

MODELING AND CONTROL OF LOCOMOTION IN COMPLEX ENVIRONMENTS

A Thesis
Presented to
The Academic Faculty

by

Tingnan Zhang

In Partial Fulfillment
of the Requirements for the Degree
Doctor of Philosophy in the
School of Physics

Georgia Institute of Technology
May 2016

Copyright © 2016 by Tingnan Zhang

MODELING AND CONTROL OF LOCOMOTION IN COMPLEX ENVIRONMENTS

Approved by:

Professor Daniel I. Goldman, Advisor
School of Physics
Georgia Institute of Technology

Professor Predrag Cvitanović
School of Physics
Georgia Institute of Technology

Professor Flavio Fenton
School of Physics
Georgia Institute of Technology

Professor James C. Gumbart
School of Physics
Georgia Institute of Technology

Professor David L. Hu
School of Mechanical Engineering
Georgia Institute of Technology

Date Approved: March 25th 2016

*To my family,
and people I love*

ACKNOWLEDGEMENTS

First of all, I would like to thank my advisor, Prof. Daniel I. Goldman. In the beginning I struggled to find my direction; he accepted me as a graduate student and led me into the interesting world of animals and locomotion. Through the years in the lab, his passion and dedication to science has deeply shaped my way of doing research. I have also learned so much from him on how to communicate and express ideas efficiently. He always cares for student's career, and he was very supportive when I decided to explore industry possibilities, which eventually helped me land my next job at Google.

I would like to express my gratitude to all colleagues of the CRAB lab: Yang Ding, Chen Li, Jeff Aguilar, Nick Gravish, Feifei Qian, Sarah S. Sharpe, Nicole Mazouchova, Perrin Schiebel, William Savoie, Mark Kingsbury, Jennifer Rieser, Henry Astley and Daria Monaenkova. Many of the fellow graduate student had already graduated and continued to do cool work in various research fields. Special thanks to Chen Li, one of my best friends who provided a lot of guidance on scientific writing. Special thanks to Perrin Schiebel and Henry Astley for inspiring discussions on snake locomotion and control. Many thanks to Jeff and Perrin for proof-reading this thesis. I also want to thank Prof. Paul Umbanhowar of Northwestern University. Although he only visited a few times, his sharp intuition and critical thinking was always enlightening.

I want to thank all my committee members, Prof. Predrag Cvitanović, Prof. Falvio Fenton, Prof. James C. Gumbart, and Prof David L. Hu, for their advice and reading my thesis. Special thanks to Prof. Predrag Cvitanović, the endowed theorist who showed me the beauty of groups and symmetries through our many discussions.

Last but not least, I would like to thank my family and my love. This work is

not possible without the unconditional love, care and support from my parents Lijun Zhang and Qi Zhang, and my love Fanjin Meng. With their help I can always conquer my frustrations and reinforce my confidence.

TABLE OF CONTENTS

ACKNOWLEDGEMENTS	iv
LIST OF TABLES	ix
LIST OF FIGURES	x
SUMMARY	xiii
I INTRODUCTION	1
1.1 Overview	1
1.2 Locomotion on and within flowable substrates	6
1.2.1 Animal locomotion on flowable ground	6
1.2.2 Granular media, model flowable substrate	8
1.2.3 Limits of terramechanics	12
1.2.4 Resistive Force Theory for granular media	13
1.2.5 Discrete Element Method	15
1.2.6 A continuum model for granular media	17
1.3 Multibody dynamics and simulations	18
1.4 Heterogeneous locomotion	22
1.4.1 Scattering motion of robots	22
1.4.2 Path planning and transport properties	26
1.5 Locomotion control and feedback	27
1.6 Organization of the thesis	30
II THE RESISTIVE FORCE THEORY FOR LEGGED LOCOMOTION ON HOMOGENEOUS GRANULAR MEDIA	31
2.1 Introduction	31
2.2 Materials and methods	32
2.2.1 Force measurements	32
2.2.2 Robot platform	35
2.3 Results and discussion	37

2.3.1	Forces on the plate	37
2.3.2	Forces on rotational intruders	38
2.3.3	Prediction of robot performance using RFT	41
2.4	Further discussions	44
2.4.1	Application to natural sand	44
2.4.2	Application to weakened granular media	45
2.5	Conclusion	46
III DISCRETE ELEMENT SIMULATION OF LEGGED LOCOMOTION ON HOMOGENEOUS GRANULAR MEDIA		48
3.1	Introduction	48
3.2	Materials and methods	49
3.2.1	Experiment platform	49
3.2.2	Simulation	52
3.3	Results and discussion	54
3.3.1	Kinematics	54
3.3.2	Ground reaction force	57
3.3.3	Parameter variation	61
3.4	conclusion	65
IV DETERMINISTIC TRANSPORT IN HETEROGENEOUS ENVIRONMENT		67
4.1	Introduction	67
4.2	Diffusion in periodic arrays	71
4.3	Elementary cell symbolic dynamics	75
4.4	Into the fundamental domain	77
4.4.1	Point group changes translation	78
4.4.2	Grammar of fundamental domain	79
4.5	Periodic orbit theory	83
4.6	Fundamental domain diffusion tensor	88
4.7	Numerical results	91

4.8	Conclusion	93
V	SNAKE LOCOMOTION AND CONTROL IN HETEROGENEOUS ENVIRONMENTS	94
5.1	Introduction	94
5.2	Materials and methods	95
5.2.1	Animal experiment	95
5.2.2	Multibody simulation	96
5.3	Results and discussions	99
5.3.1	Kinematics	99
5.3.2	Snake interaction with a single peg	101
5.3.3	Improved controller	105
5.3.4	Simulation results	105
5.4	Conclusion	110
VI	CONCLUSION AND FUTURE WORK	113
6.1	Summary	113
6.2	Future Directions	114
6.2.1	From RFT to plasticity theory	114
6.2.2	Locomotion on wet granular media	115
6.2.3	Control of limbless locomotion using multiple contacts	116
	APPENDIX A — DETAILS IN RESISTIVE FORCE THEORY	117
	REFERENCES	138

LIST OF TABLES

1	Elementary cell cycle expansion results of diffusion coefficient	91
2	Fundamental domain cycle expansion results of diffusion coefficient	91
3	Physical properties of the three granular media: poppy seeds, 0.3 mm glass spheres, and 3 mm glass spheres	120
4	Zeroth- and first-order Fourier coefficients for all media tested	125
5	Comparison of the measurements and fits of maximal vertical stress per unit depth	128
6	Particle size distribution of the natural sands tested	132

LIST OF FIGURES

1	Animals and their habitats	2
2	Hydrodynamical forces for swimming and flying in Newtonian fluids .	3
3	The Spring Loaded Inverted Pendulum template for hopping on hard ground	4
4	Flowable substrates in nature	6
5	Examples of granular media	9
6	Examples of desert animals	10
7	Drag forces in granular media depend on volume fraction	11
8	Horizontal and vertical penetration forces in granular media	12
9	Mars Rover and terramechanics	12
10	Illustration of the basic idea behind Resistive Force Theory	14
11	Multi-particle Discrete Element Method simulation	16
12	Examples of multibody simulation	19
13	Coupling between multibody simulation and DEM/RFT force models	21
14	Simulation of Xplorer walking on 3mm diameter glass particles	23
15	Single boulder scattering experiment	25
16	Snapshots of a cockroach running and following an angled wall	27
17	The multi-level control structure of locomotion systems	28
18	Delays in neural systems	29
19	Legged interaction with granular media	31
20	Measurement of resistive forces in granular media in the vertical plane using a plate element	33
21	Force and stress on a plate moving in granular media	37
22	RFT force prediction	39
23	RFT predicts legged locomotion of Xplorer	42
24	Penetration force in a weakened granular medium	45
25	RFT model for SandBot locomotion on a weakened granular surface .	46

26	DynaRoACH and experiment setup	50
27	DynaRoACH in multibody simulation	52
28	DynaRoACH two-mode locomotion	55
29	DynaRoACH performance	56
30	Peak touch-down speed of DynaRoACH leg during locomotion	58
31	Vertical ground reaction force	59
32	DynaRoACH speed upon variation of friction coefficients	61
33	DynaRoACH average forward speed versus stride frequency	63
34	A chaotic trajectory of a point particle bouncing in a hexagonal array of disks	69
35	An elementary cell and its six unit translations	71
36	Motion in fundamental domain, elementary cell, and full space	73
37	A fundamental domain periodic orbit unwrapped in full space	75
38	Elementary cell symbolic dynamics.	77
39	The three generators in fundamental domain	80
40	Fundamental domain symbolic dynamics	81
41	Diffusion coefficients computed using cycle expansion formulas	92
42	<i>C. occipitalis</i> and its movement on a white board with pegs	95
43	The snake simulation	96
44	Sequential positions of an individual <i>C. occipitalis</i> traveling in a square lattice	98
45	Snapshots of <i>C. occipitalis</i> interacting with a peg	100
46	The C-shape adopted by snakes grabbing a peg	102
47	<i>C. occipitalis</i> shape and curvature change during the interaction with a single peg	104
48	Touch sensitive controller enabled the simulated snake to grab	106
49	Effects of initial phases on contact point locomotions	106
50	Simulated snake CoM trajectories	108
51	Performance difference between controlled and passive snake in simulation	109

52	The snake robot with tactile sensing	111
53	Effective vertical and horizontal stresses per unit depth in depth-only force models	118
54	Computed net lift and thrust versus leg angle on the three model legs using depth-only force laws	119
55	The three granular media tested in our study: poppy seeds, 0.3 mm glass spheres, and 3 mm glass spheres	121
56	Vertical and horizontal stresses per unit depth	123
57	Net lift and thrust versus leg angle on the three model legs for all media tested	124
58	A generic coefficient curve that approximates scaled Fourier coefficients of all media tested	126
59	Generic stress (per unit depth) profiles for all media tested	127
60	Comparison of measured and generic stress predicted forces	128
61	A scaling routine to easily apply our resistive force model	130
62	The natural sands used to test our scaling routine	131
63	Maximal vertical stress versus depth measured in the natural sands	133
64	Net lift and thrust versus leg angle on the three model legs for the natural sands tested	134
65	Average forward speed of the robot as a function of stride frequency and leg curvature	136
66	Vertical and horizontal ground reaction forces versus time on both tripods of the robot during locomotion	137

SUMMARY

While legged and limbless animals demonstrate amazing mobility on natural, multi-component terrains, human-made devices on wheels and tracks often suffer performance loss in off-road situations. To investigate the discrepancy in locomotion efficacy, we must integrate our knowledge of biomechanics, dynamical systems, control theory, and the physics of interaction between the body/appendage and the ground. Predictive models and simulations built on such an interdisciplinary approach can help design robotic devices that gracefully navigate and manipulate complex environments.

In this dissertation, we created simulations/models to study locomotion on dry, homogeneous granular terrains. For intruders moving at low speeds (less than 0.5 m/s), granular media behave like low Reynolds number fluids. IN this regime (also known as the “frictional fluid regime”), we developed a Resistive Force Theory (RFT) to predict reaction forces on appendages moving in the vertical plane (the saggital plane). Combining these force relations with a multibody software, we could accurately and rapidly model the dynamics of a small hexapedal robot (~ 15 cm, ~ 100 g), on a granular medium composed of poppy seeds. The RFT simulation also predicted the performance of SandBot, a ~ 30 cm long, 2.5 kg weight hexapod robot, moving on A weakened granular substrate.

However, during the rapid locomotion of animals (e.g. the zebra-tailed lizard, *Callisaurus draconoides*) and robots (e.g. DynaRoACH, a cockroach inspired robot), where instantaneous limb penetration speed can reach values greater than 1.5 m/s, analogous force relations do not yet exist. Thus, we used the Discrete Element Method (DEM) to compute the limb-ground interactions. After using physical experiments to validate DEM parameters, the simulation captured the forward speed of DynaRoACH

on a substrate of 3mm glass particles at all leg stride frequencies tested. Further, the simulation revealed the mechanism by which the lightweight legged robot maintained high performance in a regime where its larger counterpart failed.

When environments become heterogeneous, new modeling and control approaches are needed. We studied the limbless locomotion of the shovel-nosed snake, *Chionactis occipitalis*, in lattices of rigid pegs affixed to a low-friction white board substrate. The kinematic analysis indicated that *C. occipitalis* actively modulated its shape and used pegs to generate thrust. Based on these findings, we constructed a close-loop-controlled snake simulation which reproduced aspects of the animal behavior. Finally, we developed a theory for transport in macroscopic, heterogeneous environments, when the long-term dynamics like diffusion constants are of interest.

CHAPTER I

INTRODUCTION

1.1 Overview

Animals must move to search for food, escape from predators, or find mates [8]. While biological locomotion has long been studied from morphological and physiological perspectives [61], it cannot be treated as an isolated phenomena involving only a few articulated joints and muscle groups. During locomotion, rhythmic motor patterns are produced by specialized circuits in the neural system, i.e. the central pattern generators (CPG) [106]. To transport the center of mass, locomotors have to interact with external environments, exchange energies, and generate thrust/drag forces using their bodies and/or appendages [75]. Information from sensory organs and mechanical feedback from the musculoskeletal system influence the central nervous system, which then adjusts the motor commands. This multi-level picture of locomotion, the integrative and comparative biomechanics and neuramechanics, is becoming increasingly popular [61, 225].

Studies in this field focus on different aspects. The contractile properties of muscles, e.g. the force-length-velocity relation, were studied *in vivo* [4] and *in vitro* [5]. Muscles and connective tendons can store/release kinematic energy and help stabilize the motion [25, 134]. The dynamics of locomotive systems can be abstracted [189, 102] and, in principle, solved using the Newton-Euler equations (or Lagrangian equations) [127] with force/torque inputs from the environment. The complex interactions between animal limbs and environments have been considered for locomotion in air [179, 222], water/fluid [215, 129, 159], and recently on natural terrains [42, 147, 142]. Efforts have also been made to connect locomotion strategies and various types

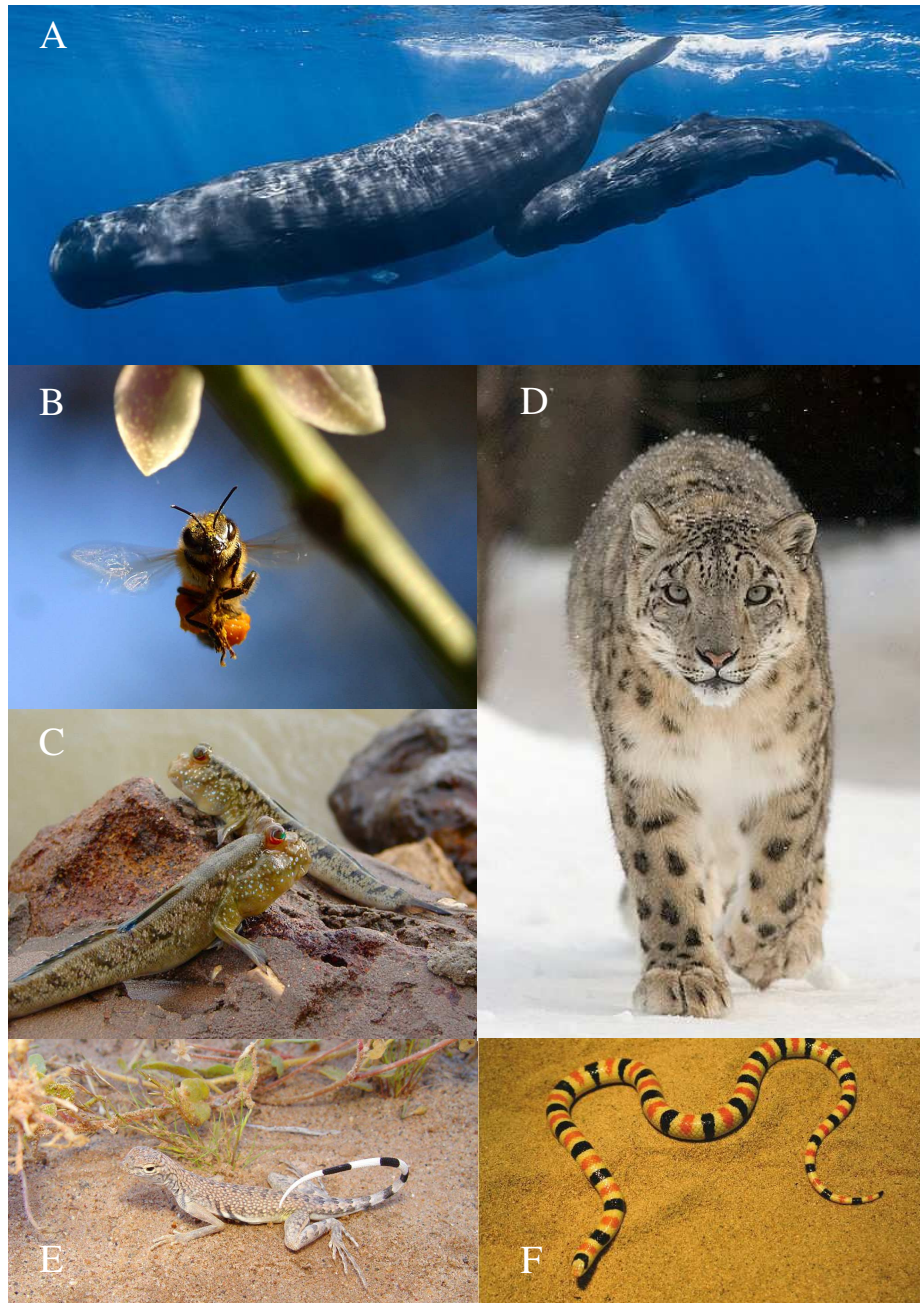


Figure 1: Animals and their habitats. (A) A group of sperm whales *Physeter macrocephalus*. (B) A buzzing bee. (C) Mudskippers. (D) A snow leopard *Uncia uncia* (E) The zebra-tailed lizard *Callisaurus draconoides*. Photo by Chen Li. (F) The Mohave shovel-nosed snake *Chionactis occipitalis*. Photo by Sarah S. Sharpe. If not otherwise indicated, all pictures are taken from Wikimedia.

of feedback information, including vision [165, 206], proprioception [186], touch [47] and temperature [200]. Finally, comprehensive theories have been proposed in attempts to incorporate all aforementioned aspects [202, 149, 172]. In this dissertation, we will primarily study the dynamics and the physics of locomotive interactions with the environment.

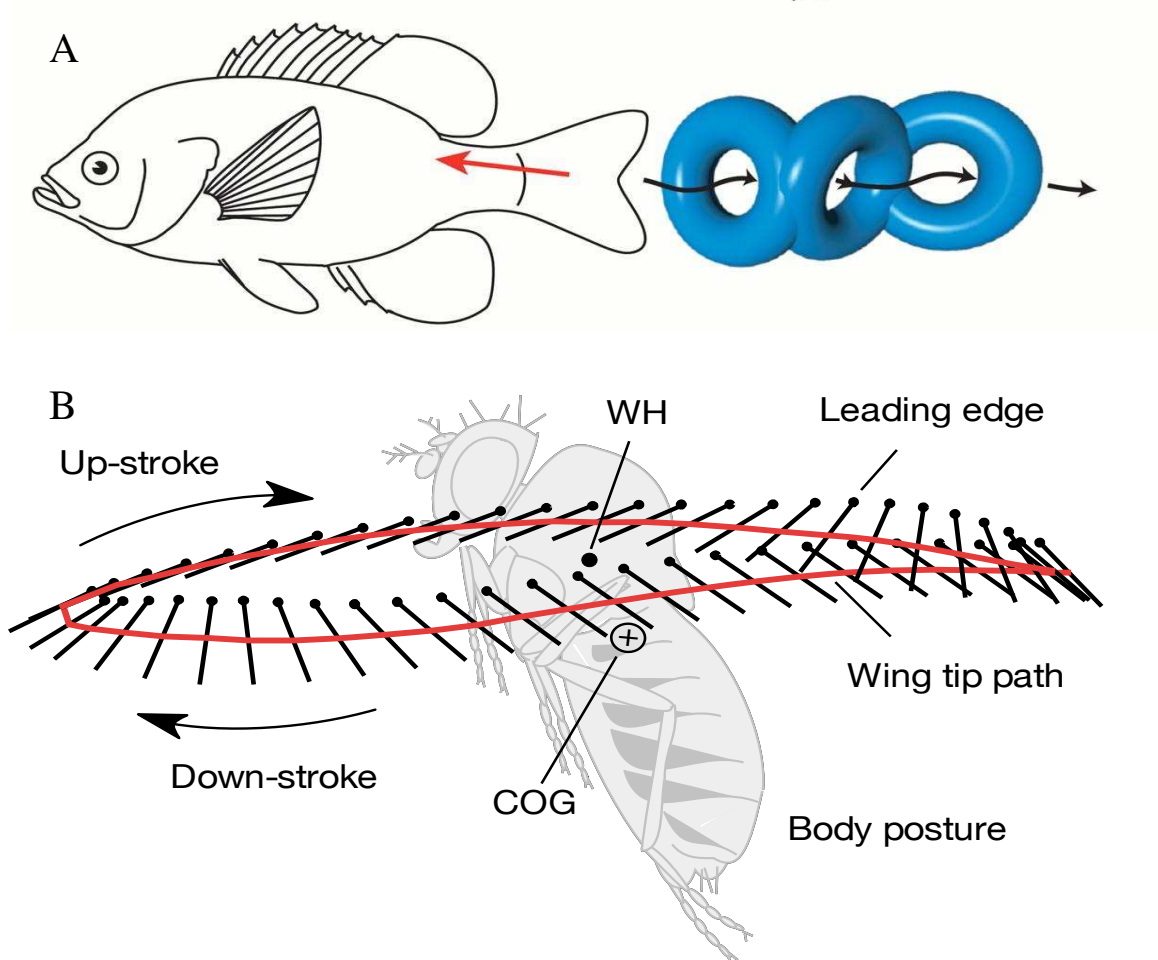


Figure 2: (A) The vortex structure (blue donut shapes) created by a moving bluegill sunfish. Adapted from [129]. (B) Wing tip trajectories of a tethered fruit fly *drosophila melanogaster*. Adapted from [132].

For flying in air and swimming in water, researchers have created many theoretical predictive models [71, 161, 219] to describe the complex interactions between the locomotor and the surrounding Newtonian fluids using the Navier-Stokes equations. With proper boundary conditions, computational fluid dynamics (CFD) can

now reproduce complex wake structures [129] around the pectoral fin of a bluegill sunfish [153], Figure 2A, or identify the velocity field near the flapping wings of a fruit fly at different stroke phases [185, 132], Figure 2B. These models have not only allowed researchers to understand the movement of aerial and aquatic organisms [219] (such as bacteria and spermatozoa [131], insects [222], birds [166], and fish and whales [129]) and their functional morphology, evolution, and ecology [67, 229], but also advanced the engineering design of aircraft [71], marine vehicles [161], and flying [229] and swimming [128] robots.

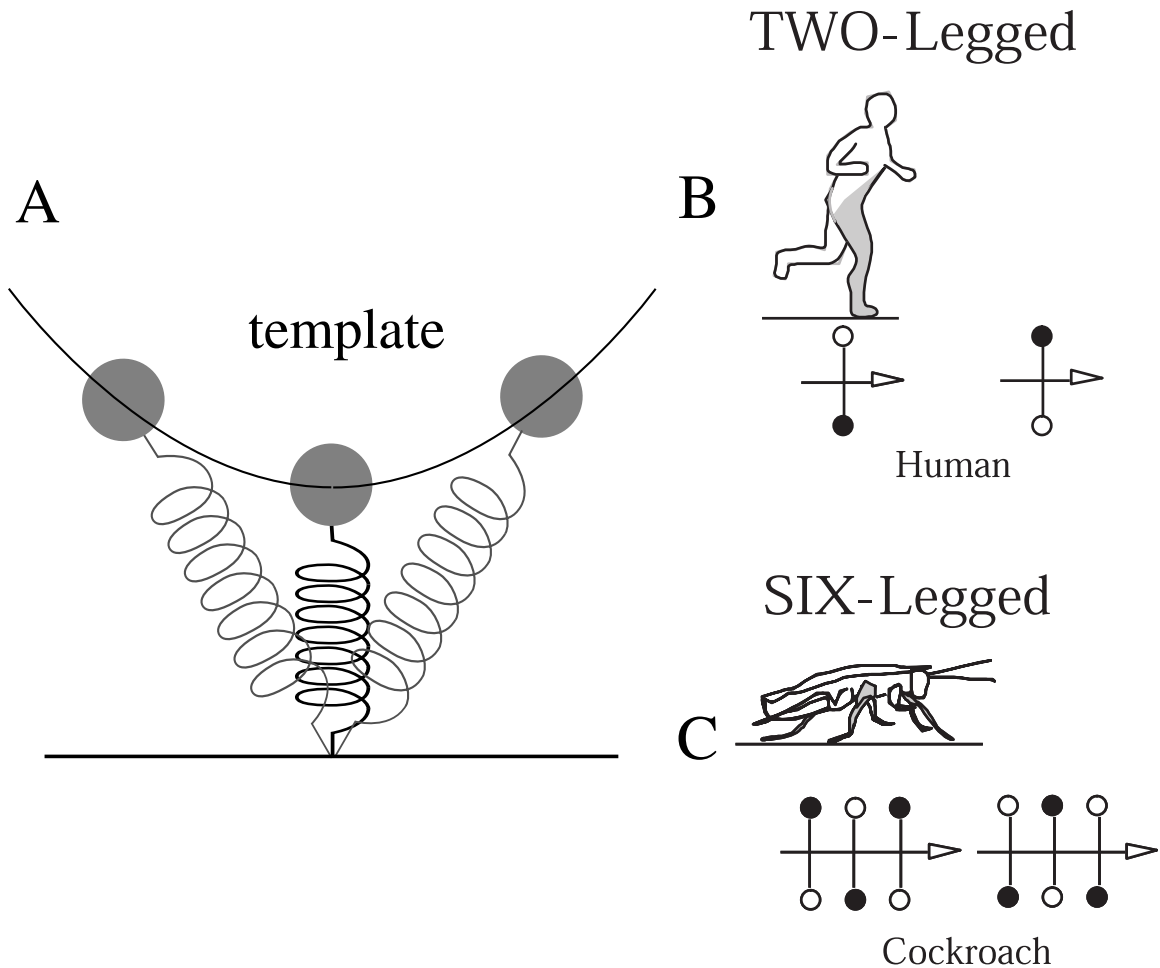


Figure 3: (A) The Spring Loaded Inverted Pendulum (SLIP) model for running on hard ground. (B) and (C) The “virtual leg” concept for movements on multiple limbs. Black or white markers indicate the group of synchronized leg(s) during the stance phase. Figure adapted from [102].

Terrestrial locomotion is another research area relevant to many different fields, from biology, physics and mechanical engineering, to robotics and industry (e.g. agricultural equipments). We can categorize ground movement into three sub-types: wheeled/tracked, legged and other limbless locomotion. The theory of wheels under rolling constraints has been established since the invention of mechanics, and the mobility of vehicles has been well studied on flat, smooth surfaces [195]. Lately, there has been an increasing need for versatile robotic devices to navigate through rough terrains of unknown physical properties. They may operate in hazardous environments for search and rescue purposes [69] and participate in exploration tasks [70]. However, compared to legged and limbless animals, the off-road mobility of wheeled and tracked vehicles is relatively limited [145].

Many terrestrial animal species (Figure 1C, D, E, and F) adopt legged locomotion, in which forward and vertical thrusts are generated by appendages moving with repetitive patterns (gaits) on ground. However, in most existing biological and robotic studies, the ground is flat and solid [202, 189, 187], and the feet are assumed to maintain non-slip contact during the entire stance phase (the gait phase that begins with foot touch down and ends with lift off) [39]. With these ansatz, template models for walking (inverted pendulum) and running (spring-loaded inverted pendulum, SLIP) were developed [39, 28]. In SLIP (Figure 3A), the body is abstracted to a point mass, and the limb is modeled as a loaded spring. The stance phase is then a simple energy saving and restoring process facilitated by the spring. This simple picture was absorbed into more comprehensive dynamical theories for animals using complicated gaits [102], Figure 3B and C. For systems with multiple appendages, the group of synchronized legs in a gait can be theoretically treated as a single, “virtual leg” [178]. Advanced robots such as BigDog [177] and RHex [187] have been built on this philosophy and can hop and dynamically balance on uneven, rough terrains such as pebbles.

Limbless locomotion on/in complex substrates is also prevalent in nature, often used by snakes [88, 111], worms [176] and some lizard species [78, 142]. It is highly flexible due to the many degrees of freedom that the slender body bears (for example, a snake can have $\sim 100 - 300$ vertebrates linked in a long chain). But the curse of dimensionality also limits the understanding of such locomotion and makes effective control a difficult task. Nevertheless, templates for snake-like locomotion have been proposed [99, 144, 18] and tested on robotic platforms [99, 144].

1.2 Locomotion on and within flowable substrates

1.2.1 Animal locomotion on flowable ground



Figure 4: Examples of flowable terrestrial substrates. (A) Sand dunes. (B) Leaf litter. (C) Snow. (D) Martian soil. Term of use: (A) Photo by Rosino. (B) Photo by bosela, used under the license Morguefile.com/cropped from original. (C) Attributed to Jason Hollinger. (D) Image is credited to NASA/JPL/Cornell.

Many terrestrial environments are composed of rheologically complex soft materials that flow upon interaction (Figure 4); examples include sand, mud, snow, and leaf debris. During the stance phase, the limb-ground contact point does not remain fixed [134], thus breaking assumptions of the SLIP template discussed previously. Even worse, flowable terrestrial materials are not yet modeled at the level of Newtonian fluids. Understanding locomotion in such environments is, therefore, an open problem.

Legged and limbless animals [30, 73, 218, 175, 134] face the challenges of moving on flowable substrates. The group led by Hanley studied the energy expenditures for mule deer and elk locomotion on snow, and they noticed a curvilinear increase in the cost of transport (CoT, the energy consumed to move unit distance) when snow depth and density increased [73]. However, some animals demonstrate agility and maneuverability on flowable terrains. Li et al. found that, by slapping its hind feet down at high speed (≈ 1 m/s) with toes spread parallel with the ground, the zebra-tailed lizard was able to running quickly over granular media [134]. Later, Qian et al. systematically studied various species (*Uma scoparia*, *Sceloporus olivaceus*, *Ocypode quadrata*, *Callisaurus draconoides* and *Pachydactylus bibroni*) moving on weakened granular media prepared with an air-fluidized bed [175]. They found that while most test animals (*U. scoparia*, *S. olivaceus*, *O. quadrata* and *P. bibroni*) suffered from performance loss (as measured by forward moving speed) when air flow increased and the ground stiffness decreased, the zebra-tailed lizard (*C. draconoides*) was able to maintain its normal locomotion speed, even when the medium was completely fluidized. Moreover, all animals out-performed the test robots (SandBot [135] and Xplorer [136]) for the same ground conditions. Despite the complexity in control, limbless locomotion works surprisingly well on flowable ground. For example, Marvi et al. recently showed that sidewinders (*Crotalus cerastes*) manipulated the length of the body in contact with granular surface in order to effectively climb granular

inclines [144].

There have also been scattered efforts to monitor and model the movement of small organisms in the soil, sand, and mud. Charles Darwin’s final book focused on the actions of worms on soil [58]. In the 1960s using capacitive sensing, Norris and Kavanau studied subsurface locomotion of four species of limbless reptiles (three snakes and one lizard) [122]. Trueman investigated the burrowing of mole crabs [210] and the razor clam *Ensis* [209] in soft substrates. Recently, Winter et al. studied the burrowing mechanism of razor clams in mud and found that the animal fluidizes the substrate to reduce drag [224]. Groups led by Jung [118] and Arratia [117] studied the swimming of nematodes in wet granular media and enhanced mobility was found when compared with fluids.

1.2.2 Granular media, model flowable substrate

Although we classify sand, soil, mud, snow, and debris all to flowable grounds, their resistance properties are not equally understood. For example, our understanding of mud is surprisingly limited; there is no established model to quantitatively characterize this structured fluid. While snow crystals have been carefully studied [171], little is known about the structure of loose, porous snow medium. A few experiments of snow avalanching [123] were conducted, but the general force-relations (e.g. penetration resistance) are still not disclosed at this stage.

On the contrary, the rheology of granular media has been studied extensively [160, 109, 97, 10]. A granular material is a collection of macroscopic, solid particles [10]. The inter-particle contact forces are typically repulsive and dissipative, because thermal fluctuations and electrostatic interactions are negligible. Like other flowable terrains, granular media exhibits solid-fluid duality [109]. When frictional contacts between grains break under stress, the medium yields (due to localized forcing from



Figure 5: Examples of granular media in nature (top row) and in lab (bottom row). Sand pictures from Wikimedia.

intruders) or avalanches in a tilted container [160]. The state of a static, homogeneous granular medium (in which particles are composed of the same material and have similar sizes) can be described by a single dimensionless parameter, the volume fraction (or packing fraction) ϕ , which is the ratio of the solid volume (the sum of grain volumes) to the media volume. For dry granular media, ϕ typically varies in $0.57 < \phi < 0.64$ [62], although the exact range is influenced by particle friction [113]. Using the air-fluidized bed and shaking protocols [190], we can precisely control ϕ in laboratory settings.

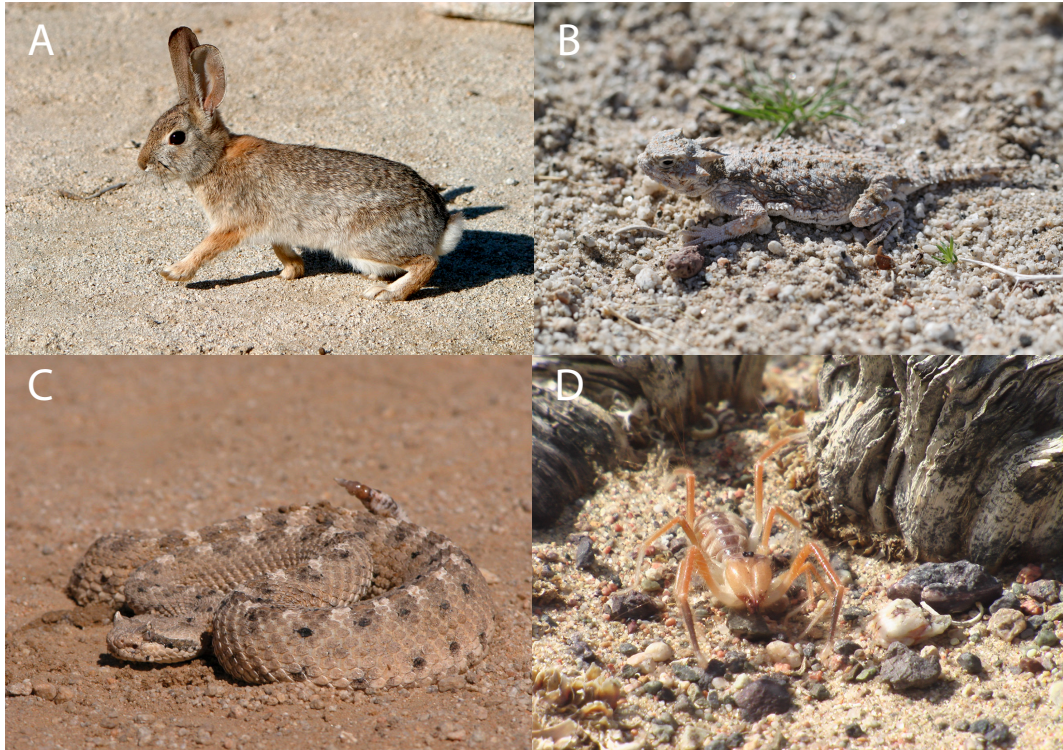


Figure 6: Examples of desert animals. (A) Desert cottontail, *Sylvilagus audubonii*. (B) Desert horned lizard, *Phrynosoma platyrhinos*. (C) Rattlesnake, *Crotalus cerastes*. (D) Camel spider, *Solifugae*. Pictures from Wikimedia.

Granular media, i.e. deserts, cover a significant portion of the land on earth [167, 72]. Although water is scarce, there is diverse wildlife present in desert [38, 151]. Typical sand dwelling animals include mammals such as rabbits (desert cottontails),

ground squirrels and kangaroo rats; some lizard and snake species, including the zebra-tailed lizards, desert horned lizards and rattlesnakes; and many arthropods such as scorpions and solifuges (camel spiders). While many animals demonstrate high mobility [134, 144] on this flowable terrain, their thrust generation mechanisms are unclear and not well studied.

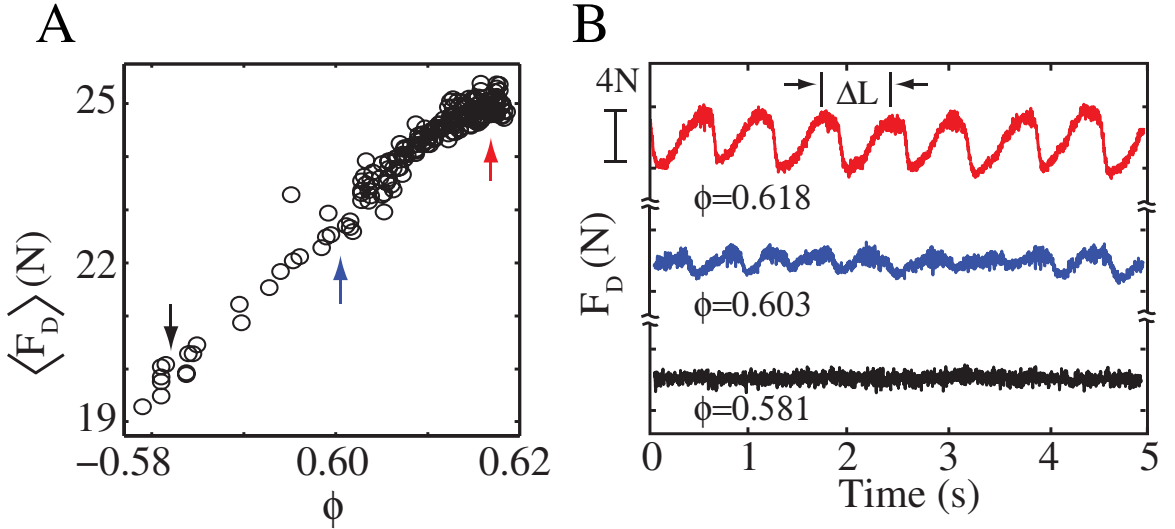


Figure 7: Drag forces in granular media depend on volume fraction. (A) Average drag force vs ϕ . Temporal force profiles are plotted in (B) for selected volume fractions (indicated by colored arrows). (B) Temporal fluctuation of drag forces at three packing fractions. Figures reproduced from [87].

In granular physics, efforts have been made to understand drag (vertical and horizontal) [7, 6, 82, 87] and lift [63, 93] forces on intruders moving at low speed ($v \lesssim 0.5$ m/s, roughly speaking). Gravish et al. performed experiments with a flat plate plowing through homogeneous granular media prepared at different ϕ , and they found that both the average drag force and temporal fluctuations in the drag increase with the packing fraction (Figure 7 A and B) [87]. For a fixed ϕ , drag forces increase approximately proportional to the leading area of intruder and penetration depth [98, 93, 32] (Figure 8A, B), but are insensitive to the changes in moving speed of intruders (Figure 8A). These studies are the building block, from which we developed more complex and comprehensive force models that demonstrated predictive power in

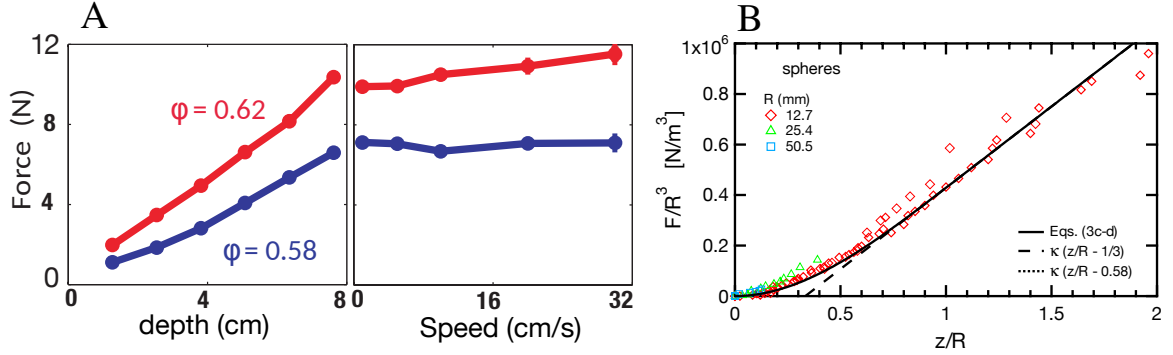


Figure 8: (A) Horizontal drag forces on a cylinder at different depths and speeds. Plot adapted from [142]. (B) Scaling of vertical drag forces for a spherical intruder. z is the penetration depth and R is the radius of the sphere. Figure reproduced from [32].

modeling animal locomotion on and within homogeneous granular media [136, 142]. Below, we explain these advanced force theories, and discuss their applicabilities and limitations.

1.2.3 Limits of terramechanics

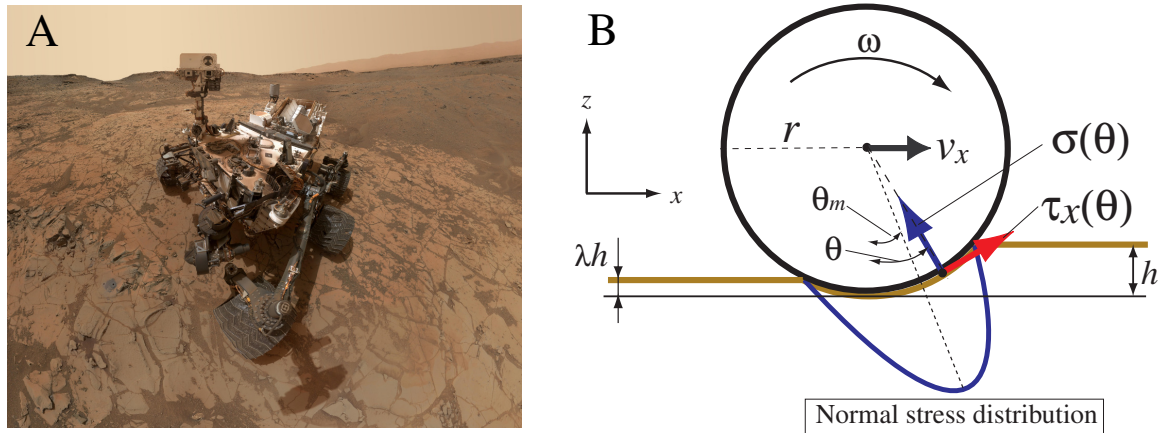


Figure 9: (A) Mars Rover Curiosity's selfie. Photo from NASA. (B) The terramechanics theory for wheel-ground interaction. A wheel of radius r is moving with forward speed v_x and angular speed ω . The normal σ and tangent τ_x stresses on the contact surface depend on the angular position θ . The ground deforms during interaction and the level of surface behind the wheel is generally lower (as indicated by the scaling parameter λ). Figure adapted from [107].

We briefly review terramechanics, the force model developed for wheeled locomotion on loose soil and granular media. Off-road mobility has long been a concern for engineers building wheeled/tracked devices, with a considerable amount of effort applied to model the interactions vehicles and loose, flowable terrain such as sand. The terramechanics approach, dating back to the 1960s, models soil as (roughly speaking) a nonlinear damped spring [23]. At each contact point on the wheel or tread, normal and shear stresses are computed, often using many fitting parameters (depending on the stress model [110, 227, 226]), Figure 9 (B). The stress projected to the vertical direction is then balanced with the load of the system to determine the static and dynamic sinkage of the wheel during slip (a condition when the lowest point of the wheel has a non-zero speed relative to the ground) [107]. Terramechanics has advanced the off-road mobility of vehicles in the past 50 years on highly deformable soil. However, since the method was primarily developed for large, heavy vehicles (such as tanks), its applicability towards small, light-weight robots is less understood [192]. Also, the interaction of geometries other than wheels and tracks (e.g., legs) with soil is not well modeled.

1.2.4 Resistive Force Theory for granular media

At this stage, there is no fundamental force law for granular media at the level of Navier-Stokes equations for fluids. In most previous studies, intruders of simple (e.g. cylindrical and rectangular) shapes were used, and movement patterns were simple, involving only translation in either the horizontal or vertical plane. The scaling force laws developed cannot be applied directly to locomotion in which parts of the body (often of irregular shapes) translate and rotate simultaneously¹.

In our lab, we were inspired by the approach developed by pioneers in fluid mechanics who did not solve (and, without computational fluid dynamics, could not)

¹Part of this section was edited based on a published work [230] with permissions.

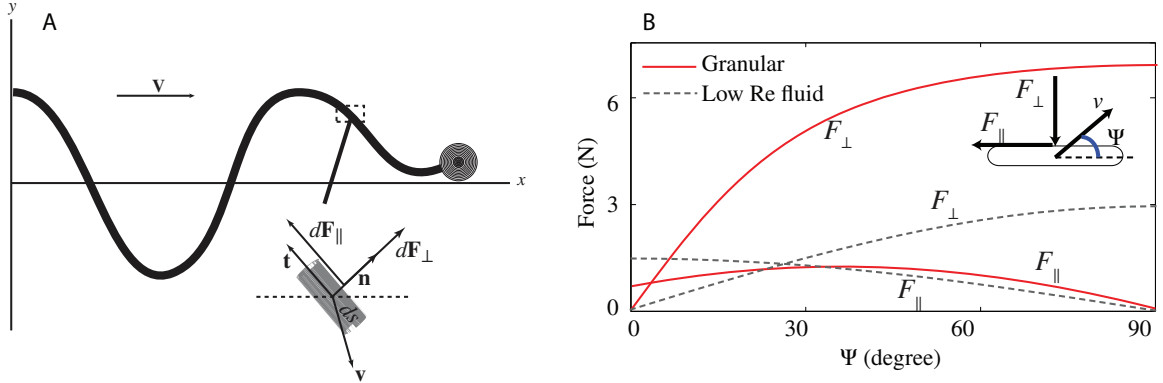


Figure 10: (A) Illustration of the basic idea behind Resistive Force Theory (RFT) for 2D swimming. The body propagates a wave of prescribed shape in the negative x -direction and experiences reaction forces which propel it forward. Each infinitesimal element ds on the swimmers body is characterized by its tangent direction $\hat{\mathbf{t}}$ (or normal direction $\hat{\mathbf{n}}$) and its velocity \mathbf{v} direction; each element experiences a force $d\mathbf{F}_{\perp,\parallel}$. In true fluids, these forces were described by Stokes law, while for granular media, they are measured in experiment. Figure adapted from [230]. (B) Averaged $\mathbf{F}_{\perp,\parallel}$ on the cylinder wall vs. angle of attack Ψ . \mathbf{F}_{\perp} is enhanced in GM compared with a low Re fluid. Figure reproduced from [64].

the full Navier-Stokes equations for complex flows in the presence of non-trivial moving boundaries. Instead, simpler approximations were made in viscous fluids. The best known of these, called Resistive Force Theory (RFT) [89] assumes that the deforming body can be partitioned into segments, each experiencing drag, and that the flow/force fields from these segments are hydrodynamically decoupled and do not influence the fields of other segments. Therefore, the normal and tangential forces on a small element (Figure 10A) depend only on the local properties, namely, the length of the element ds , the velocity \mathbf{v} and the orientation $\hat{\mathbf{t}}$ (the fluid is homogeneous, so position dependence is dropped). The net force on the swimmer is then computed from the integral

$$\mathbf{F} = \int (d\mathbf{F}_{\perp} + d\mathbf{F}_{\parallel}) = \int ds (f_{\perp}(\mathbf{v}, \hat{\mathbf{t}})\hat{\mathbf{n}} + f_{\parallel}(\mathbf{v}, \hat{\mathbf{t}})\hat{\mathbf{t}}), \quad (1)$$

where the functional forms of f_{\perp} and f_{\parallel} can in principle be determined from Stokes equations; however, experiments are often needed because analytical solutions to

Stokes equations cannot be easily obtained even in simple cases (e.g., a finite length cylinder moving in the axial direction [212]). In granular media where there is no constitutive law, f_{\perp} and f_{\parallel} can only be determined from experiment or DEM [143] simulation (details discussed later).

In viscous fluids, the RFT approximation has had some success when compared to experiment [130, 22, 137]. However, in the physiologically relevant regimes for which RFT was originally formulated (the movement of flagella for bacteria, for example), discrepancies between RFT and experiment have recently been observed [181]. To remedy this, more comprehensive theories have been developed, and these account for higher order corrections (see [181] for discussion).

RFT with empirically determined f_{\perp} and f_{\parallel} can accurately model (and predict aspects of) locomotion of animals and physical models of animals (robots) within dense GM [142, 64, 94, 63, 65]. This has been somewhat surprising, since we initially worried that interaction with a medium that can display features of a solid [160] a compressible fluid [10] and/or a gas [31] would require models which accounted for the physics of each regime as well as transitions between them. In this dissertation, we have extended RFT to legged locomotion where interactions happen in a approximately vertical plane.

1.2.5 Discrete Element Method

High-speed granular impact has been studied in various lab controlled settings [120, 85, 44], and scaling relations were discovered. These simple force laws can, at the best, be used to qualitatively explain complex locomotion systems. We still lack a quantitative model that can predict the intrusion forces in the high-speed regime relevant to the rapid locomotion of animals [134] and robots [231]. Luckily, there exists a robust numerical tool, the Discrete Element Method (DEM, Figure 11A, B, and C) [51], which is able to reproduce many granular phenomena with high fidelity.

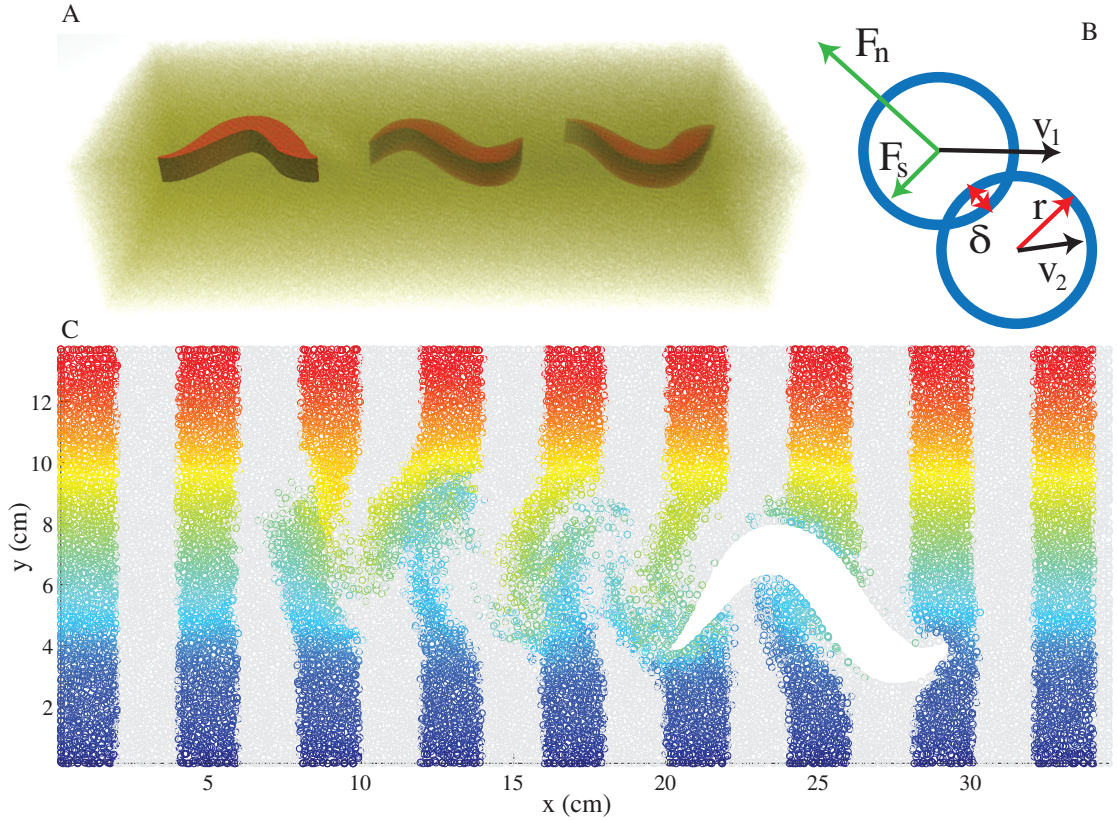


Figure 11: Multi-particle Discrete Element Method simulation (DEM) reveals how material flows around a swimming simulation. (A) A 3-dimensional DEM simulation of the sandfish lizard *Scincus scincus* in a medium of approximately 3×10^5 approximately 3 mm diameter glass spheres. The snapshots of the animals body are rendered in red. (B) In DEM simulation, when particles (of radius r) with velocities \mathbf{v}_1 and \mathbf{v}_2 collide with each other, the inter-particle contact forces $\mathbf{F}_{n,s}$ are computed from a virtual overlap δ which represents the elastic deformation at the contact area. (C) Top view of the subsurface swimming of a simulated sandfish (*S. scincus*) in DEM. Particles above the plane of interest have been rendered transparent. The movement of the animals body (indicated by the white region) mobilizes the particles around it. Colored stripes are used for visualization. Colors in the stripe correspond to the initial y positions (decrease from red to blue) of particles before the medium is disturbed. Image created by Yang Ding.

The philosophy behind DEM is straightforward, that is, to simulate the movement of every particle in the media and compute the interaction forces between each pair of grains in contact [44]. The particle deformation, i.e. the strain, during collision is represented by a virtual overlap (Figure 11B). The normal contact force is then computed using damped-spring-dashpot model [60], which has its foundation in the Hertzian theory [116] for elastic solids. The tangential force may be modeled using the dashpot formulation with different parameter values, or simply as Coulomb friction. DEM simulations were used to study the rheology of granular media; common topics include the shear band formation [108, 207, 164] and discharge rate in hoppers [9, 45], etc. Previous studies [63, 143] have also shown that, once the parameters in the contact models were correctly tuned, DEM accurately computed the drag and impact forces exerted by an intruder moving in particulate media. In this dissertation, we use the nonlinear spring force model proposed in [63, 143]. The normal and tangent forces are written as:

$$\begin{aligned}
 F_n &= k_n \delta^{3/2} - g_n \nu_n \delta^{1/2} \\
 F_t &= \mu F_n,
 \end{aligned}
 \tag{2}$$

where v_n is the normal component of the relative velocity, k_n the Hertzian contact stiffness, and g_n the viscoelasticity dissipation coefficient. The correct combination of k_n and the phenomenological parameter g_n will produce the velocity dependent coefficient of restitution measured in experiments [143]. For tangential forces we use the normal Coulomb friction. Values of these coefficients can be found in [143, 231] for 3 mm diameter glass particles and 6 mm diameter ABS plastic particles.

1.2.6 A continuum model for granular media

Recently, progress has been made in understanding the foundation of RFT and, more broadly, the connection between intrusion forces and material flow in granular media. The group led by Kamrin has developed a plasticity theory [119] for dense granular

flow. Combined with the material point method (MPM) simulation [68], they can reproduce known experiment measurements, such as the width of a shear-band developed in the split-bottom geometry [96]. The theory was recently extended to include moving boundaries, and flows and forces developed in the yielding regime were predicted [17]. The RFT force relations [136] in the vertical plane were quantitatively replicated. The surface pressure distributions predicted from the theory matched the numerical computation of RFT, for intruders of different geometries moving steadily. Although the reason behind the linear superposition in RFT has not yet been clarified, the plasticity theory already encoded information such as particle sizes and intruder speed (inertia effects) [17]. Further experiments are needed to testing this promising model in regimes where the RFT assumptions are not validated (e.g. high-speed intrusion).

1.3 Multibody dynamics and simulations

To model complex locomotion systems, we used high-fidelity multibody solvers. Multibody simulation, i.e. the method that numerically computes the dynamical systems composed of articulated rigid bodies, has broad applications. It has been used in the film industry to create realistic animations without motion capture, in the automobile industry to model engine combustion gears and suspension systems (Figure 12A), in aerospace engineering [21, 157], and recently in robotics research (Figure 12B and C) and advanced robots such as BigDog [170].

The core task of every multibody engine is to solve the Newton-Euler equations:

$$\begin{pmatrix} M & 0 \\ 0 & I \end{pmatrix} \begin{pmatrix} \dot{\mathbf{v}} \\ \dot{\boldsymbol{\omega}} \end{pmatrix} + \begin{pmatrix} 0 \\ \boldsymbol{\omega} \times I \boldsymbol{\omega} \end{pmatrix} = \begin{pmatrix} \mathbf{f} \\ \boldsymbol{\tau} \end{pmatrix}, \quad (3)$$

where M and I are the mass and moment of inertia matrices, \mathbf{f} and $\boldsymbol{\tau}$ account for external forces and torques, \mathbf{v} and $\boldsymbol{\omega}$ are translational and rotational velocities. Rigid

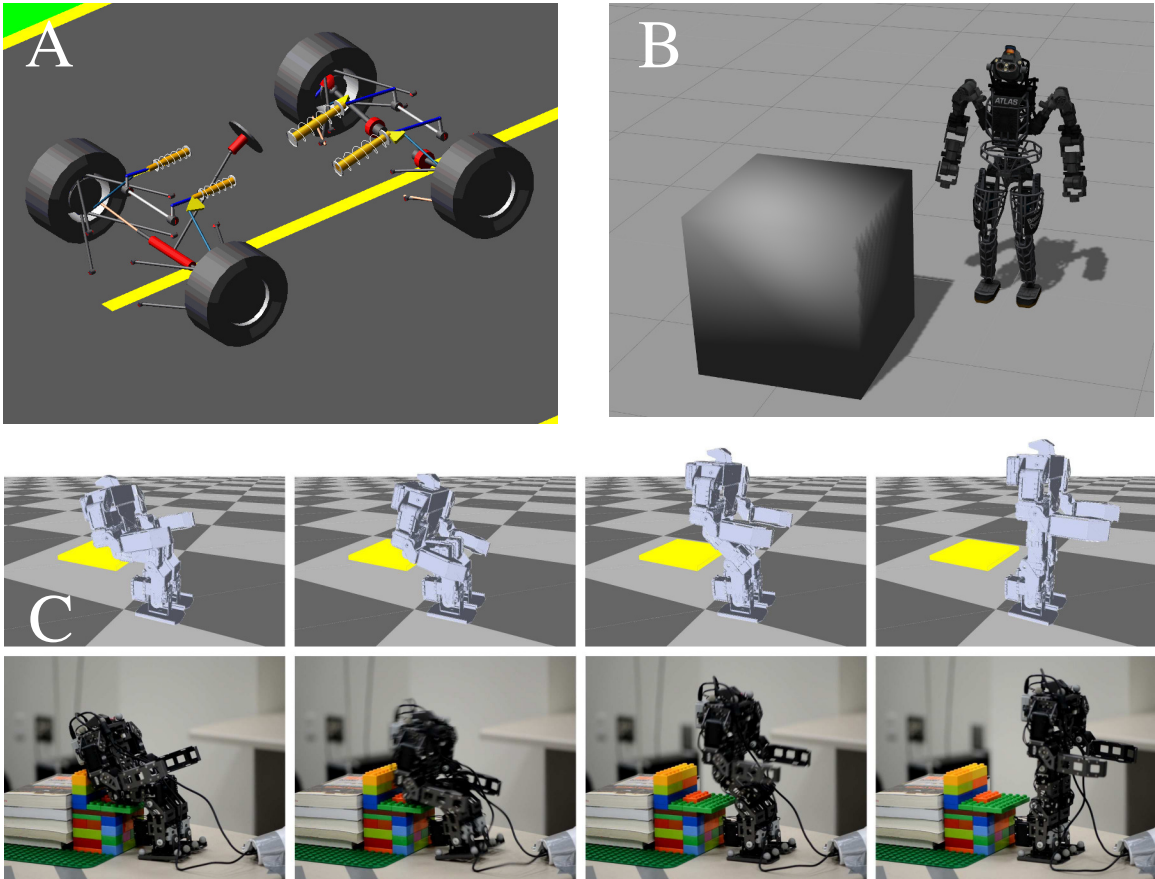


Figure 12: (A) MSC Adams simulation of a car suspension system. Adapted from mcssoftware.com under fair use. (B) Atlas, the bipedal humanoid robot simulated in Gazebo. Figure from gazebo.org. (C) Multibody simulation aided sit-to-stand task of a bipedal robot. Figure adapted from [203].

bodies in simulation are typically connected with joints of various kinds, each imposing some type of kinematic constraints. The constraints can either be solved using Lagrange multipliers, or eliminated if we reformulate the problem using generalized coordinates [138]:

$$M(\mathbf{q})\ddot{\mathbf{q}} + C(\mathbf{q}, \dot{\mathbf{q}}) = \mathbf{Q}_{int} + J_v^T \mathbf{f} + J_\omega^T \boldsymbol{\tau}, \quad (4)$$

where \mathbf{q} and $\dot{\mathbf{q}}$ are general coordinates and velocities. Centrifugal and Coriolis forces are absorbed into $C(\mathbf{q}, \dot{\mathbf{q}})$. \mathbf{f} and $\boldsymbol{\tau}$ are projected into the \mathbf{q} -coordinate system using Jacobians J_v for linear velocities, and J_ω for angular velocities. \mathbf{Q}_{int} represents the internal drive forces (in a vector form), such as torques generated by the motors.

Contact modeling is an challenging topic in the multibody simulation. The physics of interactions between solids [116, 169] is complicated and beyond the scope of this dissertation. In multibody simulation, the details of elastic deformations are ignored and the contact forces are computed using abstracted methods. In early models, contacts were resolved by adding penalty forces/impulses to penetration (e.g. such as in DEM simulation) [205]. The time step needed for numerical convergence is typically small for materials with high Young’s modulus. The current state-of-the-art approach explores LCP (linear complementarity problem) based formulations [168] where contacts are described by unilateral constraints, and the friction cones are discretized [121, 201]. Special stepping algorithms [12, 201] were developed to solve the non-smooth, stiff contact dynamics. For example, Tasaro et al. have proposed an iterative method to compute the continuous cone constraints [12, 13], and implemented it in their Chrono::Engine [204, 146], a C++ based physics simulation library. In this dissertation, we used MBDyn², an experimentally validated [83] physics engine to model dynamics of legged robots. Lately, to study the limbless locomtion

²Source code available at www.mbdyn.org

we switched to the high-fidelity Chrono::Engine³, which has a more flexible API (application program interface) and better visualization. The soft ground interactions in our simulation are based on either RFT or DEM, while rigid body collisions are handled directly in the physics engine (e.g. Chrono::Engine).

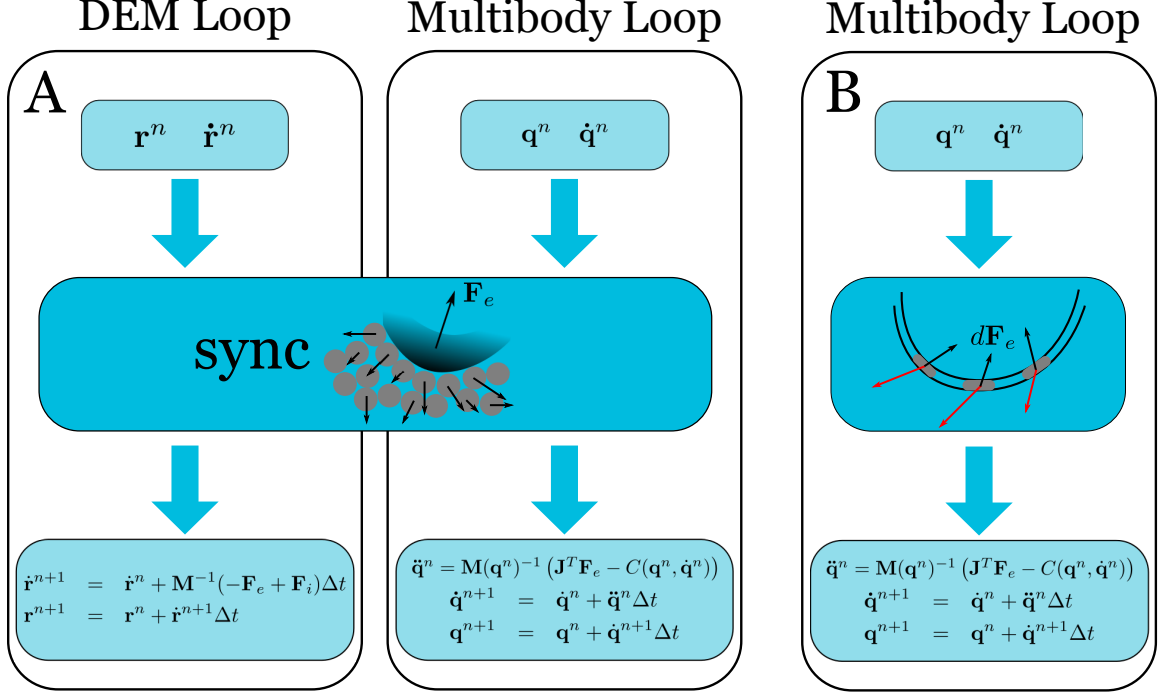


Figure 13: Coupling between multibody simulation and (A) DEM or (B) RFT force models. $(\mathbf{q}^n, \dot{\mathbf{q}}^n)$ is the state of the articulated rigid-body system at the n -th step during simulation. $(\mathbf{r}^n, \dot{\mathbf{r}}^n)$ represents the state of the particle system in DEM. $\mathbf{F}_e/d\mathbf{F}_e$ is the $3M \times 1$ column vector containing DEM/RFT interaction forces applied to all M rigid bodies. \mathbf{F}_i is the inter-particle collision force vector of dimension $3N \times 1$, where N is the number of simulated grains. Black arrows indicate forces on individual particles and rigid bodies. Red arrows indicate velocities at different surface elements of a rigid body. Δt is the time step.

We illustrate the idea of multibody-ground cosimulation in Figure 13. At the beginning of each simulation step, we consider the force vector \mathbf{F}_e applied to the right-hand side of Equation 4. If RFT is used as the input force model, we simply sum the element force $d\mathbf{F}_e$, which depends on the local velocity and orientation

³Source code and instructions can be found at <http://chronoengine.info/chronoengine/>

or each small surface segment (Figure 13B, middle block). Then, the multibody dynamics is updated by the physics engine and ready for next iteration. In this way, the simulation only contains the multibody loop. If use DEM, we have to compute \mathbf{F}_e and inter-particle collision force \mathbf{F}_i from contacts between rigid bodies and particles. We also update both the multibody system and the particle system, and synchronize their states before the next force computation stage (Figure 13A, middle block). The time step Δt needed for simulation to converge depends on the force models being used. In DEM systems, small values ($1 \sim 2 \mu s$) for time step are needed to capture the particle collision process. In RFT simulation, we usually set $\Delta t = 0.01s$ for real time computation; reducing Δt does not give observably different dynamics.

1.4 Heterogeneous locomotion

1.4.1 Scattering motion of robots

When robots step into Mother Nature, they face the challenging environments that wild animals are familiar with—uneven, rough and multicomponent heterogeneous terrains. Unlike homogeneous granular media which is better understood, most natural terrains have some randomness, and their resistance properties are not predictable. Pioneers in the robotics community have built legged systems that can negotiate multiple terrains. Examples of such robots includes RHex [187] and BigDog [177], and the recently released next-generation Atlas (a bipedal, humanoid robot). However, most existing studies have focused on the control [223] and mechanical design [187] aspects of these robots. Principles of locomotion and transport in heterogeneous environments have not yet been revealed.

In recent years, we have begun to approach heterogeneous locomotion problems from a “robophysics” perspective [3]. Robots can serve as simplified locomotor models because they are highly controllable (as compared with animals that often exhibit unpredictable behavior) and their parameters are tunable. Systematic studies using

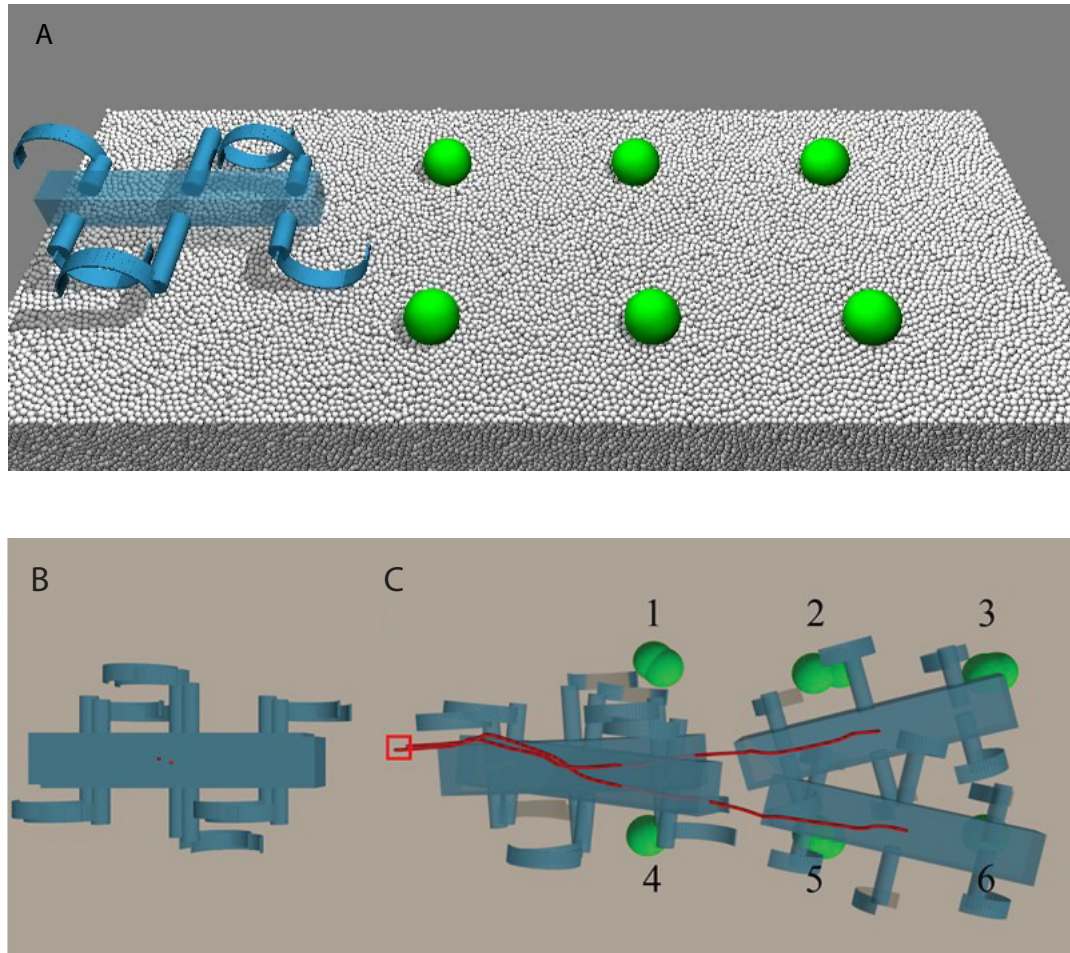


Figure 14: (A) Simulated Xplorer robot walking on 3mm diameter particles. Glass boulders (green spheres, 1.5 cm in radius) were added to perturb the locomotion. (B) Two simulation runs started with very similar initial positions. (C) After a few steps, the center of mass (CoM) trajectories (red lines) began to separate. Figure adapted from [174].

robots have facilitated the understanding of locomotion principles on/in homogeneous flowable terrain, for various movement modes such as walking and running [135, 136, 231], jumping [1], and limbless undulation [142, 144].

In the spirit of robophysics, we studied the heterogeneous locomotion problem in a lab controlled environment [174]. While a natural particulate terrain contains poly-dispersed particles (the diameters of which range from a few hundred microns to several centimeters), the “model” heterogeneous medium was bi-dispersed, and composed of a homogeneous bed of 3 mm glass particles, and boulders of 3 cm in diameter. We used an open-loop controlled hexapod robot, Xplorer [136] as the test platform. The motion of the robot was captured by high-speed cameras (AOS X-PRI) at 250 frames per second. A DEM simulation was created to compare with experiment (Figure 14A). In both experiment and simulation, the locomotion of Xplorer was perturbed, as shown from the tracked center of mass (CoM) trajectories (Figure 14C). Although the condition of the test bed was precisely controlled at the particle level (the positions and velocities of individual particles) in simulation, if the robot’s starting positions were varied by ~ 0.5 cm (which is $\sim 5\%$ of the body length, Figure 14B), the CoM trajectories separated after a few leg strides [174]. The sensitivity on initial condition is a signature of chaotic behavior, frequently observed in turbulence [184], ODE (ordinary differential equation) systems [41, 139, 199], and some families of low dimensional maps [92].

In later studies, we made extensive experimental efforts to understand the complex interactions between Xplorer’s leg and a boulder placed on a granular medium composed of loosely packed poppy seeds (Figure 15) [173, 174]. The change of the robot’s moving direction (the scattering angle θ , Figure 15B) after collision with the single boulder depended sensitively on both the impact parameter (the distance between the boulder and the centerline of the robot before collision, Figure 15B and C) and the fore-aft position (the initial distance between the CoM of Xplorer and the

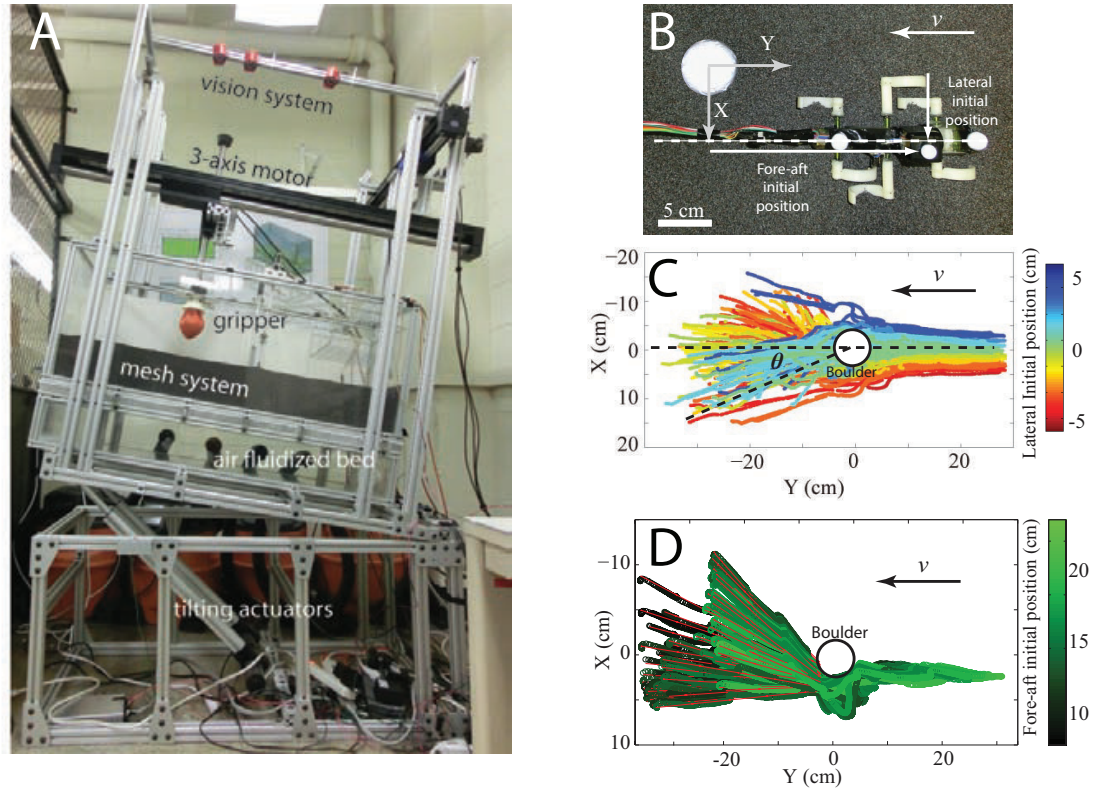


Figure 15: Single boulder scattering experiment. (A) Automated terrain creation and locomotion testing system. The automated system, including the vision system, the 3-axis motor, the universal jamming gripper, the air fluidized bed and the tilting actuators. (B) Experimental setup. The center of the boulder is set as the origin. X and Y axis represents lateral and fore-aft direction. (C) Robot CoM trajectories for different lateral initial positions (i.e., different impact parameter). Data were collected from a free boulder experiment, where the boulder was initially placed at a burial depth of ≈ 1 cm, a quarter of the free boulder diameter. Trajectory color indicates different impact parameters. (D) Robot CoM trajectories for various fore-aft initial positions (i.e., different leg phase at contact). Data were collected from immobile boulder experiment, where the boulder was fixed at a burial depth of ≈ 1.25 cm, a quarter of the stationary boulder diameter. Red lines represent the linear fit of the robots trajectories after boulder interaction, which was used to calculate the scattering angle θ . The white circles in (B) and (C) indicate boulder position. Figure adapted from [174].

boulder, projected to the moving direction, see Figure 15B and D). Detailed observations indicated that θ was largely determined by the inclination angle at the point of first leg contact, and was insensitive to the actual material composition and geometry of the boulder.

Although complicated, the interaction between the robot and the boulder can be described by a non-trivial potential function that depends on state variables (e.g., leg phase and CoM position) [174]. Based on this evidence, an anticipatory controller was examined [173] to “counter” the effects of boulders.

1.4.2 Path planning and transport properties

In a field of obstacles where the robot is scattered by a potential at each step, it is not surprising that the dynamic of the open-loop controlled robot is chaotic. Given the instability presented in heterogeneous locomotion and the complexity of the underlying interaction model, an accurate analytical/numerical description of the dynamical system seems hopeless.

However, not all locomotion tasks require precise predictions of trajectories. For example, animal foraging behavior requires locomotion control at a strategic level (e.g. searching and path planning) [216, 217]. In a context where the present food distribution is far away (so a direct sensing is not valid) and undetermined, what are optimal searching paths that increase survivability? Various studies have raised this question [196, 105], where animal locomotion patterns were analyzed at a landscape level. A similar situation applies to robotic devices in search and rescue tasks, where points of interest (such as locations of victims of an earthquake) remain to be explored efficiently. In recent years, there have been scattered studies on chaotic planning and trajectory generation in autonomous robots [158, 220]. At the time of this dissertation, literature on this topic is still scarce, and few principles have been revealed. While studies have shown some scaling laws for animal behaviors [196], they

only hypothesized, vague connections between movement patterns and properties of the environment (such as drift and diffusion in fluids) [105].

In this dissertation, we explore the in-depth topic of diffusional transport in a deterministic setting, where interaction forces between scatterers and a passively controlled, constant-speed particle are modeled using hard-wall potentials. “Artificial potential” based control has been proposed and tested in the past [180, 126]. We anticipate that the theory presented can be used as fundamental blocks in advanced path planning algorithms for next-generation field robots.

1.5 Locomotion control and feedback

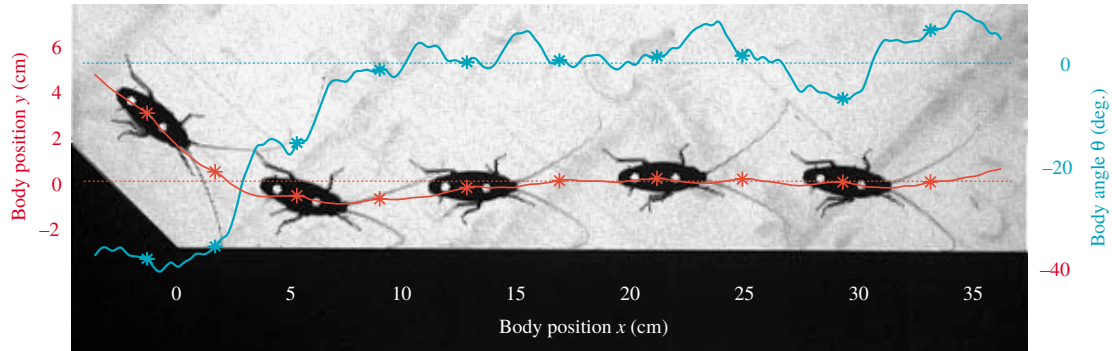


Figure 16: Snapshots of a cockroach running and following an angled wall. The cockroach’s body trajectory is plotted in red. The blue curve indicates the body angle. Figure adapted from [47].

Animal locomotion in many scenarios is guided by a closed-loop control system. The controller, i.e. the neural system, is responsible for processing information of the environment collected from various sensory sources (such as vision, tactile sensing from the antenna, force and torque measurements from ensembles of Golgi tendon organs [48]). Signals combining motor pattern and sensory feedback are emitted to groups of synergistic muscles, which generate motion that is adaptive to the environment. There are many examples of animal locomotion with integrated feedback. was shown to use its antenna during high speed running to follow walls that change

orientation (Figure 16) [47]. The bipedal guinea fowl can dynamically balance its steps on obstacles by increasing distal muscles recruitment [57].

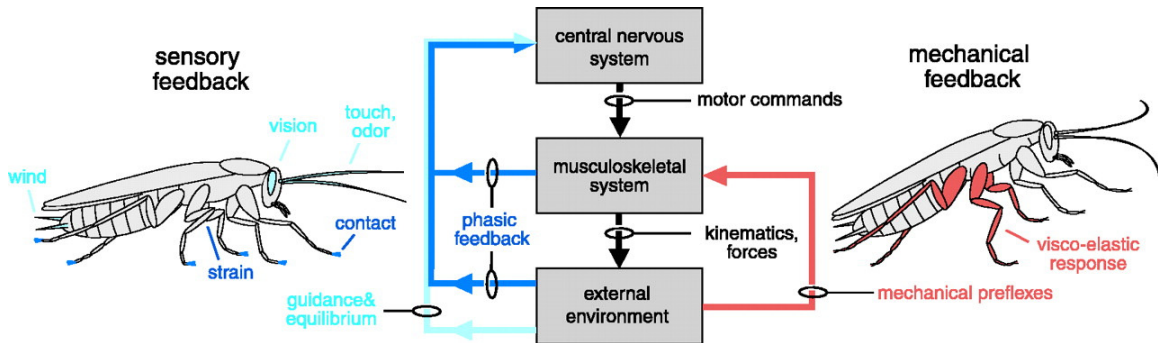


Figure 17: The multi-level control structure of locomotion systems. Figure adapted from [61].

There are two distinct categories of feedback: the sensing feedback that needs to be actively processed (Figure 17, left side), and mechanical feedback which responds passively at the musculoskeletal level (Figure 17, right side). Although in this introduction we will not delve deeply into the neuromechanics world, it is worthwhile to differentiate the roles of different sensory feedback. Inputs from central sensors such as eyes and ears are used to adjust the overall moving direction and speed, while proprioceptors such as the inner ear maintain the body balance unconsciously. Phasic feedbacks (mainly from mechanosensory cells such as muscle spindles) are fired at the time of rapid perturbation. They can modulate the motor pattern within a step cycle and increase the robustness of locomotion.

In neural systems, time delays are inevitable (Figure 18) [47, 95]. For example, there is often a lag between the onset of stimuli and the time stamp at which sensors begin to collect and transmit information [95]. Such delays challenge the number of viable control schemes that rely on the sensing information [95]. In fact, it has been shown that the mechanical response (the spring and damper-like, intrinsic behavior of musculoskeletal structures) can play a dominant role in the stability of repetitive, rapid locomotion [74]. The groups led by Full and Holmes proposed the lateral

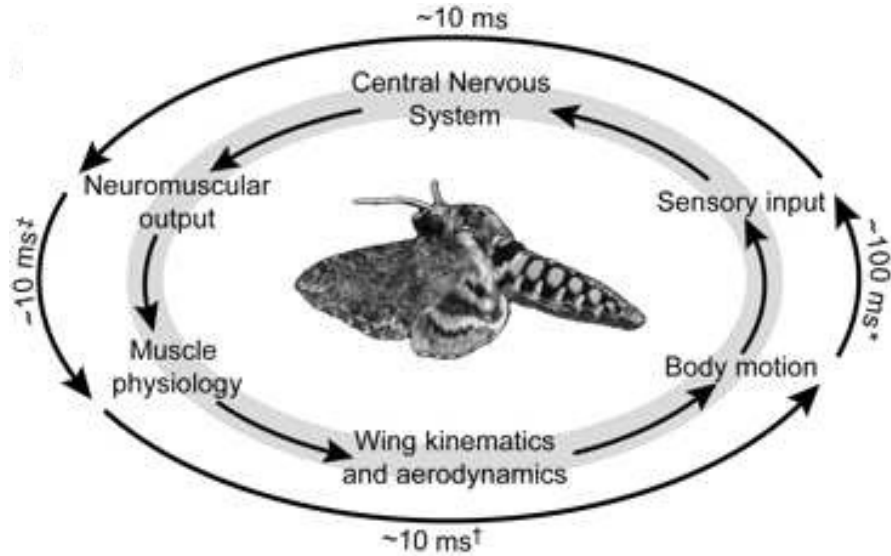


Figure 18: Illustrated diagram showing the information flow and time delay during the hawkmoth flying. Figure adapted from [162].

leg-spring (LLS) model [188], a self-stabilizing system that explained the horizontal recovery of cockroaches under sudden perturbations [114]. Conversely, a naive control strategy based on feedback from body orientation may slow down the equilibrium process of the natural dynamics (as described by the LLS template) [188].

In robot control, sensing feedback often needs to be tightly coupled to low-level, mechanical compliance in motors and actuators. A robot arm with high proportional gain (i.e. low compliance) can trace the desired trajectory accurately in a workspace with known boundaries. However, when a snake robot undulates in an array of pegs positioned randomly, such precise control using fixed joint space template (e.g. the serpentine wave [99]) can be a disaster [208]. Hogan et al. have proposed an impedance control [100] in which loads from the environments (forces at the end-effector and torques at joints) may be used to tune both the compliance and the inertia response of the manipulator actively [101]. The desired behavior of the system, i.e. the target impedance, was often encoded in second-order,

damped-oscillator equations [101]. Controllers built with this scheme were demonstrated in legged [33, 211] systems traversing rough environments and limbless [182] robots climbing pipes, although physical principles connecting compliance, environment properties, and locomotion efficiency have not yet been discovered. In this dissertation, we apply biologically inspired, compliant control schemes to a snake-like robot in simulation, and systematically study the locomotion performance.

1.6 Organization of the thesis

With the framework introduced, this thesis is organized in the following manner:

1. In Chapter 2, a RFT model for low-speed, legged locomotion on granular surface is presented. The chapter is edited based on [136].
2. In Chapter 3, I illustrate a DEM study of lightweight, high-speed locomotion on granular fluid. The chapter is edited based on [231, 175].
3. In Chapter 4, transport and diffusion of a particle moving in a heterogeneous environment, the Lorentz gas is discussed.
4. We present preliminary studies of snake locomotion and control in Chapter 5.

CHAPTER II

THE RESISTIVE FORCE THEORY FOR LEGGED LOCOMOTION ON HOMOGENEOUS GRANULAR MEDIA

The contents of this chapter was edited based on the published papers [136, 175]. RFT force measurements and Xplorer experiments were conducted by Chen Li. Penetration tests in weakened granular and SandBot experiments were conducted by Feifei Qian.

2.1 Introduction

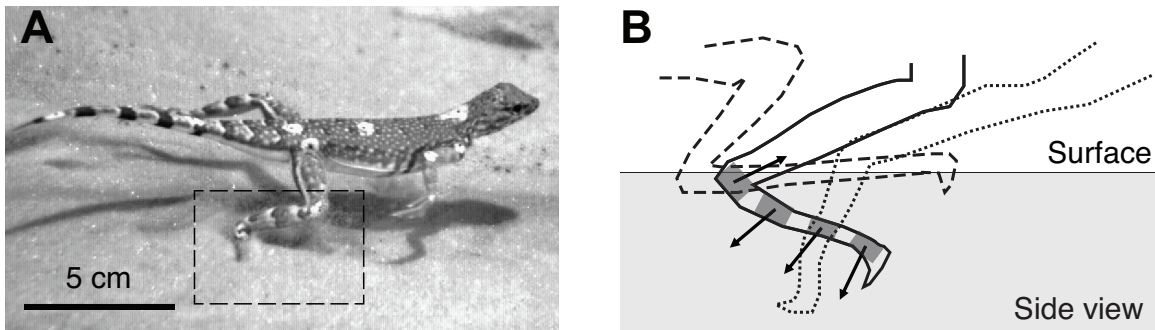


Figure 19: Legged interaction with granular media. (A) A zebra-tailed lizard running on sand [134]. Dashed box indicates the region of leg-ground interaction shown in (B). Schematic of leg-ground interaction for (B) the hind foot of the zebra-tailed lizard. Dashed, solid, and dotted tracings are leg positions at early, mid, and late stance. Bars and arrows indicate local orientations and movement directions of leg elements. The gray area is the granular substrate.

To begin to create a terradynamics that allows the prediction of legged locomotion on a flowable ground, we hypothesized that the net forces on a leg (or a body) moving in a granular medium in the vertical plane could be approximated by the linear superposition of resistive forces on infinitesimal leg (or body) elements. Our hypothesis was inspired by our recent success in applying the methods of resistive

force theory [131] to predict the forces and movement during the limbless locomotion of a lizard swimming in sand [142] and in describing the drag [142, 63] and lift [63] on simple objects moving in granular media at fixed depths. In these studies, the linear superposition was valid for intruders moving in granular media in the horizontal plane at low enough speeds (for example, ≤ 0.5 m/s for 0.3-mm glass particles [142]), where intrusion forces are dominated by particle friction (insensitive to speed) and non-inertial [142]. However, it was unclear whether linear superposition could apply to legs (or bodies) of complex morphology and kinematics moving in the vertical plane. In this chapter we will answer these questions in detail.

2.2 Materials and methods

2.2.1 Force measurements

To measure resistive forces for leg elements, we moved a thin rigid plate (of area A) in granular media in the vertical plane at 1 cm/s and measured lift f_z and drag f_x on the plate (in the continuously yielding regime). We determined vertical and horizontal stresses $\sigma_{z,x} = f_{z,x}/A$ as a function of the plates depth $|z|$ below the surface, angle of attack β , and angle of intrusion γ (Figure 20). To test the generality of our resistive force model, we used three dry granular media of various particle size, shape, density, and friction, prepared into flat, naturally occurring, loosely and closely packed states [135, 142] (Figure 55, and Table S1). Slightly polydispersed near-spherical glass particles 0.3 and 3 mm in diameter (covering the particle size range of natural dry sand (~ 0.1 to ~ 1 mm) [19]) and rounded, slightly kidney-shaped poppy seeds (0.7 mm in diameter) allowed us to probe general principles for naturally occurring granular media of high sphericity and roundness (such as Ottawa sand [43]). We discuss at the end of the paper possible effects of particle nonsphericity and angularity also found in many natural sands [43].

We used aluminum to construct the plate element (area $A = 3.81 \times 2.54$ cm²,

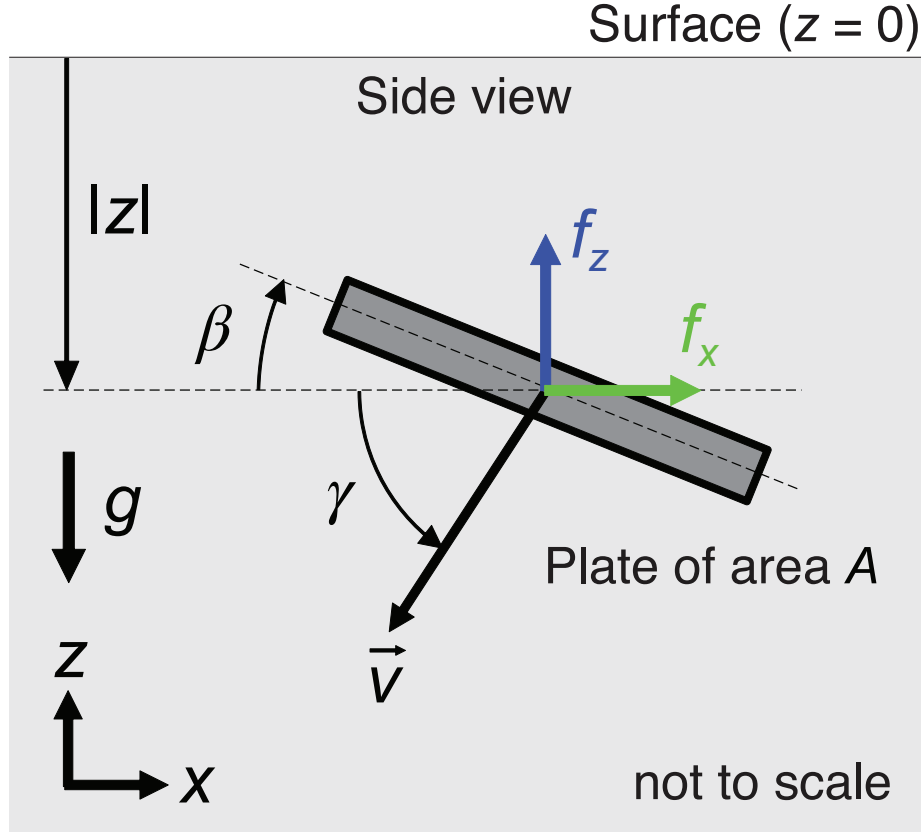


Figure 20: Lift F_z (blue arrow) and drag F_x (green arrow) on a thin rigid plate of area A moving in granular media (gray area) in the vertical plane at speed $v = 1$ cm/s were measured as a function of the plates depth $|z|$ below the surface, angle of attack β , and angle of intrusion γ . The granular media were fluidized (and then compacted when a closely packed state was prepared) using an air-fluidized bed. g is gravitational acceleration.

thickness = 0.64 cm) and model legs (maximal length $2R = 7.62$ cm, width = 2.54 cm, thickness = 0.64 cm). We measured the friction coefficient μ between aluminum and poppy seeds to be 0.40 (later we constructed robot legs using plastic of a similar friction coefficient with poppy seeds, 0.36), by placing an aluminum plate on a wooden plate bonded with a single layer of poppy seeds, increasing the slope of the wooden plate from zero, and examining the angle ξ at which the aluminum plate began to slide. Thus $\mu = \tan\xi$. The length and width of both the plate element and model legs were ~ 10 times the particle diameter, ensuring that the granular media could be approximated as a continuum.

Before each force measurement, we used an air fluidized bed ($24 \times 22 \text{ cm}^2$ surface area) to prepare the granular media (15 cm deep) to a well-defined compaction (see Table 3 for the volume fractions of closely and loosely packed states of the granular media tested). Air flow was turned off during force measurements. We used a 6 degree-of-freedom robotic arm (CRS Robotics) to move the plate element and rotate the model legs. We used a 6-axis force and torque transducer (ATI Industrial Automation) mounted between the intruder and the robotic arm to measure forces to a precision of 0.05 N at a sampling frequency of 100 Hz. We performed all the force measurements at low speeds ($\sim 1 \text{ cm/s}$) to ensure that particle inertia was negligible, and in a vertical plane at the middle of the air fluidized bed and far from the sidewalls (distance $> 3 \text{ cm}$) to minimize boundary effects.

In the plate element intrusion experiment, we attached the plate to the force and torque transducer via a supporting rod and an adjustable mount with which attack angle β could be varied. We varied intrusion angle γ by adjusting the trajectory of the robotic arm. For each combination of β and γ , we separately measured the forces on the supporting rod and mount moving in the granular media without the plate, and subtracted them to obtain forces exerted by the granular media on the plate alone.

During each test session, we first prepared the granular media while the plate was above the surface. We then moved the plate (oriented at attack angle β) downward to the surface (depth $|z| = 0$), paused it for 2 seconds, and then intruded it into the granular media along intrusion angle γ . After intrusion was finished, we prepared the granular media again, and extracted the plate along the same path. This gave us measurements of stresses $\sigma_{z,x}$ for both $\pm(\beta, \gamma)$. For horizontal movements ($\gamma = 0$), $\sigma_{z,x}$ were nearly constant when the plate was far from the container sidewalls, and we obtained $\alpha_{z,x}$ by fitting Eq. 1 to averages of $\sigma_{z,x}$ in the steady state regions at three depths ($|z| = 2.54 \text{ cm}$, 5.08 cm , and 7.62 cm). We measured $\alpha_{z,x}$ for γ within

$[-\pi/2, \pi/2]$, and determined $\alpha_{z,x}$ for γ within $[-\pi, -\pi/2]$ and $[\pi/2, \pi]$ by symmetry:

$$\begin{cases} \alpha_z(\beta, \gamma) = \alpha_z(-\beta, -\pi - \gamma) & \text{if } -\pi \leq \gamma \leq -\pi/2 \\ \alpha_z(\beta, \gamma) = \alpha_z(-\beta, \pi - \gamma) & \text{if } \pi/2 \leq \gamma \leq \pi \end{cases} \quad (5)$$

$$\begin{cases} \alpha_x(\beta, \gamma) = -\alpha_x(-\beta, -\pi - \gamma) & \text{if } -\pi \leq \gamma \leq -\pi/2 \\ \alpha_x(\beta, \gamma) = -\alpha_x(-\beta, \pi - \gamma) & \text{if } \pi/2 \leq \gamma \leq \pi \end{cases} \quad (6)$$

In the model leg rotation experiment, we rotated the model legs at an angular velocity $\omega = 0.2$ rad/s at a hip height $h = 2$ cm within leg angle $-3\pi/4 \leq \theta \leq 3\pi/4$ (at the beginning and end of which all three legs tested were fully above the granular surface), where leg angle θ was defined as the angle sweeping from the vertical downward direction to the direction along which leg length was maximal. For each model leg, we separately measured the forces due to the weight of the model legs rotating in the air, and subtracted them to obtain the forces on the model legs exerted by the granular media during rotation.

Due to the high repeatability of our fluidized bed and robotic arm, we found that for all media tested, run-to-run variation in $\alpha_{z,x}$ for fixed β and γ was always within 0.005 N/cm³ at any given depth; thus we only performed one trial for each combination of β and γ . All the stresses were calculated in the regions where the plate was far from the container boundaries (distance > 6 cm). We also confirmed that for low enough speeds, intrusion forces in granular media were insensitive to speed (for example, in loosely packed poppy seeds, at $v = 1$ m/s, force only increased by less than 20% from that at $v = 1$ cm/s); thus, particle inertia was negligible.

2.2.2 Robot platform

We built our robot (body length = 13 cm, body mass = 150 g) by modifying a small commercially available robot (RoboXplorer, Smart Lab). The robot had similar morphology and kinematics as a RHex robot, with a rigid body and six legs performing

1 degree-of-freedom rotation in an alternating tripod gait. We substituted the stock motor with a stronger one (RadioShack Super Speed 9–18 VDC Hobby Motor, Model # 273-256) and modified the gear trains (gear ratio: 47 revolutions in the motor transmits into 1 rotation of the legs). These changes increased maximal stride frequency f to 5 Hz. We removed the external body shell to reduce weight and the belly area (to $13 \times 2 \text{ cm}^2$). This reduced drag on the belly during locomotion on granular media.

We used 3-D printing to make custom robot legs. All the legs had the same maximal length $2R = 4.1 \text{ cm}$, width = 1.0 cm, and thickness = 0.3 cm, but different curvatures $1/r = [-1, -0.92, -0.60, 0, 0.60, 0.92, 1]/R$. The ABS plastic used to fabricate the legs had a similar friction coefficient with poppy seeds (0.36) to that of aluminum with poppy seeds (0.40). The leg width and length were ~ 10 times the particle diameter, allowing the granular media to be approximated as a continuum. We ensured that the legs had large enough stiffness and moved like rigid bodies ($< 5\%$ deformation) during locomotion.

We tuned the center of mass of the robot to overlap with the geometric center of the body by adding mass to the lighter end of the robot. We measured the masses, dimensions, and relative positions of all robot body and leg parts, and calculated the moment of inertia of the robot to be $I = 2.08 \times 10^3 \text{ g cm}^2$ about the pitch axis through the center of mass. We powered the robot by an external power supply (Power Ten Inc.) to ensure constant voltage during trials, and adjusted voltage to vary stride frequency f between trials.

Before each trial, we used an air fluidized bed track ($200 \times 50 \text{ cm}^2$ surface area) to prepare the granular media (12 cm deep) to a well-defined compaction. We used two synchronized high-speed cameras (X-PRI, AOS Technologies) to capture top and side views of the robot’s locomotion at 500 frame/s. We measured f from the side view, and measured forward speed v_x from the top view by digitizing a high contrast

marker placed near the center of mass. For each f and $1/r$, we performed three trials and reported mean \pm s.d. for average forward speed \bar{v}_x in experiment.

2.3 Results and discussion

2.3.1 Forces on the plate

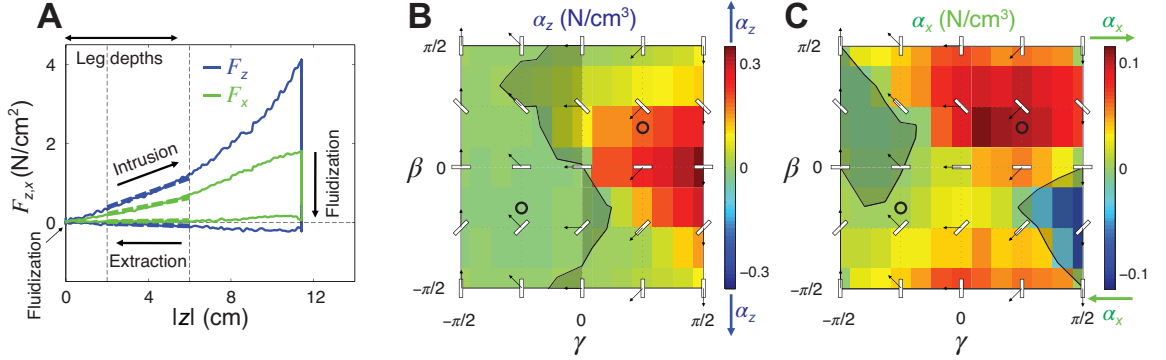


Figure 21: (A) Vertical (blue curve) and horizontal (green curve) stresses $\alpha_{z,x} = F_{z,x}/A$ versus $|z|$ for representative intrusion and extraction using $(\beta, \gamma) = \pm(\pi/6, \pi/4)$ into loosely packed poppy seeds. Blue and green dashed lines are linear fits with zero intercept over intermediate depths at which the plate was fully submerged and far from the bottom of the container. Horizontal arrows on top indicate the range of leg depths in Figures 22 and 23. (B) Vertical and (C) horizontal stresses per unit depth $\alpha_{z,x}$ [slopes of dashed fit lines in (A)] versus β and γ . Plate schematics with arrows denote representative orientations and movement directions. Black curves indicate where $\alpha_{z,x} = 0$. The shaded areas indicate where α_z (or α_x) is not opposing the plates vertical (or horizontal) velocity. Circles indicate z,x from data shown in (A). Arrows above and below the color bars indicate directions of $\alpha_{z,x}$ for positive and negative values.

In all media tested, we observed that for all attack angles β and intrusion angles γ , $\sigma_{z,x}$ were nearly proportional to depth $|z|$ when the plate was fully submerged and far from the bottom of the container (Figure 21A). This is because friction-dominated forces are proportional to the hydrostatic-like pressure in granular media. Therefore, we modeled the hydrostatic-like stresses as

where $\alpha_{z,x}$ are vertical and horizontal stresses per unit depth (slopes of dashed fit lines in Figure 21A). We found that in all media tested, $\alpha_{z,x}$ depended sensitively on

both attack angle β and intrusion angle γ (Figure 21, C and D, Figure 56, and additional data Table S5). $\alpha_{z,x}$ was opposing the plates vertical (or horizontal) velocity for most but, counter-intuitively, not all β and γ (exceptions are indicated by the shaded regions). For almost all attack angles β , $\alpha_{z,x}$ had larger magnitudes for intrusion angle $\gamma \geq 0$ than for $\gamma \leq 0$; i.e., it was harder to push the plate into granular media than to extract it. For all intrusion angles γ except $\gamma = \pm\pi/2$, $|\alpha_{z,x}|$ were asymmetric to attack angles $\beta = 0$ and $\beta = \pm\pi/2$; i.e., only when the plate moved vertically were stress magnitudes the same for vertically or horizontally mirrored orientations (e.g., $\beta = \pm\pi/6$). These asymmetries are a result of gravity breaking symmetry in the vertical plane and differ from the case in the horizontal plane [142]. Our resistive force measurements are an advance from previous force models based on the flat-plate approximation used in many terramechanic models [23, 150], which capture only the dependence of stresses on intruder depth, but not on its orientation or movement direction (Figure 53).

Despite their different magnitudes and subtle differences in shape, the overall profiles of stresses (per unit depth) $\alpha_{z,x}(\beta, \gamma)$ were similar for all media tested. Furthermore, these stress profiles could be approximated (to the first order) by a simple scaling of generic stress profiles (Figures 58 and 59, and Tables 4 and 5).

2.3.2 Forces on rotational intruders

We next tested our hypothesis that forces on a complex intruder moving in granular media in the vertical plane could be approximated by the linear superposition of forces on all intruder elements. We measured the net lift F_z and thrust F_x on thin rigid model legs rotating about a fixed axle (simulating a tethered body [222, 229]) through granular media in the vertical plane at ~ 1 cm/s (Figure 22). We then compared them to predictions from the resistive force model by the integration of stresses over

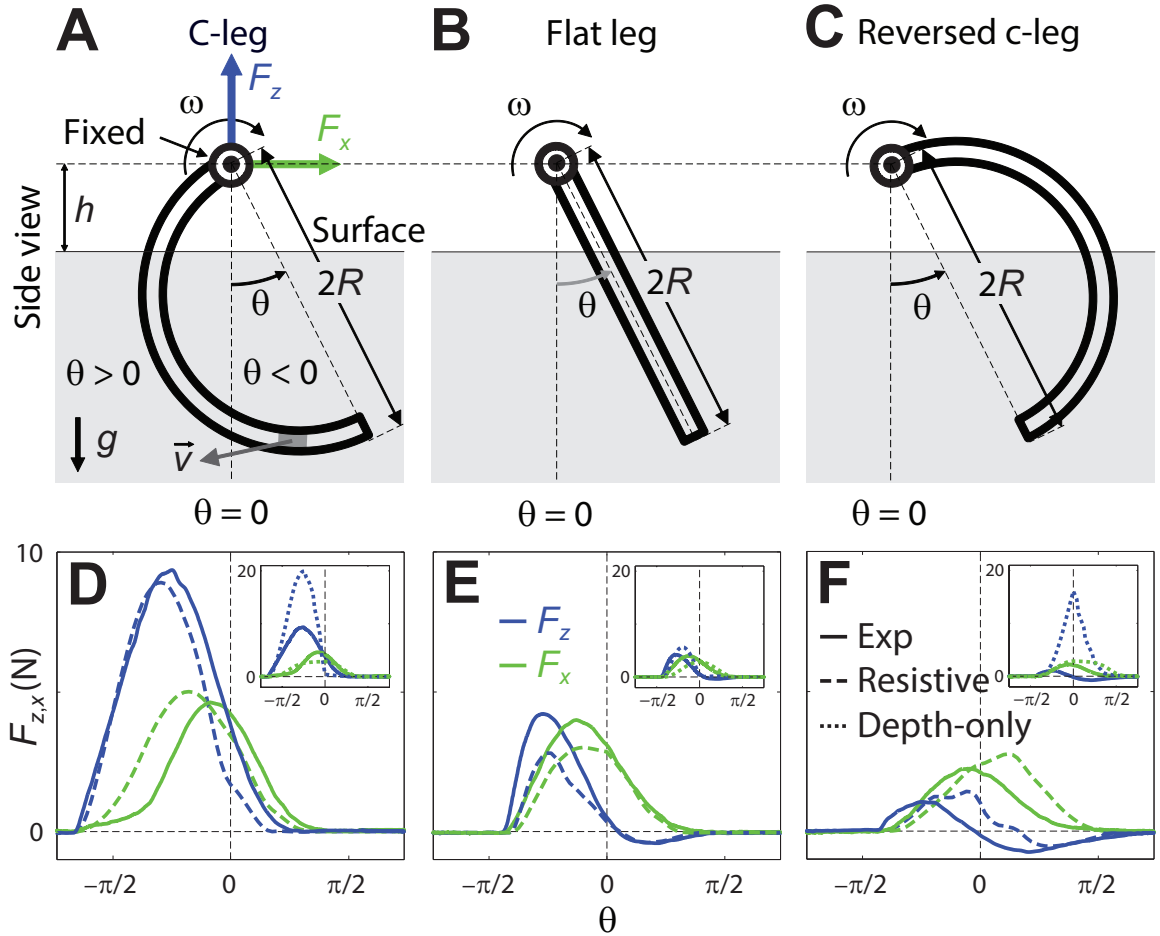


Figure 22: The resistive force model predicts forces on intruders of complex morphology and kinematics moving in granular media. Three thin rigid model legs of different geometries, (A) a c-leg, (B) a flat leg, and (C) a reversed c-leg, were rotated about a fixed axle at a hip height h through granular media (gray area) in the vertical plane at an angular velocity ω , generating leg speeds of $v \sim 1$ cm/s, and net lift F_z (blue) and thrust F_x (green) were measured as a function of leg angle θ . All three legs had identical maximal length $2R$ from the axle. g is gravitational acceleration. (D to F) $F_{z,x}$ versus θ on the three legs measured in the experiment (solid curves) and predicted by the resistive force model (dashed curves) using Eq. 2 (movie S3). Insets: $F_{z,x}$ versus θ from experiment (solid curves) versus predicted (dotted curves) using Eq. 2 and previous force models in which stresses depended only on depth (Figure 54).

the legs

$$F_{z,x} = \int_S \sigma_{z,x}(|z|_s, \beta_s, \gamma_s) dA_s = \int_S \alpha_{z,x}(\beta_s, \gamma_s) |z|_s dA_s, \quad (7)$$

where S is the leading surface of the leg; dA_s , $|z|_s$, β_s , and γ_s are the area, depth below the surface, angle of attack, and angle of intrusion of infinitesimal leg elements; and $\alpha_{z,x}(\beta_s, \gamma_s)$ are element stresses per unit depth (interpolated from data in Figure 21, B and C). To test the robustness of our force model, we used three model legs of different geometries (with the same maximal leg length $2R$): a RHex robots c-leg [135, 115], a flat leg, and a reversed c-leg (Figure 22, A to C). In model calculations, each leg was divided into 30 elements.

In all media tested (Figure 22, D to F, and Figure 57), we observed that for all three legs, the measured net lift and thrust $F_{z,x}$ as a function of leg angle θ (solid curves) were asymmetric to the vertical downward direction ($\theta = 0$), and were larger during intrusion ($\theta \leq 0$) than during extraction ($\theta \geq 0$). Peak $F_{z,x}$ were largest on the c-leg and smallest on the reversed c-leg. The reversed c-leg experienced significant negative lift (suction force, $F_z < 0$) during extraction. For all media tested, our resistive force model predicted $F_{z,x}$ versus θ for all three legs (dashed curves), capturing both the magnitudes and asymmetric profiles. The relative errors of peak forces between data and model predictions were within 10% for the c-leg in four media tested, and within 33% for all three legs in all media tested. The accuracy of our resistive force model was significantly better than that of previous force models in which stresses depended only on depth (Figure 22, D to F, insets; Figure 54). Furthermore, our resistive force model revealed that the c-leg generated the largest forces, because its morphology allowed leg elements to not only reach deeper depths but also access larger stress regions in Figure 21, B and C (particularly for elements at large depths).

Our discovery of the insensitivity of the stress profiles to particle properties (Figure 56) has practical benefits: For granular media of near-monodispersed, near-spherical, rounded particles, as an alternative to measuring $\alpha_{z,x}$ for all attack angles β and intrusion angles γ in the laboratory, one can simply perform a single measurement [of $\alpha_z(0, \pi/2)$, using a horizontal plate penetrating vertically downward] to infer all $\alpha_{z,x}(\beta, \gamma)$ by a scaling routine (supplementary text section 3 and Figure S9) and predict forces (with a small loss in accuracy for the c-leg and the flat leg, but a larger loss in accuracy for the reversed c-leg, Figure 60).

2.3.3 Prediction of robot performance using RFT

We tested the ability of our resistive force model to predict legged locomotion. We chose to study the locomotor performance (speed) of a small RHex-like robot [115] (Figure 23A, top) moving on granular media. The robot's six legs rotated nearly entirely in the vertical plane during locomotion, and its small size ensured that leg intrusion speeds were low enough for particle inertia to be negligible. We chose poppy seeds as the test granular medium, because the grains were both small enough to be prepared in our fluidized bed track [135] and large enough to not jam the robot's motor and gear trains. The robot's legs had a similar friction coefficient with poppy seeds to that of the model legs and were sufficiently rigid so that they experienced negligible bending during movement.

Unlike the sand-swimming lizard, which moves within granular media quasistatically (thrust and drag are always roughly balanced) [142], legged locomotion on the surface of granular media is dynamic (forces are not always instantaneously balanced). As a result, the resistive force theory (which solves for speed by balancing forces) [131, 142] cannot be directly applied. Thus, to use our resistive force model to calculate robot speed, we developed a three-dimensional multibody dynamic simulation of the robot (Figure 23A, bottom) (28). The simulated robot had the same body

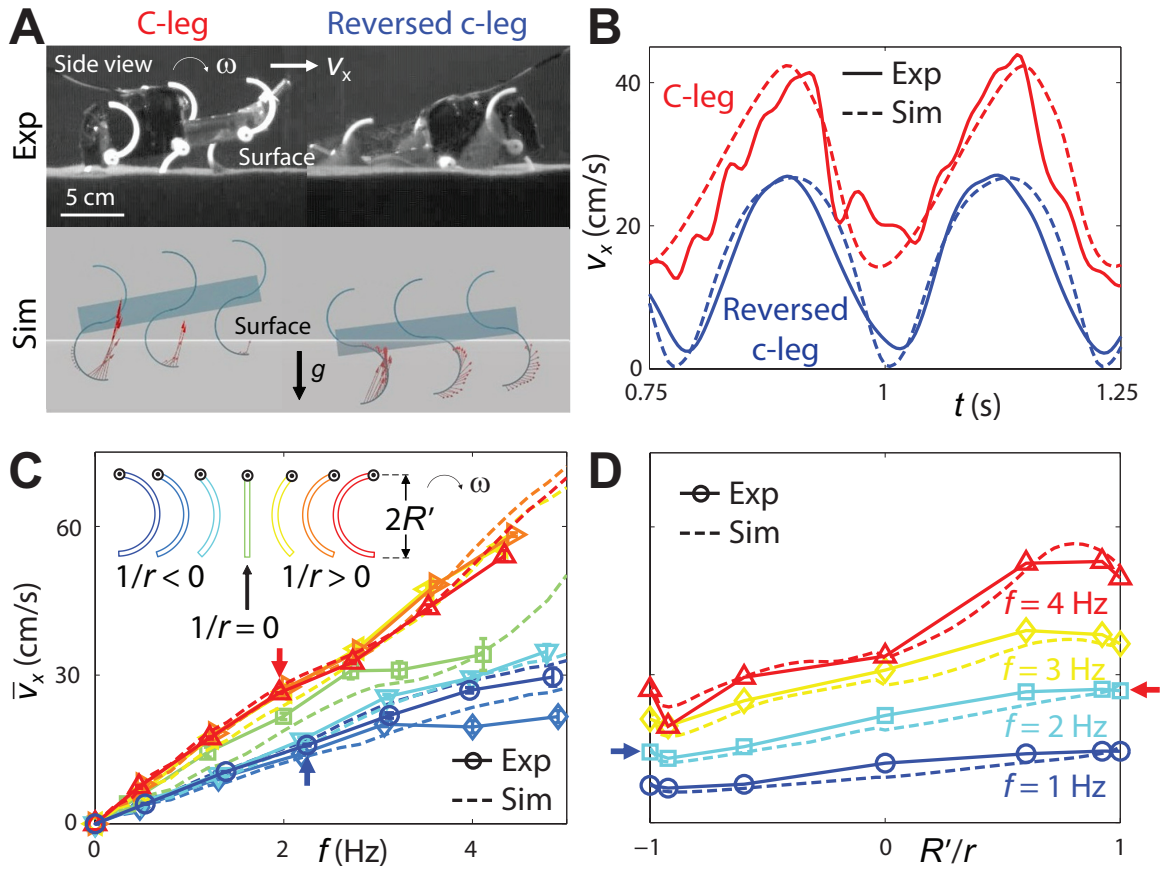


Figure 23: A multibody dynamic simulation using the resistive force model predicts legged locomotion on granular media. (A) Side views of a small RHex-like robot at mid-stance during locomotion on granular media, using c-legs (left) and reversed c-legs (right) in the experiment (top) and simulation (bottom). Arrows in the simulation indicate element forces on one tripod of legs. g is gravitational acceleration. (B) Forward speed v_x versus time t from two representative runs using c-legs (red, stride frequency $f = 2.0$ Hz, curvature $1/r = 1/R$) and reversed c-legs (blue, $f = 2.2$ Hz, $1/r = 1/R$). (C) Average forward speed Embedded Image versus f using legs of seven curvatures $1/r$ transitioning from reversed c-legs to c-legs (inset), where r is the radius of curvature, $2R$ is the maximal length of the robot legs, and the minus sign denotes reversed legs. (D) Embedded Image versus $1/r$ at $f = 1, 2, 3,$ and 4 Hz. In (B) to (D), solid and dashed curves indicate the experiment and simulation, respectively. Error bars in (C) denote ± 1 s.d. ($\ll 1$ cm/s in the simulation). Experimental data in (D) are interpolated from those in (C) (hence no error bars). Red and blue arrows in (C) and (D) indicate averages from data shown in (B).

and leg morphology and used the same alternating tripod gait as the actual robot and had its motion constrained in the vertical plane. We divided each body plate and leg into 30 elements. The velocity \mathbf{v} and angular velocity $\boldsymbol{\omega}$ of the simulated robots body were calculated by solving the Lagrangian equations of the robotic system, provided the net force and torque calculated from our resistive force model by the integration of stresses over each leg and the body using Eq. 2. To test the robustness of our resistive force model and simulation, we used legs of seven geometries with different curvatures $1/r$ (given maximal leg length $2R$) (Figure 23C, inset) and varied stride frequency f to up to 5 Hz.

We observed similar robot kinematics (Figure 23A) and forward speed v_x versus time t (Figure 23B) in both the experiment and simulation. The robot moved faster and penetrated its legs less deeply during stance using c-legs (Figure 23A, left; Figure 23B, red) than using reversed c-legs (Figure 23A, right; Figure 23B, blue). Average forward speed \bar{v}_x increased with stride frequency f for legs of all curvatures $1/r$ and was lower at any f using legs of negative curvatures than using legs of positive curvatures (Figure 23, C and D). The agreement between experiment and simulation in $\bar{v}_x(f, 1/r)$ was remarkable: Errors were within 20% for 90% of the f and $1/r$ tested and within 35% for all the f and $1/r$ tested. Simulation using our scaling routine also achieved reasonable accuracy (Figure 53). This was an improvement over simulation using previous force models in which stresses depended only on depth (Figure 65).

Our resistive force model and simulation revealed that the robot moved faster using c-legs than using reversed c-legs, because whereas the c-legs penetrated less deeply, their elements accessed larger stress regions in Figure 21, B and C, resulting in larger leg lift (Figure 66) and smaller body drag. Our model and simulation also allowed the prediction of ground reaction forces on granular media (Figure 23A, red arrows, and Figure S13), which would be difficult to measure otherwise. Furthermore, our model and simulation predicted that using arc-like legs (given maximal leg length

2R) of an optimal curvature of $1/r = 0.86/R$, the robot would achieve maximal speed of $\bar{v}_x = 72 \text{ cm/s}$ (≈ 5 body length/s) at 5 Hz. Our approach affords significant reduction in the computational time needed to model movement on granular media. For example, relative to our multiparticle Discrete Element Method (DEM) simulation of movement on granular media [231, 63], our simulation using the resistive force model can achieve a factor of 10^6 in speed-up (e.g., 10 s versus 30 days using DEM to simulate 1 s of locomotion on a granular bed of 5×10^6 poppy seeds).

2.4 Further discussions

2.4.1 Application to natural sand

We tested the predictive power of our scaling routine (Figure 61) for two highly polydispersed, nonspherical, highly angular natural sands (Figures 62, 63 and 64, and Table 6)¹. We found that the model accuracy for natural sands was slightly worse than found in the glass spheres and poppy seeds (for example, 35% versus 20% error in peak F_z for a rotating c-leg). As was the case for the near-spherical granular media tested, the functional forms of forces on the c-leg and the flat leg were still well captured by our scaling routine. Furthermore, the overestimation was not affected by reducing the polydispersity of the natural sand. This suggests that the nonsphericity and angularity of natural sand particles [43] may be the cause of this overestimation, which may require additional model fitting parameters and scaling factors. Our model is intended for dry sand (~ 0.1 to ~ 1 mm in particle diameter [19]) and may not work for dry cohesive powder ($\leq \sim 0.01$ mm) [40]. We do not expect our model to work if the particle size approaches a characteristic length of the locomotor (for example, ~ 1 cm particles for our robot of ~ 1 cm foot size), so that the continuum assumption breaks down and particles effectively become boulders. We also do not expect our model to capture wet, cohesive flowable media such as soil and mud.

¹Details can also be found in Appendix A

2.4.2 Application to weakened granular media

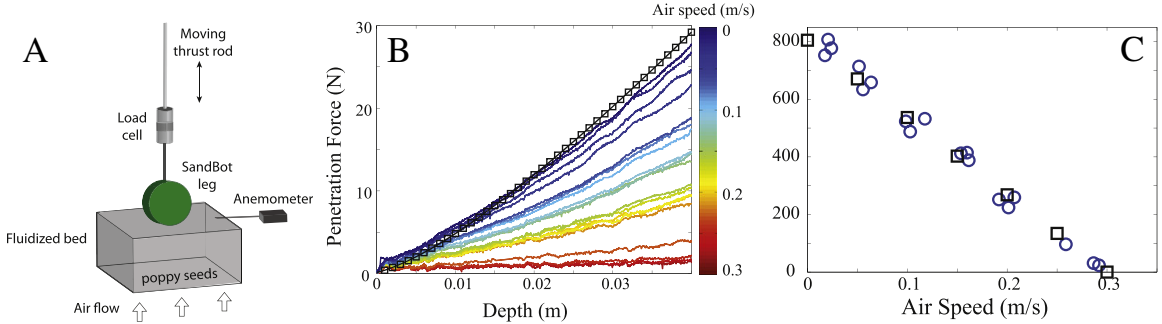


Figure 24: Experiment setup and force measurement for the penetration experiment. (A) Diagram of penetration experiment. (B) Vertical force on a $w = 3.7$ cm, $R = 3.8$ cm SandBot cylindrical leg versus depth during penetration of ≈ 1 mm diameter poppy seeds at various air fluidization speeds from 0 to $0.3 \text{ m} \cdot \text{s}^{-1}$. Colors represent air speeds. (C) Vertical penetration resistance, k , versus air flow speed. Blue circles and black squares represent the slope of vertical force per unit depth from experiment and RFT simulation, respectively. Figure reproduced from [175].

Locomotor performance is sensitive to mechanical properties of the ground, which vary widely among different terrestrial environments. Using an air-fluidized bed, we can systematically control penetration resistance of granular media via continuous upward air flow. Recently, we studied locomotion performance of the larger SandBot (~ 2.5 kg, ~ 30 cm RHex-like robot, Figure 25A) walking on a weakened granular substrate. We measured the vertical ground reaction force F_z (Figure 24B, solid lines), and computed the penetration resistance $k = F_z/|z| = A\alpha_z(0, \pi/2)$ (force per depth, blue circles in Figure 24C) on a cylindrical leg (Figure 24A) of SandBot under different air flow speeds v_{air} . Though air flow potentially adds more complications to the system, k in experiments decreased approximately linearly with increasing v_{air} (below the onset of fluidization). We posited that the angular dependence map $\alpha_{z,x}$ was preserved under the air flow. The decrease of granular resistance was then modeled by a single scaling factor (like ζ in the generic stress calculation in Appendix A). The modified RFT captured the penetration force (Figure 24B, the black solid line with squares) and resistance (Figure 24C, black squares) on the leg. We then used the

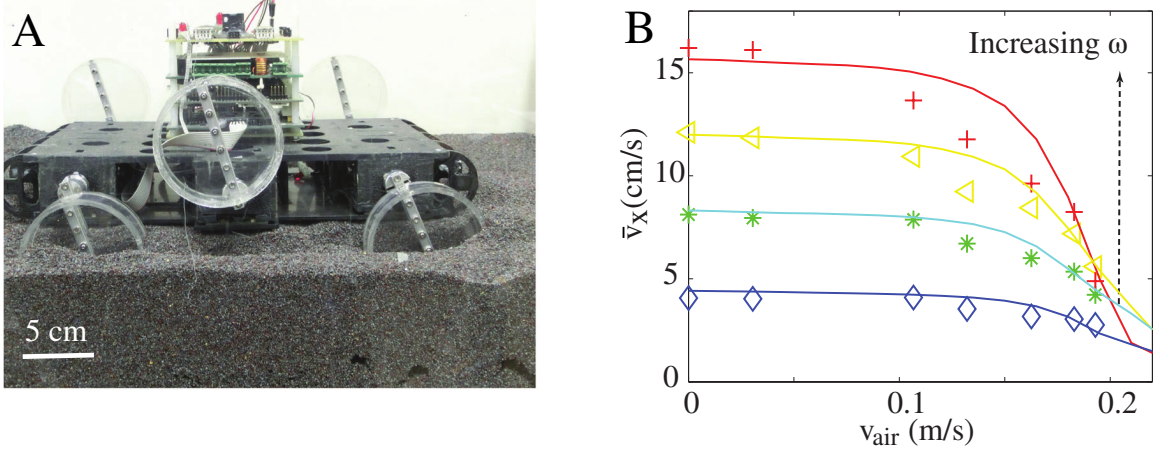


Figure 25: (A) SandBot with cylindrical wheels. (B) Average forward speed \bar{v}_x of SandBot on poppy seeds as a function of air flow speed for different leg rotation frequencies ($\omega = 2, 4, 6, 8$ rad/s, from blue to red). Solid curves correspond to RFT model predictions. Figure reproduced from [230].

extended terradynamics to predict the locomotion speeds of SandBot. The average forward speed \bar{v}_x vs. v_{air} in terradynamic simulations (Figure 25B, solid lines) and experiments (Figure 25B, symbols) agreed well for low air speed $v_{air} \approx 0$. Though in experiments \bar{v}_x decreased faster with increasing v_{air} than in RFT (especially at the highest frequency $\omega = 8$ rad/s), the model qualitatively captured the experimentally observed failure of the locomotor at large v_{air} .

2.5 Conclusion

We have developed a new approach to predicting legged locomotion on granular media. This terradynamics relies on new resistive force measurements and linear superposition [131, 142, 63]. The general profiles of these resistive force measurements are insensitive (other than magnitudes) to a variety of granular media composed of slightly polydispersed, approximately spherical, rounded particles. Our terradynamics may not be limited to legged locomotion, because the integration of stresses should in principle work for devices of other morphology and kinematics, such as

wheels, tracks, and earth movers moving on granular media [23, 150]. For the particle types tested here, an important addition to our model would be to capture three-dimensional effects [134] and spatial and temporal variation in compaction [135] and slopes [30], and test its validity in the high-speed inertial fluid regime (when leg intrusion speed is 1 m/s, at which particle inertia dominates forces) [231]. Our resistive force model also provides opportunities to test and develop new physics theories of dense granular flow [119]. Finally, we envision that, in concert with aero- and hydrodynamics [71, 161, 219, 131, 222, 166, 129, 67, 229, 128], a general terradynamics of complex ground will not only advance understanding of how animals move [61] at present [219, 131, 222, 166, 129, 67, 28, 39, 102, 134, 30, 73, 218, 142], but also facilitate the development of robots with locomotor capabilities approaching those of organisms [229, 128, 177, 135, 115, 231].

CHAPTER III

DISCRETE ELEMENT SIMULATION OF LEGGED LOCOMOTION ON HOMOGENEOUS GRANULAR MEDIA

The contents of this chapter was edited published in ref. [231]. Experiments were performed by Feifei Qian.

3.1 Introduction

Animals live in the deserts can move rapidly across granular surfaces. For example, the zebra-tailed lizard (*Callisaurus draconoides*, ~ 10 cm, ~ 10 g) can run at speeds over 100 cm/s (10 body length/s) on sand. Unlike SandBot which must penetrate a large portion ($> 70\%$) of its limbs to move on granular media, the lizard is light enough that even while running it only penetrates a small portion ($< 30\%$) of its limbs to generate force [134]. This suggests that a small, lightweight body may confer advantages for locomotion on deformable surfaces such as granular media.

Recent advances in the technique of smart composite microstructures (SCMs) [228] have enabled the development of small, lightweight robots (~ 10 cm, ~ 20 g) [103, 26] such as DynaRoACH (Figure 26A). These robots are similar in size to the zebra-tailed lizard (and many other desert vertebrates and invertebrates [49, 156] and can achieve performance approaching animals (~ 10 body length/s) on solid surfaces. Therefore, in addition to advancing locomotor capabilities of devices on complex terrain [133], these lightweight robots provide promising physical models to study how effective legged locomotion can be achieved on granular (flowable) substrates in small, high-performing animals.

In this chapter we reveal principles of movement of lightweight locomotors on granular media using a combination of laboratory experiment and Discrete Element Simulation (DEM). We perform studies of DynaRoACH on a medium of glass particles. To obtain estimates of ground reaction forces that result in high performance, we integrate the DEM simulation with a multi-body dynamic simulation of the robot. Our study reveals for the first time that qualitatively different propulsion mechanisms exist for low- and high-frequency movement on granular media. While the low-frequency locomotion of DynaRoACH can be understood using a previously introduced rotary walking model, at higher frequency, the robot utilizes the hydrodynamic response of the granular medium to achieve high performance through sustained fluidization of the ground. Furthermore, we use the simulation to systematically vary parameters such as friction (particleparticle and particleleg) that are inconvenient to modify in experiment, and demonstrate performance and stability limits. We also investigate how limb width modifies the walkrun transition. We expect that the mechanics discovered here and the tools we have developed should be applicable to other devices and provide a starting point to understand biological locomotion and develop robot designs on more complex deformable substrates, such as leaf litter and mud.

3.2 Materials and methods

3.2.1 Experiment platform

Robotic platform The DynaRoACH robot used in this study (Figure 26A) is a small, lightweight (10 cm, 25 g), bio-inspired hexapedal robot [103]. It has six c-shaped legs (radius 1 cm) and runs with an alternating tripod gait. All six legs are driven by a single motor through body linkages. The motor is controlled by a centralized controller mounted close to the center of mass (CoM) of the robot. Control parameters such as the stride frequency, running time, and PID control gains are set on a PC and communicated to the controller through a Bluetooth wireless interface.

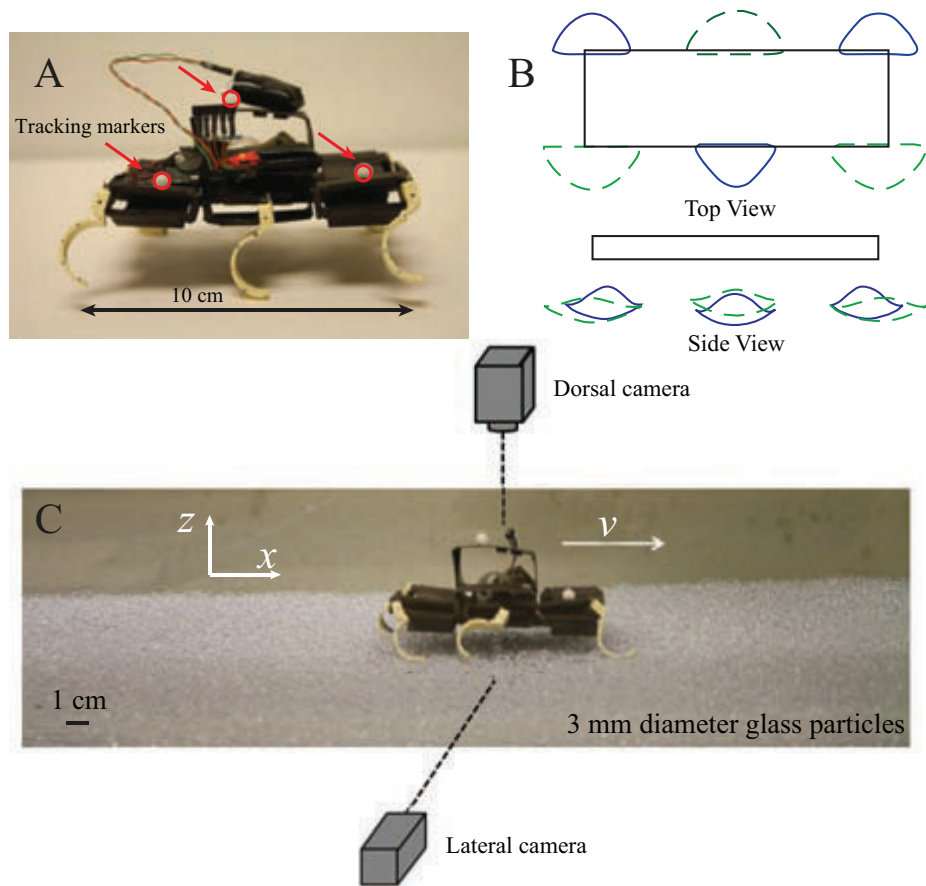


Figure 26: The lightweight, hexapedal DynaRoACH robot resting on a bed of 3 mm diameter glass particles. (B) Leg tip trajectories from top view and side view. Solid blue and dashed green trajectories denote the two alternating tripods. (C) High-speed video experimental setup.

We used 3.0 ± 0.2 mm diameter glass particles (density = 2.47 g/cm³) as the granular medium (Figure 26C). The large size of the particles reduces computation time in the simulation portion of the study, facilitating a direct comparison between experiment and simulation. While these particles are larger than most natural sand grains, they have similar qualitative behavior in response to intrusion; a previous study [143]) also demonstrated that these particles provided a good model material for studying locomotion (swimming) within granular media.

In our study, we prepared the granular medium into a closely packed state ($\phi = 0.63$). However, we found that our results did not qualitatively change for different ϕ (e.g. robot speed was insensitive to ϕ), likely because the robot penetrated its legs into the granular medium to depths of only a few particle diameters and the range of achievable ϕ was small ($0.61 < \phi < 0.63$) in the low-friction 3 mm particles.

We ran the DynaRoACH robot on a 75 cm long, 30 cm wide trackway filled with the 3 mm diameter glass particles to a depth of 6 cm (Figure 26C). We pressed the particles using a flat plate before each trial to prepare the particles to a closely packed state. Running kinematics were captured by two high-speed video cameras (AOS X-PRI) from both top and side views at a frame rate of 200 fps. One high-contrast dorsal marker was bonded above the robot CoM to obtain average forward speed; two lateral markers were bonded on the front and rear of the robot body to obtain CoM height (approximated by the average vertical position of the two markers). Stride frequency was determined from the videos.

To capture prescribed leg trajectories, the robot was suspended in the air and the trajectories of the leg tips were recorded as the motor rotated. During a cycle, each leg rotated backward about the hip (retraction), lifted-up sideways, and swung forward (protraction) (Figure 26B). Leg kinematic parameters such as the foreaft swing angle and lateral lifting angle were determined by tracking the markers on the legs and used to guide tuning of leg trajectories in simulation. We define a stride period T as the

time between the start of two consecutive retraction phases, and stance as when the leg generates ground reaction force (determined from simulation).

3.2.2 Simulation

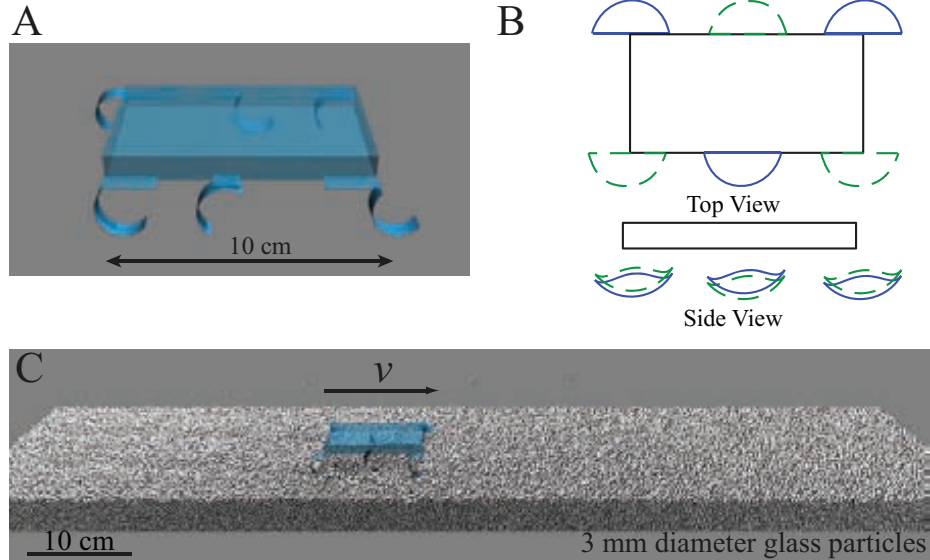


Figure 27: (A) Simulation of the robot using MBDyn. (B) Leg tip trajectories in simulation. (C) Simulation of the robot running on a bed of 3 mm particles.

In the simulation, we use the contact force model given by Equation 2, with $k_n = 2 \times 10^6 \text{ kg} \cdot \text{s}^{-2} \cdot \text{m}^{-1/2}$ and $g_n = 15 \text{ kg} \cdot \text{s}^{-1} \cdot \text{m}^{-1/2}$. We set $\mu_{pp,pl} = \{0.1, 0.3\}$ the particleparticle and particleleg friction coefficients. The restitution and friction coefficients were experimentally measured and validated in a rod drag experiment [143]. Once the parameters were set in the DEM simulation, the robot locomotion could be accurately predicted over a wide range of conditions. The simulated granular bed (3×10^5 particles) was 60 PD (particle diameters) in width, 15 PD in depth, and 290 PD in length, and had frictionless boundaries (Figure 1F). At low frequencies we used a shorter granular bed (90 PD) containing 1.1×10^5 particles to save computation time.

To model the robot we used a multi-body dynamic simulator, MBDyn [83, 24], which allows time domain simulation of multi-body mechanical systems from first

principle equations (Equation 3). MBDyn features a full 3D simulation with six translational and rotational degrees of freedom. This is essential for locomotion on the surface during which pitch, roll, and yaw are often present [133]. In the dynamic simulation, the robot was constructed with similar body and leg geometries as the actual robot (Figure 27A). The simulated robot was composed of 13 individual rigid parts: one box-shaped body, six c-shaped legs, and six linking plates between legs and body. The legs of the actual robot were not perfectly rigid but experimental observations showed little leg deformation during locomotion on granular media. The joints between the link plates and c-shaped legs allowed frontback swing of the legs while the platebody joints allowed sideways lifting of the legs. Tuning kinematic parameters for the joint movements produced leg trajectories (Figure 27B) that resembled experimental measurements (Figure 26B) without mimicking the internal linkage of the actual robot.

We combined MBDyn with the DEM code to simulate robot locomotion on granular media via a communication interface (a UNIX socket using C++). At each time step, MBDyn integrated the equations of motion for the robot combined with the forces and torques calculated from the DEM code. The updated kinematics including position, orientation, velocity, and angular velocity of each part of the robot were then passed back to the DEM code to compute the forces and torques on all interacting elements at the next time step. The time step was $2.5 \mu s$, although setting it to $1 \mu s$ did not change the results; the time step was determined by typical particle overlap times in DEM. In addition to the kinematics during locomotion (e.g. CoM position and velocity, stride length, limb penetration depth), the dynamics during locomotion (e.g. net ground reaction force on each limb and tripod) were also determined from the simulation.

3.3 Results and discussion

3.3.1 Kinematics

From measurements in simulation of the instantaneous speed of the robot (see Figure 28), we computed time-averaged forward speed. The speed of the robot measured in both experiment and simulation (Figure 29A) agreed well, and increased monotonically with stride frequency. At the highest stride frequency tested in experiment (12 Hz), the robot reached a speed of 50 cm/s (5 body length/s), comparable to slow runs of the zebra-tailed lizard. Calculated stride length (Figure 29B) decreased with stride frequency from low (0 – 3 Hz) to intermediate frequencies (4 – 6 Hz) but increased with stride frequency at high frequencies (7 – 12 Hz). Duty factor (the percentage of the total stride period during which the limb is in contact with the ground) measured in simulation (Figure 28E and J) fell below 0.5 at intermediate frequencies of ~ 6 Hz (Figure 29C), indicating the onset of aerial phases. Closer examination of the kinematics revealed that the robot displayed a transition in locomotor mode as stride frequency increased.

At low stride frequencies (e.g. 3 Hz, Figure 28A–E), as predicted, the DynaRoACH robot used a quasi-static rotary walking locomotor mode, where forward speed increased sub-linearly with stride frequency (i.e. stride length decreased; Figure 29B). Instantaneous forward speed also increased from 0 to 25 cm/s during most of stance and then dropped to zero (Figure 28C). Vertical position of the CoM simulation (Figure 28B and D) showed that average body height was 1.28 ± 0.03 cm during stance, increased by 0.46 ± 0.03 cm (38% of the standing body height 1.2 cm) during most of stance, and then decreased by the same amount.

The observed decrease in stride length with stride frequency, increase in body height and forward speed during most of stance, and decrease in body height and forward speed between stances were in accord with predictions of the rotary walking model (Figure 29A and 3B, red curve) [135]. This suggests that like SandBot,

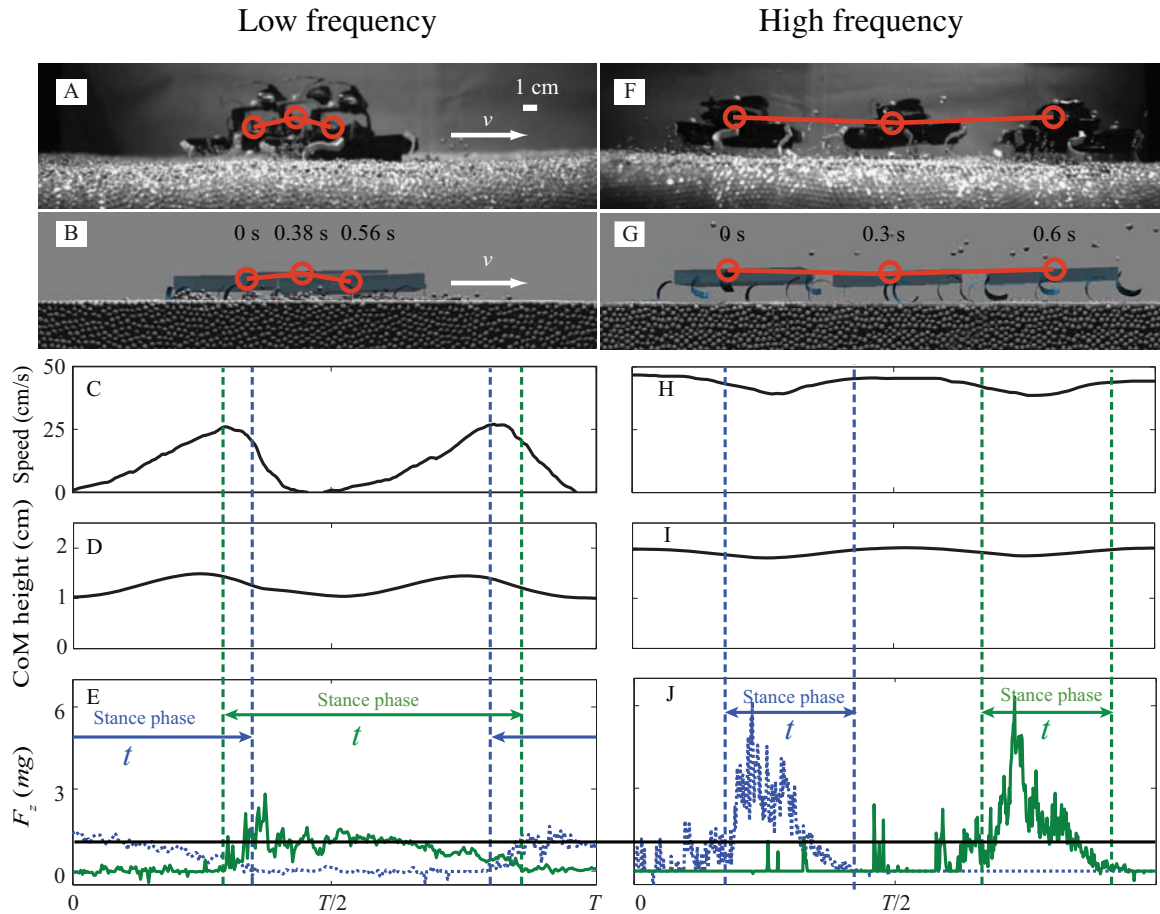


Figure 28: Two locomotion modes observed for the robot moving on granular media: (A)-(E) walking at low frequencies (e.g. 3 Hz); (F)-(J) running at high frequencies (e.g. 11 Hz). (A), (F) Sideview of the robot in experiment. (B), (G) Sideview of the robot in simulation. (C), (H) Instantaneous forward speed versus time. (D), (I) Body height versus time. (E), (J) Vertical ground reaction force on a tripod versus time. Dashed blue curve and solid green curve are for the two alternating tripods. Black horizontal line indicates body weight (mg). In (A), (B) and (F), (G) the three time instants shown are the start, middle, and end of three different stances. In (C)(E) and (H)(J) data are shown for simulation only. Duty factor is stance duration t divided by stride period T .

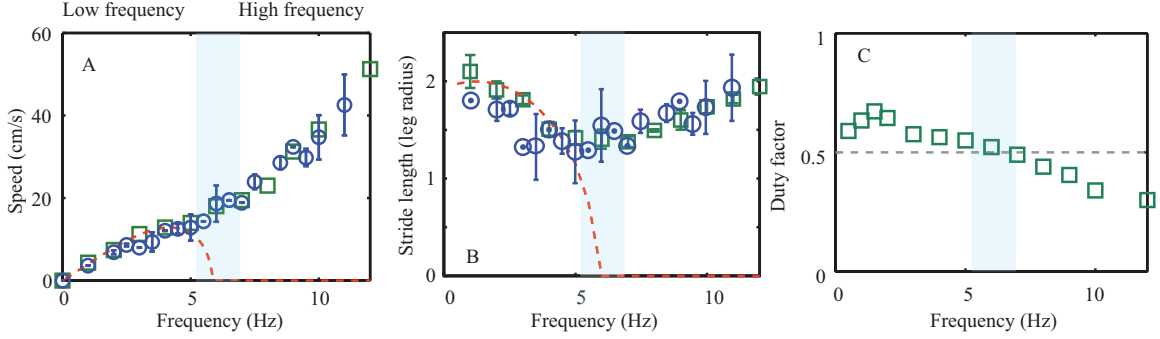


Figure 29: Performance and gait parameters (blue circles: experiment; green squares: simulation): (A) average forward speed versus stride frequency; (B) stride length versus stride frequency; (C) duty factor versus stride frequency (simulation only). Blue region indicates where transition of locomotor mode occurs. Dashed red curves in (A, B) are predictions from the rotary walking mode [135]. Error bars indicate standard deviation.

the small DynaRoACH robot also rotary-walked on solidified granular media at low frequencies. The decrease in body height and forward speed occurred at the start of stance; however, this does not contradict the rotary walking model, but is a consequence of the different leg trajectories of the small robot and SandBot. Because SandBot rotates its legs in circular trajectories, its body must rest on the surface between two tripods, resulting in stance phase that begins during the retraction phases of legs. The DynaRoACH robot instead uses protractionretraction leg trajectories, which result in stance phases that begin during protraction phases of the legs.

At high stride frequencies (Figure 28F–J, 11 Hz) the DynaRoACH robot exhibited a different locomotor mode than that predicted by the rotary walking model. The forward speed of DynaRoACH increased super-linearly with stride frequency (i.e. stride length increased; Figure 3B). Instantaneous forward speed was always greater than zero and decreased during the first half of stance. It then increased during the second half of stance (Figure 28H). The average body height measured in simulation was 1.86 ± 0.02 cm above the surface (Figure 28F, G, I), which was 0.58 cm (48% of the standing body height 1.2 cm) higher than that at low frequencies. Body height decreased by 0.19 ± 0.02 cm (16% of the standing body height 1.2 cm) during the

first half of stance and increased by the same amount during the second half of stance. Simulation revealed that grains around the intruding legs remained fluidized throughout the stance phase.

While these kinematics were different from those predicted by the rotary walking model (Figure 29A and B, red curve), they also differed from the slow surface swimming which SandBot used at high stride frequencies [135], in which the body height remained constant while the belly lay on the surface and forward speed was small (~ 1 cm/s). For DynaRoACH running on granular media at high frequencies, we observed a decrease in body height and instantaneous forward speed during the first half of stance, a monotonic increase of average forward speed with stride frequency, and aerial phases observed. These signatures were also observed in the zebra-tailed lizard running on granular substrates [134]; that study revealed that the lizards movement could be described by a springloaded inverted pendulum (SLIP) model [28]. This similarity suggested that unlike SandBot, but like the zebra-tailed lizard, the small robot used a SLIP-like running mode on granular media at high frequencies.

3.3.2 Ground reaction force

To understand the mechanism of the transition in locomotor mode from walking at low frequencies to running (but not swimming) at high frequencies, we examined in simulation the vertical ground reaction force, F_z , on a tripod of legs. For animals and legged robots moving on deformable or yielding substrates such as the surface of water [84] or granular surfaces [134], it is critical that the material generates sufficient F_z to balance the weight and inertial force of the body before legs sink too deeply into the substrate. Averaged over a cycle, lift must equal the body weight, i.e. $\frac{1}{D \cdot T} \int F_z dt = mg$, where mg is the body weight of the robot, T the cycle period, and D the duty factor defined as the stance duration divided by T .

At low stride frequencies (e.g. 3 Hz), because duty factor was greater than (but

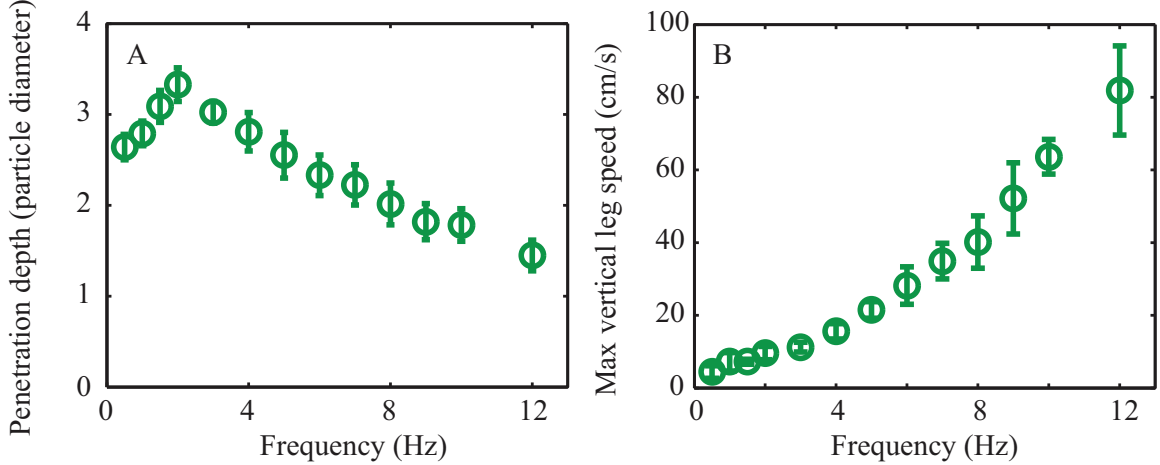


Figure 30: Limb penetration and intrusion speed measured in simulation. (A) Maximum leg penetration depth (measured in particle diameters) versus stride frequency. (B) Maximum leg vertical penetration speed versus stride frequency. Error bars indicate standard deviation.

close to) 0.5, F_z on both tripods was close to the body weight for most of the cycle (Figure 28E). As duty factor decreased below 0.5 with increasing stride frequency, F_z on both tripods no longer overlapped, and the magnitude of F_z on each tripod increased. The peak of F_z increased from $\sim 1 mg$ at 3 Hz (Figure 28E) to $\sim 6 - 7 mg$ at 12 Hz (Figure 28J). Peak torque on a tripod about the hips measured in simulation at 12 Hz was 10 mN-m; this was less than the stall torque of the motorgearbox system.

The rotary walking model can only explain the mechanism governing the increase in F_z at low frequencies. At low frequencies (< 3 Hz), the granular force is friction dominated, and therefore is independent of intrusion speed and increases with penetration depth. As stride frequency increased, this depth-dependent granular force increased due to the increasing inertial force associated with the lifting of the body [135]; this resulted in an increasing penetration depth (Figure 30A). As stride frequency increased to > 3 Hz, however, the measured leg penetration depth decreased (Figure 30A), counter to the prediction of the rotary walking model. In this regime the walking model also predicted a decrease in the lift force on the legs, contrary to observations (Figure 28E and J).

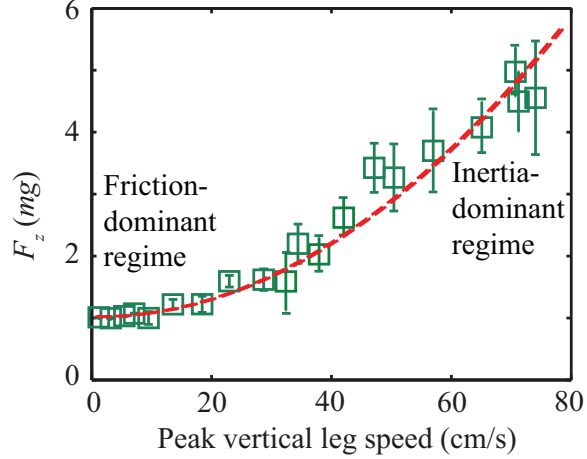


Figure 31: Vertical ground reaction force versus maximum leg penetration speed. Dashed red curve indicates quadratic fit $F_z/mg = \alpha v^2 + 1$ with fitting parameter $\alpha = 5.7 \times 10^{-3} \text{cm}^{-2} \text{s}^2$. Error bars indicate standard deviation.

This discrepancy suggests that there must be additional contribution to the force at high frequencies. Examination of leg kinematics in simulation revealed that the vertical penetration speed of the legs increased with stride frequency and reached nearly 1 m/s at 12 Hz (Figure 30B). It is known that the granular forces during high-speed impact are hydrodynamic-like and increase approximately quadratically with impact speed [120, 85]. Our data of lift versus vertical leg penetration speed (Figure 31, green squares) can be described approximately by a quadratic with a non-zero y-intercept (Figure 31, dashed red curve), due to the finite yield stress of the medium. We hypothesize that as the vertical leg penetration speeds increases, the inertial force of the grains being accelerated by the legs becomes important and contributes significantly to the vertical ground reaction force. In other words, at high frequencies, the robot runs on granular material that behaves like an inertial fluid, much like the basilisk lizard (*Basiliscus*), the so-called Jesus lizard that runs on the surface of water [84].

We used previous intrusion studies in granular media to estimate the transition

frequency for the DynaRoACH robot. Studies of horizontal drag in granular media [7] suggest that inertial effects become important for intrusion speeds beyond $v_c \sim (2gd)^{1/2}$, where d is the particle diameter and g the gravitational acceleration. For 3 mm diameter glass particles, $v_c = 25$ cm/s. This indicates that hydrodynamic-like force should become significant as the vertical leg penetration speed increases beyond ~ 25 cm/s, or as stride frequency increases past ~ 6 Hz (Figure 30B). This is in accord with the observed transition in locomotor mode around 6 Hz (Figure 29). We posit that this transition of the propulsion mechanism from low-frequency (i.e. low vertical penetration speed) walking on yielding ground to high-frequency (i.e. high vertical penetration speed) running on fluidizing ground is generic to locomotion on granular media. However, the frequency at which the walk-to-run transition occurs should depend on parameters associated with the granular media as well as the robot morphology and kinematics.

The capability of the small robot to run rapidly at high frequencies on granular media by using hydrodynamic-like forces, in contrast to SandBots slow swimming, suggests that lightweight locomotors have an advantage when moving on granular surfaces. Indeed, the small robots legs are relatively large (projected surface area ~ 1.4 cm²) compared with its body weight (25 g) (each leg of a tripod applies a pressure of 600 Pa when standing), and can generate enough hydrodynamic-like lift by paddling its legs rapidly to maintain the body well above the surface. By contrast, SandBots legs are relatively small (projected surface area ~ 5 cm²) compared with its body weight (2300 g) (each leg of a tripod applies a pressure of $\sim 1.5 \times 10^4$ Pa when standing), and cannot generate enough hydrodynamic-like lift to support the body before the legs sink deeply enough to encounter previously disturbed material over steps and trigger swimming. This may explain why the zebra-tailed lizard, the highest-performing among desert lizards of similar size, has the largest hind feet [134, 175]

3.3.3 Parameter variation

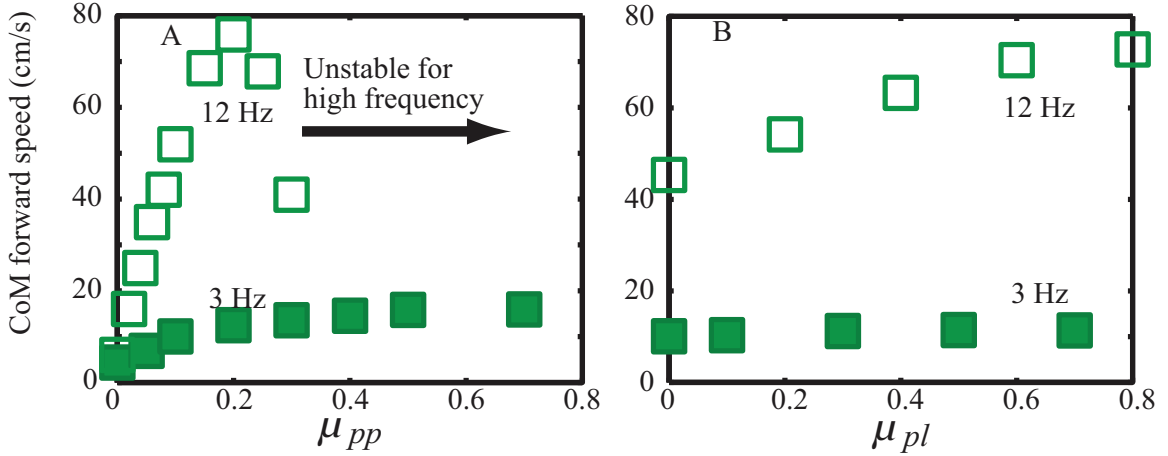


Figure 32: Robot average forward speed upon variation of (A) particleparticle friction μ_{pp} (with $\mu_{pp} = 0.3$) and (B) particle leg friction μ_{pl} (with $\mu_{pp} = 0.1$) in simulation (filled green squares: 3 Hz; empty green squares: 12 Hz).

Because the MBDyn multi-body simulation is based on first principles (i.e. NewtonEuler equations of motion), and the DEM simulation of granular media is based on validated empirical models (e.g. Hertzian contact theory, Coulomb model of friction), our results should be applicable to a broad class of granular substrates. The simulation tool therefore allows rapid and accurate systematic variation of the properties of the locomotor (e.g. leg morphology, leg kinematics) as well as the granular substrate (e.g. size, density, friction, and hardness of particles). For example, while in experiment it is difficult to alter only one property while not changing others, in simulation we can test the effects of each substrate property. This can provide insight for design of future multi-terrain robots, and allows testing of biological hypotheses. To demonstrate the capabilities of our simulation for parameter variation, we varied the coefficients of particleparticle friction μ_{pp} , particleleg friction μ_{pl} , and leg width, and tested the effects of these parameters on the robot speed.

Dramatic changes in locomotor performance were observed when μ_{pp} was varied (Figure 32A). For walking at low frequencies (e.g. 3 Hz, Figure 32A, filled green

squares), the robot speed increased monotonically with μ_{pp} , and saturated at high μ_{pp} . In this regime, forces were dominated by friction (particularly, μ_{pp}). As μ_{pp} increased, the legs needed to penetrate less to balance body weight and inertial forces. As a result, stride length and speed increased with μ_{pp} . The saturation of speed at high μ_{pp} was a consequence of leg penetration depth approaching zero with increasing μ_{pp} . Thus, stride length could not increase further.

For running at high frequencies (e.g. 12 Hz, Figure 32A, empty green squares), the robot speed increased with μ_{pp} for $\mu_{pp} < 0.2$ and decreased with μ_{pp} for $\mu_{pp} > 0.2$. The increase of speed with μ_{pp} for $\mu_{pp} < 0.2$ is likely because the inertial force provided by the particles being accelerated by the legs increased with μ_{pp} . We observed that multiple layers of particles directly under and around the legs were fluidized during leg penetration. We hypothesize that the size of the region of accelerating particles increases with μ_{pp} because larger μ_{pp} facilitates interlocking of the particles. The decrease of speed with μ_{pp} between $0.2 < \mu_{pp} \lesssim 0.4$ for running at high frequencies is likely a result of reduction in propulsion due to an asymmetric gait. We observed that in this regime, the particles became more tightly interlocked and lost fluidity. The lift force on one tripod alone became sufficient to accelerate the robot up such that the body traveled in the air during the remainder of the cycle and the other tripod never touched the ground.

As μ_{pp} increased above ~ 0.4 , the particles became so tightly interlocked that the granular substrate behaved like rigid ground. Locomotion became unstable as the robot bounced erratically, and its movement direction changed randomly. This is similar to the unstable motion of the robot on rigid ground (Li et al., 2010). Forward speed was not well defined in this regime. The perfectly rigid legs of the robot used in simulation may have contributed to this instability by generating force spikes during substrate impact [124]

Particleleg friction μ_{pl} had little effect on the robot speed at low frequencies (e.g. 3

Hz, Figure 32B, filled squares). We observed that the penetration depth and the stride length remained the same when μ_{pl} increased. This indicates that the yielding forces of granular media during low-speed penetration are insensitive to the surface roughness of the c-legs, but instead are dominated by particle particle friction (Figure 32A). We hypothesize that at low frequencies, as the robot rotary walks on solidified particles, ground reaction force results primarily from normal forces on the leading surface (rather than friction on the thin sides) of the c-legs.

At high frequencies (e.g. 12 Hz, Figure 32B, empty squares) the robot speed was sensitive to (and increased with) μ_{pl} . We observed an increase in F_x but not F_z with μ_{pl} (e.g. F_x increased by 50% when μ_{pl} increased from 0 to 0.7 while F_z did not change significantly). Further work is needed to better understand propulsive force in the high-frequency impact-induced fluid-like regime.

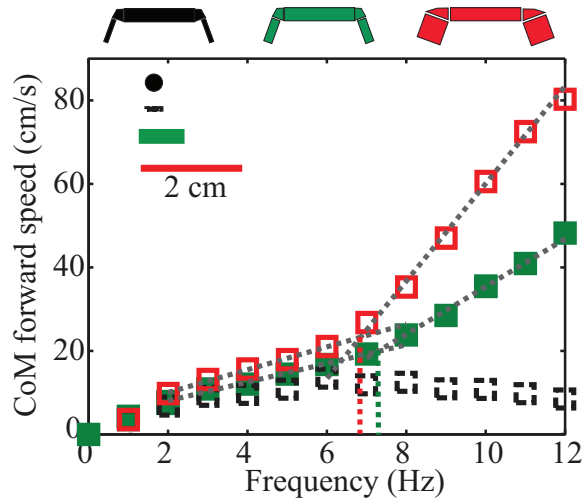


Figure 33: Robot average forward speed versus stride frequency (solid green squares: original foot width of 0.7 cm; dashed black squares: foot width of 0.3 cm; empty red squares: foot width of 2 cm) for different leg widths (in simulation). Horizontal bars in the inset represent the width of the legs. The filled black circle indicates the particle size. Front view of the robot with different leg widths are shown on top. Values of friction coefficients $\mu_{pp,pl} = \{0.1, 0.3\}$ are used. The dashed lines in the 2 cm and 0.7 cm leg widths are separate linear fits to the speed of the robot between the stride frequencies of 2 – 6 Hz and 7 – 12 Hz. The intersection of a pair of lines indicates the transition frequency from rotary-walking-dominated locomotion to fluid-like propulsion.

Because both hydrostatic-like frictional forces [7, 98] and hydrodynamic-like inertial forces [120, 85] are proportional to intruder area, we expected that an increase (or decrease) of the robot leg width would result in increased (or decreased) ground reaction forces. To test how leg size affects locomotor performance and transitions in locomotor modes, in simulation we varied the width of all the six c-legs (Figure 33, top diagrams) while keeping their radius and kinematics fixed.

At low stride frequencies (1 – 3 Hz) the performance of the robot was insensitive to changes in the leg morphology (Figure 33). Because the robot is lightweight, at low frequencies the stride length was near $2r$, the maximal value of the stride length for rotary walking (where r is the leg radius), seen in the original legs (Figure 29B). An increase in the foot width could not increase the stride length significantly beyond $2r$ and thus the forward speed did not increase significantly (Figure 33, filled green squares to empty red squares). When the width of the legs was close to the particle diameter, we postulated that the ground reaction force would no longer linearly scale with the leg area. In the lowfrequency regime we observed that the penetration depth increased by only 33% when the foot width was reduced to half of the original width. As a result, the stride length and speed did not drop substantially (Figure 33, filled green squares to dashed black squares).

In contrast, at high stride frequencies the robots performance depended sensitively on the leg width. We observed that increasing the leg width by 3 times (from 0.7 cm to 2.0 cm) increased the stride length (and, thus, the average speed) by up to 1.7 times (Figure 33, from filled green to empty red). Surprisingly, the frequency at which the robot switched from rotary-walking behavior to fluid-like propulsion was insensitive to leg width. We determined the transition frequencies from the intersection of linear fits to the speed of the robot in two regions, 2 – 6 Hz and 7 – 12 Hz (Figure 33, dotted gray lines). We found that the transition frequencies decreased by only 0.5 Hz (about 6%) when the leg width increased by 3 times. Transition frequencies measured from

duty factor (i.e. the frequency at which duty factor = 0.5) also showed a decrease by ~ 1 Hz (10%). This implies that the relationship between foot area and average speed is non-trivial. We hypothesize that it is governed by a nonlinear interplay of body inertia and complex intrusion rheology. Advances in the physics of intrusion and impact [191, 44] are required to develop a fundamental understanding of such interactions. In addition, decreasing the leg width by 50% (from 0.7 cm to 0.3 cm) (Figure 33, filled green to dashed black) resulted not only in decreased speeds at low frequencies, but also triggered a transition of locomotor mode from running to slow swimming (similar to that observed in SandBot [135]).

3.4 conclusion

Inspired by high-performing desert animals moving on granular media, we studied in experiment the locomotion of a lightweight, bio-inspired, legged robot (DynaRoACH) on a granular substrate and developed an experimentally validated computer simulation of the locomotion. Our approach enabled examination of the mechanics responsible for the robots high locomotor performance. DynaRoACH displayed a transition in locomotor mode from walking at low frequencies to running at high frequencies. At low frequencies, hydrostatic-like forces generated during yielding of the granular material ultimately led to solidification of the material, and the robot moved as if it were walking on a solid surface. At high frequencies, however, the inertia of the grains being accelerated became important and forces became hydrodynamic-like. In this regime the robot ran rapidly by paddling legs on fluidized granular material. Thus our results reveal that lightweight robots can achieve high locomotor performance on granular media by exploiting the fluid-like properties of these substrates.

The experimentally validated simulation of the lightweight robot platform provides the most accurate model to date of robot locomotion on granular media, and therefore enables detailed examination of the mechanics of legged locomotion over a wide range

of flowable substrates. In particular, the simulation tool we have developed can be used to systematically test the effect of both locomotor and substrate properties on locomotor performance. Practically this can guide the design, control and power consumption estimates for high-performing multi-terrain robot platforms.

Finally, we note that while the approach described here allows detailed investigation of mechanics of movement, a complementary approach is needed: the development of low-order dynamical models [136] that can be used to gain insight into the critical mechanics of dynamical running. In our future work, we will investigate whether a dynamic force relationship that describes the hydrodynamic-like forces during high-speed leg intrusions can be obtained from measurements in DEM simulation. We posit that a generalized locomotion model similar to the SLIP [28] can be developed based on such a force relationship and can extend our current study to more generalized conditions. This generalized model will shed light on the locomotor dynamics of legged animals and robots on granular media, as well as guide development for analytically tractable low-order models.

CHAPTER IV

DETERMINISTIC TRANSPORT IN HETEROGENEOUS ENVIRONMENT

The chapter contains an ongoing work made possible by collaborating with Prof. Predrag Cvitanović.

4.1 Introduction

The advances in the theory of dynamical systems have brought a new life to Boltzmann's mechanical formulation of statistical mechanics, especially for systems near or far from equilibrium, and yielded new sets of microscopic dynamics formulas for macroscopic observables such as the transport coefficients. Sinai, Ruelle and Bowen (SRB) have generalized Boltzmann's notion of ergodicity for a constant energy surface for a Hamiltonian system in equilibrium to dissipative systems in nonequilibrium stationary states [198, 183, 29]. In this more general setting the attractor plays the role of a constant energy surface, and the SRB measure is a generalization of the Liouville measure. Such measures are purely microscopic and indifferent to whether the system is at equilibrium, close to equilibrium or far from it. "Far from equilibrium" in this context refers to systems with large deviations from Maxwell's equilibrium velocity distribution. Furthermore, the theory of dynamical systems has yielded new sets of microscopic dynamics formulas for macroscopic observables such as diffusion constants, to which we turn now.

The classical Boltzmann equation for evolution of 1-particle density is based on stosszahlansatz, neglect of particle correlations prior to, or after a 2-particle collision. It is a very good approximate description of dilute gas dynamics, but a difficult

starting point for inclusion of systematic corrections. In the periodic orbit theory of deterministic diffusion, introduced in refs. [14, 54, 55], no correlations are neglected - they are all included in the exact cycle expansions for transport coefficients such as the diffusion constant.

Let $\hat{x}(t) = \hat{\phi}^t(\hat{x}_0)$ denote the point in the full state space \widehat{M} reached by the flow in time t . The diffusion tensor is the temporal and ensemble average of the displacement:

$$D_{ij} = \lim_{t \rightarrow \infty} \frac{1}{2dt} \langle \hat{x}(t)_i \hat{x}(t)_j \rangle, \quad (8)$$

where the index i and j are restricted to the spatial components q_i of the state space vectors $x = (q, p)$, i.e., if the dynamics is Hamiltonian, the sum is over the d degrees of freedom.

The Lorentz gas [140] is one of the simplest dynamical systems that exhibit deterministic diffusion. The 2-dimensional Lorentz gas is an infinite scatterer array in which diffusion of a light molecule in a gas of heavy scatterers is modeled by the motion of a point particle in a plane as a sequence of straight, free flight segments, bouncing elastically off an array of reflecting disks. The Lorentz gas is called “gas” because one can equivalently think of it as consisting of any number of point-like fast “light molecules” interacting only with the stationary “heavy molecules,” and not among themselves. As the scatterer array is built up from defocusing surfaces, it is one of the simplest hyperbolic Hamiltonian dynamical systems that exhibits chaos and deterministic diffusion, Figure 34. The original Lorentz gas [140] assumed a random distribution of heavy scatterers; a description of such gas requires statistical assumptions about the distribution of scatterers. A periodic Lorentz gas (configuration of scatterers invariant under a discrete group of translations of the plane), however, is amenable to pure deterministic description. Ergodic properties of periodic Lorentz gases were first studied by Sinai [197], and its diffusive properties have been extensively studied ever since [76, 35, 36, 141, 34, 81, 37]. For a recent review

see Detmantmann [59].

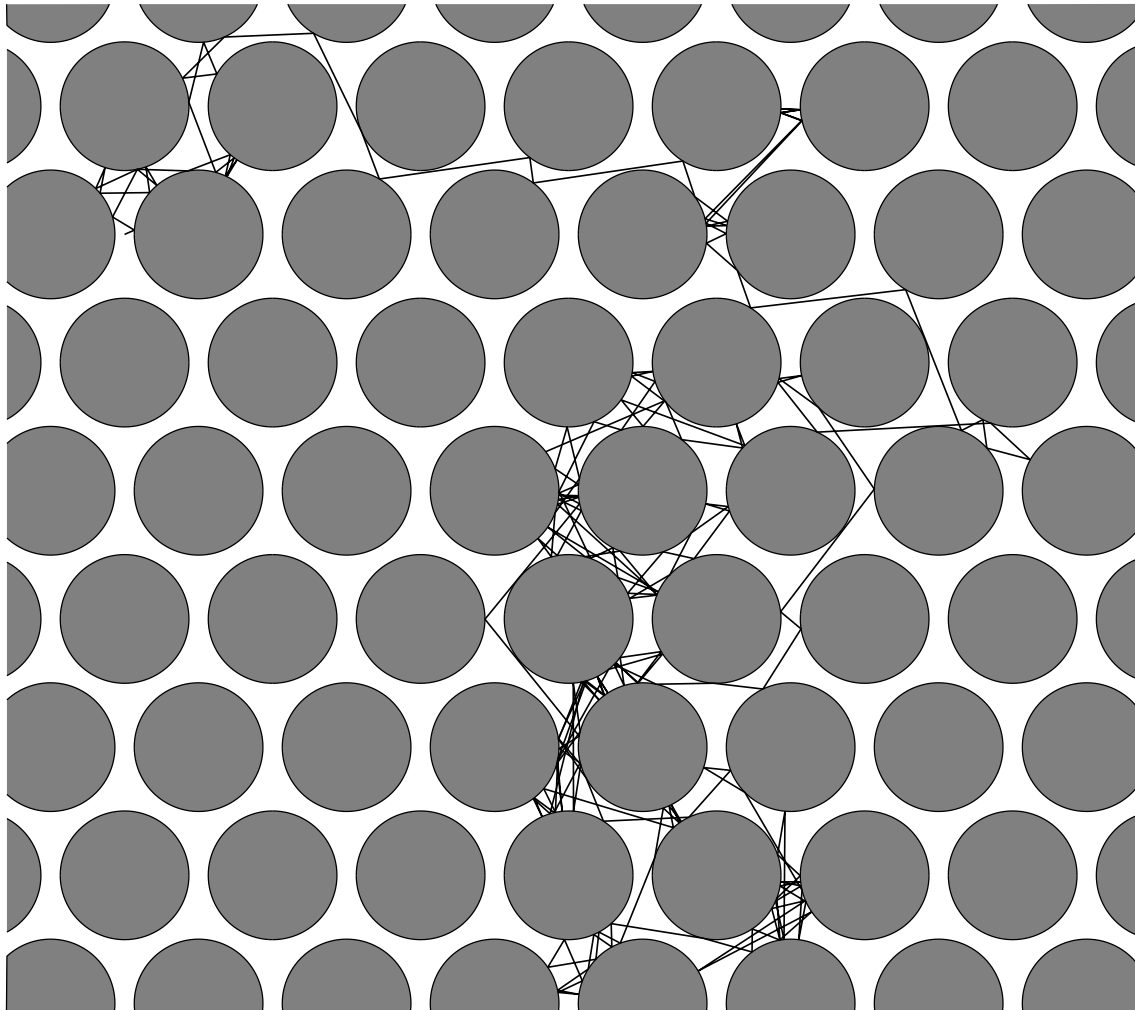


Figure 34: A chaotic trajectory of a finite horizon Lorentz gas point particle bouncing in a hexagonal array of disks. The disks are spaced closely enough so that the no free flight segment is of infinite length.

One distinguishes the *infinite horizon* diffusive behavior, which allows for infinite length flights, from the *finite horizon* case [36], where the particle always hits the next disk in finite time. Here we shall restrict our consideration to the finite horizon case, with a triangular tiling of the plane by disks sufficiently large so that no infinite length free flight is possible. In this case the diffusion is normal [36, 27], with $\hat{x}(t)^2$ growing like t . Unfortunately, as we shall see, the same mechanism that guarantees

a finite horizon also leads to rather awkward pruning of periodic orbits.

The approach introduced in ref. [54] and tested in ref. [55], exploits the fact that the periodic Lorentz gas can be constructed by putting together translated copies of an elementary cell. Therefore quantities characterizing global dynamics, such as the Lyapunov exponent and the diffusion constant, can be computed from the dynamics restricted to the elementary cell.

To investigate the transport property of such systems, we apply cycle expansions [52] to the analysis of *diffusion coefficient*. The resulting formulas are exact; no probabilistic assumptions are made, and all correlations are taken into account by the inclusion of cycles of all periods. While existing cycle expansion theory yields the correct result by tiling the state space into elementary cells, the convergence rate is slow because of bad shadowing and poor choice of symbolic grammar [55]. In this paper we propose a novel approach that significantly improves the efficiency of cycle expansion formula, by factorizing the non-commuting rotational and translational symmetry and using periodic orbits in the fundamental domain.

The exact results are sometimes counterintuitive, and might help us decide whether a diffusive phenomenon whose microscopic dynamics is hard to observe directly, such as conductance fluctuations in a mesoscopic device, is due to impurities or to deterministic transport. For example, as some parameter (such as mean free flight time) is increased, the deterministic diffusion coefficient reveals a non-monotone, fractal dependence.

In sect. 4.2 we define periodic Lorentz gas, and describe the symmetry reduction of its full state space to the elementary cell and the fundamental domain.

In sect. 4.5 we briefly review the formulas for diffusion coefficients in the 2-dimensional periodic Lorentz gas, using dynamics restricted in elementary cell.

In sect. 4.6 we factorize the rotational symmetry and derive the diffusion coefficient

using fundamental domain cycles.

4.2 Diffusion in periodic arrays

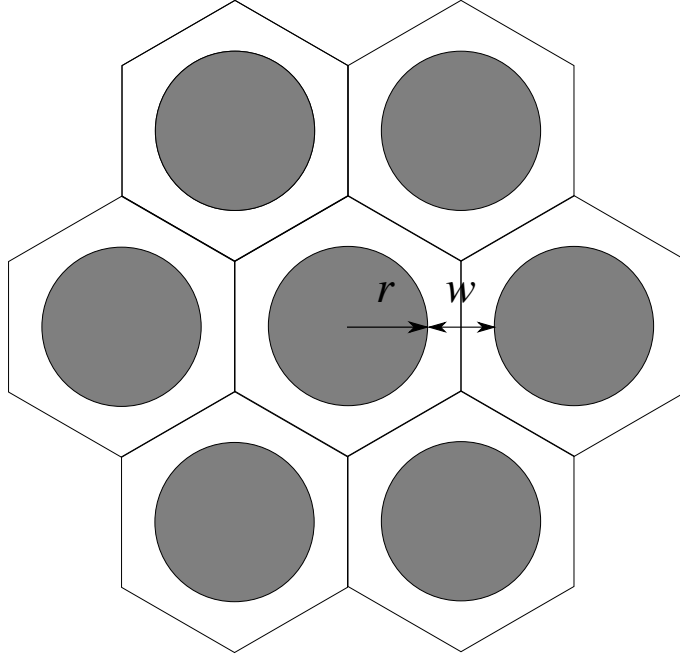


Figure 35: An elementary cell and its six unit translations. The ratio of distance w between the nearest pair of disks to the disk radius r determines the dynamical properties in the system. The transition between the finite and the infinite horizon is controlled by the ratio of w/r : the horizon is finite for $w/r < 4/\sqrt{3} - 2 = 0.3094 \dots$.

Most of the periodic Lorentz gas literature, such as Bunimovich and Sinai [36], is focused on the symmetries under discrete translations of periodic tilings of the plane, usually defined by a parallelepipedal “fundamental domain” (“primitive unit cell”) spanned by a pair of vectors $\mathbf{e}_1, \mathbf{e}_2$, such that the center of every disk is labeled by a pair of integers $\hat{n} = (m, n) = m \mathbf{e}_1 + n \mathbf{e}_2$. However, for a triangular periodic Lorentz gas the full symmetry group is the space group $p6mm$ (see Cotton [46] *Chemical applications of group theory*, Chapt. 11, for a discussion of the geometry of space groups), and the natural tiling is in terms of the hexagon centered on the scattering disk (“Wigner-Seitz cell”, “Voronoi cell”), see Figure 35. The full, infinite state space

\widehat{M} (i.e., both spatial coordinates and momenta) then has a periodic tiling by compact state space tiles

$$\widehat{M} = \bigcup_{\hat{n} \in T} \mathcal{M}_{\hat{n}},$$

obtained by all *translations* a state space tile, which we here refer to as the *elementary cell* $\mathcal{M} = \mathcal{M}_0$, with T the abelian group of lattice translations.

Furthermore, space group $p6mm$ has a point subgroup $C_{6v} = D_6$, because the hexagonal elementary cell itself can be tiled by 12 triangular tiles,

$$\mathcal{M} = \bigcup_{g \in D_6} \widetilde{M}_g,$$

as in Figure 36 (a), upper left. We pick one of these compact state spaces, and refer to it as the *fundamental domain* $\widetilde{M} = \widetilde{M}_e$. The fundamental domain tiles the full hexagon by its 11 copies obtained by application of the D_6 point group actions, rotations around the center or reflections across symmetry lines.

As we will work with three kinds of state spaces, throughout the text we will repeatedly use tildes (\sim), nothings and hats ($\widehat{}$) atop symbols to signify dynamical quantities in the fundamental domain, elementary cell and full state space, respectively:

$$\begin{array}{ll} \sim & \text{fundamental domain } \widetilde{M}, \text{ triangle in Figure 36} \\ [\textit{nothing}] & \text{elementary cell } \mathcal{M}, \text{ hexagon in Figure 36} \\ \widehat{} & \text{full state space } \widehat{M}, \text{ lattice in Figure 36} \end{array} \quad (9)$$

The dynamics can be restricted to the elementary cell by imposing periodic boundary conditions: whenever the particle leaves across the edge of the hexagon cell, it immediately reenters through the opposite edge, and the corresponding discrete translation is recorded, in order that the full state space trajectory can be reconstructed from the trajectory confined to the elementary cell. Let $\hat{x}(t) = \hat{\phi}^t(\hat{x}_0)$ denote the point in the full state space \widehat{M} reached by the flow in time t . $x(t) = \phi^t(x_0)$ denotes the

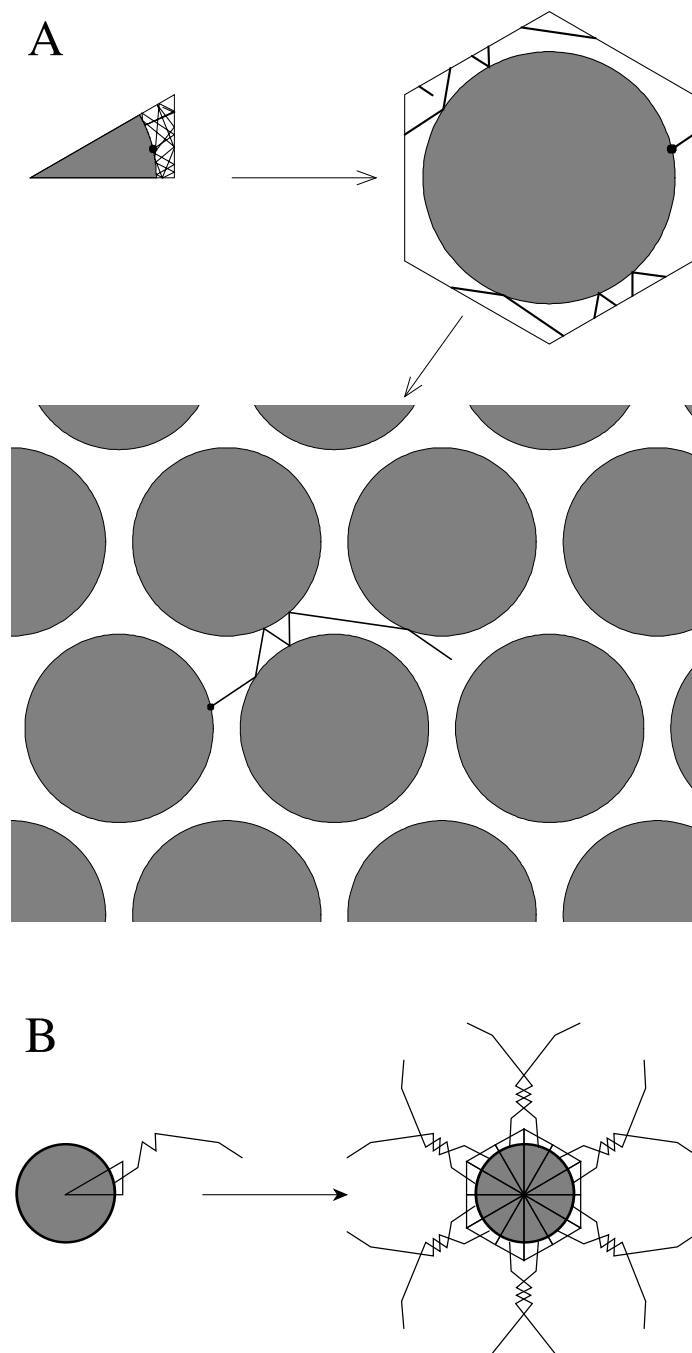


Figure 36: (A) Motion in the fundamental domain $\widetilde{\mathcal{M}}$ (top left), the elementary cell \mathcal{M} (top right), and the full state space $\widehat{\mathcal{M}}$ (bottom). (B) The above trajectory unwrapped in the full space and its 11 copies obtained by applying all D_6 point group actions to it. Figure adapted from ref. [55].

corresponding flow in the elementary cell; the two are related by

$$\hat{n}_t(x_0) = \hat{\phi}^t(x_0) - \phi^t(x_0) \in T, \quad (10)$$

the translation of the endpoint of the global path into the elementary cell \mathcal{M} . We will show in sect. 4.5 that for the dynamics in the elementary cell, the full state space displacement accrued along an elementary cell periodic orbit is one-to-one and independent of the starting point.

The elementary cell dynamics can be restricted to dynamics in the fundamental domain by applying a reflection whenever the trajectory crosses one of the three edges of the triangle, as will be discussed in detail in sect. 4.4.1. We denote the quantity $\tilde{x}(t) = \tilde{\phi}^t(\tilde{x})$ as the flow in the fundamental domain \widetilde{M} . $\tilde{\phi}^t(\tilde{x})$ is related to $\phi^t(\tilde{x})$ by a point group symmetry $g \in D_6$ which maps $\tilde{x}(t) \in \widetilde{M}$ to $x(t) \in \mathcal{M}$.

Thus any full state space trajectory $\hat{x}(t)$ can be uniquely reduced to its fundamental domain counterpart $\tilde{x}(t)$. This eliminates redundancies purely due to symmetries, and renders computations carried out in the fundamental domain easier, with significantly faster convergence. The reverse process, however, is always one-to-many, as illustrated by Figure 36 (b). As the fundamental domain does not have the concept of absolute orientation, a single unwrapped trajectory may have up to 11 full state space copies, with 12 orientations in all. Even worse, depending on where we start to unwrap the trajectory, the full state space trajectories can be of completely different shapes, and, the global distance $\hat{f}^{rT_{\tilde{p}}}(\tilde{x}) - \tilde{x}$, $\tilde{x} \in \tilde{p}$, depends on the starting cycle point if \tilde{p} is only a segment of the global cycle p . An example is the full state space diamond-shaped 4-cycle of Figure 37; depending whether one starts at \tilde{x}_1 or \tilde{x}_2 on the corresponding fundamental domain 2-cycle, the global distance covered in time $T_{\tilde{p}}$ is either the short or the long diagonal.

How to deal with such consequences of the non-commutativity of translations and rotations is the main thrust of this paper.

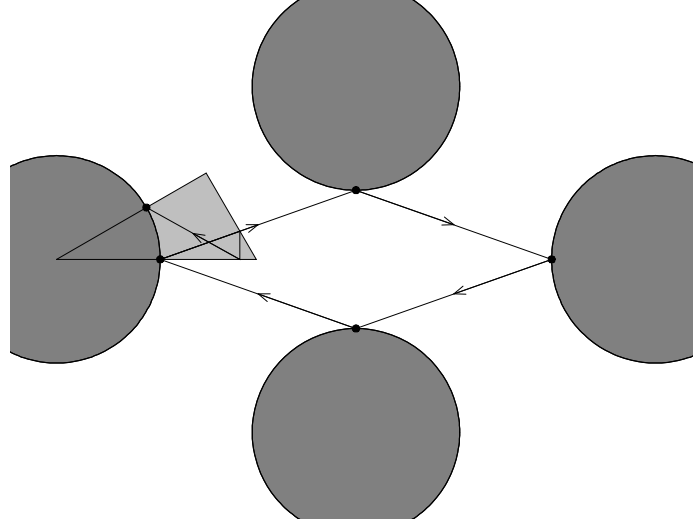


Figure 37: A fundamental domain periodic orbit unwrapped in full space. Figure reproduced from ref. [54].

4.3 Elementary cell symbolic dynamics

The computation of diffusion coefficient (39) requires knowledge of periodic orbits. In the Lorentz gas system, a few simple orbits may be obtained by inspection: a 2-bounce periodic orbit is traced out by the particle bouncing between a disk and one of its nearest neighbors, or one of the second nearest disks. The number of periodic orbits increases exponentially with n_p , the number of bounces (the ‘topological length’ of the orbit), they trace out shapes of increasing spatial complexity, and as their instability increases exponentially with their length, it becomes quickly not possible to determine them with the initial guess Newton’s method.

Instead, we need to first enumerate qualitatively all possible trajectories, i.e., construct the *symbolic dynamics* for the system. The idea is to identify each periodic orbit with a unique sequence of symbols, drawn from a finite alphabet. Intuitively speaking, a symbol may characterize a certain pattern of the dynamics. Once the alphabet and the grammar of admissible itineraries is determined, we may enumerate all possible periodic orbits and eventually pin down as many as needed for the

computation of a given long-time average.

We start with a brief review of the symbolic dynamics developed in ref. [55]. With imposed finite horizon there are 12 possible ways of jump from a disk (Figure 38 (a)). Any trajectory in the full space can always be constructed from a series of flights, each belongs to the 12 “signature jumps”. In particular, a periodic orbit in the elementary cell is represented as a repeatable string of such symbols. For example, the bouncing mode between nearest disks is written as $\overline{06}$, meaning that the periodic orbit is consisted of two successive flights, one traveling towards right (symbol 0) and the next reflecting backwards (symbol 6).

Periodic orbits in the elementary cell can either be *stationary* in the full state space (returning to its initial point after completing a full cycle, e.g., $\overline{06}$ that bounces between two nearest disks); or *running*, with a net spatial displacement after each period (e.g., $\overline{05}$, Figure 38 (a) and (c)). A stationary cycle “traps” the particle locally for all time, while a running cycle advances it at a constant velocity. The diffusion (39) is the result of competition between the two type of cycles.

With the symbolic dynamics, we then use the least action principle to compute the periodic orbits [52]. In a planetary Hamiltonian billiard system, the Maupertuis’ principle indicates that the traveling length along a cycle is minimized. We can solve the problem by optimizing the total free flight distance with the constraint that links have to connect the specific disks visited along the orbit.

Some confidence can be gained at this point by applying the above formula (39) to a trivial system. For a simple example, see the chain of baker’s maps chain of coupled baker maps studied in ref. [79]. In this case there are only four fixed points, all with stability $\Lambda_p = 1/2$, two of which give rise to the translations $\hat{n}_p = \pm 1$. As the system is uniformly hyperbolic, all curvature terms are identically zero, and the fixed points substituted into (39) yield immediately the correct result $D = 1/4$.

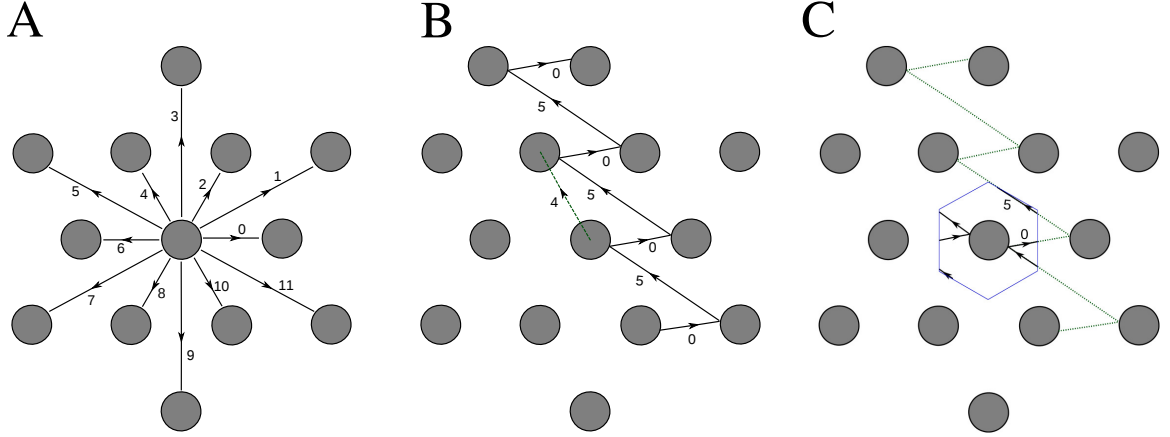


Figure 38: Elementary cell symbolic dynamics is obtained by counterclockwise labeling the translation vectors connecting the center of the current disk to the center of the next disk. (A) The finite horizon is here imposed by limiting jumps from the center cell to six short jumps (even labels $0, 2, \dots, 10$) and six ‘long’ jumps (odd labels $1, 3, \dots, 11$). (B) Running mode $\overline{05}$ advances by \hat{n}_4 per period. (C) In the elementary cell this is a periodic orbit $\overline{05}$ of topological length 2.

4.4 Into the fundamental domain

In ref. [54] some effort, unsuccessful, was made to derive a diffusion formula for the fully symmetry-reduced dynamics, involving only quantities computed within the fundamental domain. The fact that lattice translations do not commute with the symmetry group within the elementary cell makes this apparently a difficult task. The main achievement of this paper is a new proposal how to extend periodic orbit theory in order to solve this vexing problem.

In sect. 4.2 we had reduced a trajectory from full space to elementary cell, as in Figure 36(a), upper right, using the translational symmetry, and were able to compute various quantities in terms of elementary cell periodic orbits. In this section we will further utilize the point group symmetry to derive the fully symmetry-reduced trace formula and, for the first time, the diffusion constant using cycles restricted to the fundamental domain.

4.4.1 Point group changes translation

A point x in the elementary cell is identified by its fundamental domain mirror image:

$$x = g \tilde{x},$$

given a little group action $g \in G$. We have to appreciate that both the full space flow $\hat{\phi}^t(x)$ and elementary flow $\phi^t(x)$ is G-equivariant under the lattice group symmetry,

$$\hat{\phi}^t(g \tilde{x}) = g \hat{\phi}^t(\tilde{x}), \phi^t(g \tilde{x}) = g \phi^t(\tilde{x}), \quad (11)$$

It follows that the displacement in full space is also G-equivariant under the little group:

$$\hat{n}_t(x) = \hat{\phi}^t(g \tilde{x}) - \phi^t(g \tilde{x}) = g (\hat{\phi}^t(\tilde{x}) - \phi^t(\tilde{x})) = g \hat{n}_t(\tilde{x}). \quad (12)$$

However, this nice property does not automatically resolve the problem at hand. When the dynamics is restricted to the fundamental domain, we lose the absolute orientation. We show this by following a prime periodic orbit \tilde{p} in the fundamental domain.

Let $\tilde{p} \equiv \{\tilde{x}_1, \dots, \tilde{x}_{n_{\tilde{p}}}\}$, with topological length $n_{\tilde{p}}$ and \tilde{x}_i the points of collision on the orbit. Starting from the edge of disk at \tilde{x}_i , at some point the flight will meet one of the triangle boundaries of the fundamental domain and be deflected back. In the full space the particle continues to another triangular domain, which, in general, does not have the same orientation to the original copy (figure here). The relative change in the orientation can always be described by a element of the little group. Before the particle reaches the next collision point \tilde{x}_{i+1} , it has crossed multiple boundaries (or symmetry lines), and we denote the accumulated change in the orientation by $g_{\tilde{p}}(\tilde{x}_i, \tilde{x}_{i+1})$.

Denote the displacement of flight $(\tilde{x}_i, \tilde{x}_{i+1})$ as $\hat{n}_{\tilde{p}}(\tilde{x}_i, \tilde{x}_{i+1})$, the added displacement from \tilde{x}_i to \tilde{x}_{i+2} is

$$\hat{n}_{\tilde{p}}(\tilde{x}_i, \tilde{x}_{i+2}) = \hat{n}_{\tilde{p}}(\tilde{x}_i, \tilde{x}_{i+1}) + g_{\tilde{p}}(\tilde{x}_i, \tilde{x}_{i+1}) \hat{n}_{\tilde{p}}(\tilde{x}_{i+1}, \tilde{x}_{i+2}), \quad (13)$$

i.e., we have to memorize the change in the relative orientation. Applying this rule to the entire cycle, we have (after applying a cyclic shift $n_{\tilde{p}} + 1 \rightarrow 1$)

$$\hat{n}_{\tilde{p}}(\tilde{x}_1) = \sum_{i=1}^{n_{\tilde{p}}} g_{\tilde{p}}(\tilde{x}_1, \tilde{x}_i) \hat{n}(\tilde{x}_i, \tilde{x}_{i+1}), \quad (14)$$

where the left order product $g_{\tilde{p}}(\tilde{x}_1, \tilde{x}_i) = \prod_{j=1}^{i-1} g_{\tilde{p}}(\tilde{x}_j, \tilde{x}_{j+1})$, and $g_{\tilde{p}}(\tilde{x}_1, \tilde{x}_1) = e$. Unlike in the elementary cell, the displacement in general is dependent on the starting point.

We define the total group action (orientation change) for the orbit

$$h_{\tilde{p}}(\tilde{x}_1) = \prod_{i=1}^{n_{\tilde{p}}} g_{\tilde{p}}(\tilde{x}_i, \tilde{x}_{i+1}), \quad (15)$$

which immediately connects the flow in fundamental domain and elementary cell by

$$\phi^{t_{\tilde{p}}}(\tilde{x}_i) = h_{\tilde{p}}(\tilde{x}_i) \tilde{\phi}^{t_{\tilde{p}}}(\tilde{x}_i). \quad (16)$$

Although the group action $h_{\tilde{p}}(\tilde{x}_i)$ depends on the initial points on the orbit as well, it is a property of the orbit's symmetry. Using (15), one can easily show that all $h_{\tilde{p}}(\tilde{x}_i)$, $\tilde{x}_i \in \tilde{p}$ belong to the *same* subgroup of G

$$h_{\tilde{p}}(\tilde{x}_{i+1}) = g_{\tilde{p}}^{-1}(\tilde{x}_i, \tilde{x}_{i+1}) h_{\tilde{p}}(\tilde{x}_i) g_{\tilde{p}}(\tilde{x}_i, \tilde{x}_{i+1}). \quad (17)$$

If we let the particle (starting from \tilde{x}_i) travel along the fundamental domain orbit r times, the result displacement is

$$\hat{L}_{\tilde{p}}(r, \tilde{x}_i) \equiv (e + h_{\tilde{p}}^1(\tilde{x}_i) + \dots + h_{\tilde{p}}^{r-1}(\tilde{x}_i)) \cdot \hat{n}_{\tilde{p}}(\tilde{x}_i). \quad (18)$$

4.4.2 Grammar of fundamental domain

Existing elementary cell symbolic dynamics cannot generate the prime fundamental domain orbits. While the 12 symbols partition the elementary cell state space into distinct regions, when wrapped into the fundamental domain state space, these regions begin to overlap. Thus, we developed a new symbolic description to identify the fundamental domain cycles, by means of tile generators, which we describe next.

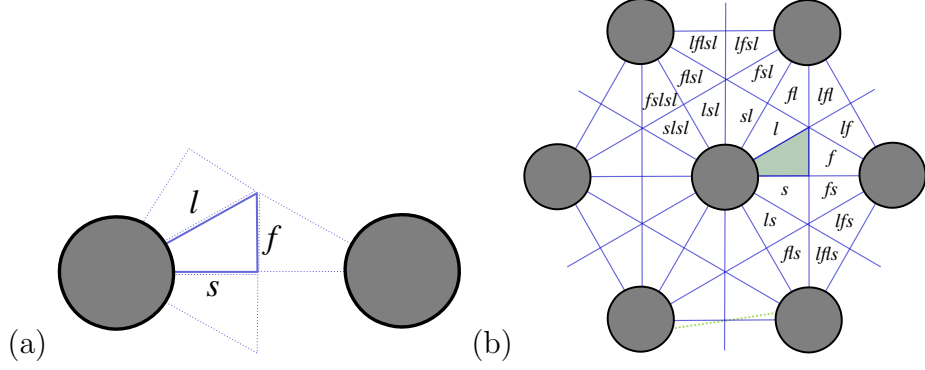


Figure 39: (a) Three generators tile the plane by flipping the fundamental domain across its three straight edges. Two are elements of D_6 , the reflection s across the short disk-disk separation, and the reflection ℓ across the long disk-disk separation. Together they tile the elementary cell (hexagon in Figure 36 (a) upper right) by copies of the fundamental domain. Translations are generated by the reflection f that pivots a disk center to disk center by a flip across the symmetry line normal to the short disk-disk separation. (b) Tiling of the 7-disk by copies of the fundamental domain, labeled by a (not unique) sequence of the three generators $\{s, \ell, f\}$, chosen so that each sequence contain one and only on disk-to-disk pivot f .

Tracking an arbitrary trajectory in the triangular, fundamental domain, we can distinguish two types of bounces: those off the disk edge, and those that in the full state space cross the symmetry axes. As discussed in sect. 4.4.1, the latter will add up to group operations along the full state space trajectory.

We enumerate all the elements in the point group D_6 :

$$G = \{e, C_6^+, C_6^-, C_3^+, C_3^-, C_2, \sigma_{d1}, \sigma_{d2}, \sigma_{d3}, \sigma_{v1}, \sigma_{v2}, \sigma_{v3}\}, \quad (19)$$

with $s = \sigma_d$ the reflection across the short disk-disk separation, and $\ell = \sigma_v$ reflection across the long disk-disk separation generators of D_6 . The entire space group $p6mm$ is then generated by adding a disk-to-disk generator f that pivots a disk center to another by flip across the symmetry line normal to the short disk-disk separation, Figure 39 (a). We find it convenient to define C as the generator of cyclic rotations by $\pi/3$,

$$\ell s = C_6^- = C, \quad C^6 = e; \quad s\ell = C_6^+, \quad s = C_6^+ \ell. \quad (20)$$

A free flight between two disks in the full space may then be wrapped into fundamental domain, according to the sequence of edges $\{s, \ell, f\}$ it passed. There are many different paths when jump to the nearest disk: it can be as simple as a single pivot f , or can be more complex such like ℓfs that involves crossing multiple symmetry lines, Figure 39 (b). We also note that some symbol combinations are topologically equivalent, in the sense that they yield the same group actions. For example, the short jump sf is topologically equivalent to fs , because the particle ends up in the same copy of fundamental domain before the next collision.

Our next task is to generate all topologically distinct itineraries from $\{s, \ell, f\}$. We can immediately realize a partial list of the equivalence relations:

$$\begin{aligned} fs &= sf, \\ flf &= lfl. \end{aligned} \tag{21}$$

All longer equivalence relations in Figure 39 can be reduced to the above primitive ones:

$$\begin{aligned} fsl &= sfl, \\ lf ls &= flsf. \end{aligned} \tag{22}$$

There are also some pruning rules to keep in mind. Because a free flight cannot cross the same border twice, sequences including $\ell\ell, ff, ss$ are forbidden. C^3 (and all higher orders) is also pruned as the particle cannot cross the center hard disk; nor swirl around it.

While the string description of flight is mathematically rigorous, it is practically impossible to be encoded into programs for computing the orbits, because the number of equivalent strings increases exponentially when the length of the orbit (and also the string) increases. However, there is a more physically intuitive way to organize the symbols, by means of “topological flight”, Figure 40 (a). In this representation, a

equivalence relation like $sf \equiv fs$ can be uniquely identified by a combination of a disk number and a partition number $\{\bar{0}, \underline{6}\}$. Longer flight such like $lflslf \equiv flfslf \equiv flsflf \equiv flslfl$ that cross many boundaries now yields a very simple symbol pair $\{\bar{1}, \underline{5}\}$.

Because this compact representation only takes into consideration the starting and ending points of a free flight, the exponentially long list of equivalent strings are eliminated. The topological flight leads to a straight forward numerical scheme to find cycles. The disk number fixes the two ends of the free flight while the partition number limits the range of angles on the disk. Similar to searching cycles in the elementary cell, we now have a constrained version of convex minimization problem which can be solved using standard non-linear optimization approach.

4.5 Periodic orbit theory

Periodic orbit theory of deterministic diffusion, introduced in refs. [14, 54], exploits the fact that the periodic Lorentz gas can be constructed by putting together translated copies of an elementary cell. Therefore quantities characterizing global dynamics, such as the Lyapunov exponents and the diffusion tensor, can be computed from the dynamics restricted to the elementary cell, as shown numerically in ref. [55]. In refs. [14, 54, 55, 15, 16] it was shown that deterministic diffusion tensor in the *periodic* Lorentz gas can be expressed in terms of (relative) periodic orbits, and exact formulae for such global dynamical averages as Lyapunov exponent and diffusion tensor were derived, using only the dynamics in the *elementary cell*, which we discuss now.

Previous works by Machta and Zwanzig [141] have given numerical results for the diffusion constant in Lorentz gases, as well as estimates based on a random walk approximation. We shall follow their notation and fix the radius of the disks to 1, and assume unit particle speed.

Let $\hat{x}(t) = \hat{\phi}^t(\hat{x}_0)$ denotes the point in the full space \widehat{M} reached by the flow in

time t . $x(t) = \phi^t(x_0)$ denotes the corresponding flow in the elementary cell; the two are related by

$$\hat{n}_t(x_0) = \hat{\phi}^t(x_0) - \phi^t(x_0) \in T, \quad (23)$$

the translation of the endpoint of the global path into the elementary cell \mathcal{M} . The diffusion tensor, by definition, is the temporal and ensemble average of the displacement:

$$D_{ij} = \lim_{t \rightarrow \infty} \frac{1}{2dt} \langle \hat{n}_t(x_0)_i \hat{n}_t(x_0)_j \rangle_{\widehat{\mathcal{M}}}, \quad (24)$$

where the index i and j are restricted to spatial components q_i of the state space vectors $x = (q, p)$, i.e., if the dynamics is Hamiltonian, the sum is over the d degrees of freedom.

Following the general definition (24), one can numerically compute the diffusion coefficient for various systems (which is not limited to the Lorentz gas). However, little insight is gained in the dynamics of the system. Instead, [14, 54, 55, 15, 16] suggest we study the quantity

$$Q(\beta) = \lim_{t \rightarrow \infty} \frac{1}{t} \log \langle e^{\beta \cdot \hat{n}_t(x)} \rangle_{\widehat{\mathcal{M}}}, \quad (25)$$

where β is an auxiliary vector quantity. The interesting dynamical averages such like mean drift and diffusion can be easily obtained by taking derivatives of $Q(\beta)$ and set $\beta = 0$, e.g.:

$$\begin{aligned} 2dD_{ij} &= \left. \frac{\partial}{\partial \beta_i} \frac{\partial}{\partial \beta_j} Q(\beta) \right|_{\beta=0} \\ &= \lim_{t \rightarrow \infty} \frac{1}{t} \langle \hat{n}_t(x)_i \hat{n}_t(x)_j \rangle_{\widehat{\mathcal{M}}}, \end{aligned} \quad (26)$$

yields a diffusion matrix. The diffusion tensor matrix can, in general, be anisotropic (i.e., have d distinct eigenvalues and eigenvectors). The spatial diffusion constant is then given by the Einstein relation

$$D = \frac{1}{2d} \sum_i^d \left. \frac{\partial^2}{\partial \beta_i^2} Q(\beta) \right|_{\beta=0} = \lim_{t \rightarrow \infty} \frac{1}{2dt} \langle (\hat{q}(t) - q)^2 \rangle_{\widehat{\mathcal{M}}}, \quad (27)$$

Because of the translational invariance, it was shown in ref. [55] that the ensemble average in (25) can be written as an integral over the elementary cell

$$\langle e^{\beta \cdot (\hat{x}(t) - x)} \rangle = \frac{1}{|\mathcal{M}|} \int_{x,y \in \mathcal{M}} dx dy \mathcal{L}^t(y, x), \quad (28)$$

given the evolution operator

$$\mathcal{L}^t(y, x) = e^{\beta \cdot (\hat{x}(t) - x)} \delta(y - x(t)), \quad (29)$$

for the flow. It is a linear operator such that it satisfies the semi-group property:

$$\mathcal{L}^{t_1+t_2}(y, x) = \int dx' \mathcal{L}^{t_2}(y, x') \mathcal{L}^{t_1}(x', x) \quad (30)$$

and when $\beta = 0$ it reduces to the Ruelle-Perron-Frobenius operator.

We may also introduce the same operator for discrete maps, after we have chosen the appropriate Poincaré section and study the dynamics restricted to the intersections of the flow on the hyper-surface:

$$\mathcal{L}^n(y, x) = e^{\beta \cdot (\hat{f}^n(x) - x)} \delta(y - f^n(x)). \quad (31)$$

For the Lorentz gas system, consider the Poincaré section to be the edge of the disk. The finite horizon guarantees that the particle will collide with a disk in finite time and the Poincaré map is truly a “return map”. Once we have specified the arch length φ at which the particle hits the disk and the incident angle ψ (which gives the tangent velocity component at the collision point), the dynamics is fully determined. There are two other marginal directions along which the dynamics is trivial, because the system is Hamiltonian.

The dynamical average we are interested does not belong to any particular finite time (or a finite number of returns on the section). As $t \rightarrow \infty$ (or $n \rightarrow \infty$ for the map), the average quantities are dominated by the leading eigenvalue of \mathcal{L}^t , $\lambda_0 = e^{s(\beta)t}$, i.e., it is straightforward to show that in the limit $Q(\beta) \rightarrow s(\beta)$.

For sake of simplicity, we will proceed with the derivation for the return map and in the end generalize to the continuous flow. While the evolution operator (29) and (31) act on a functional space of infinite dimension, their spectrum may still be extracted by the trace formula:

$$\det(1 - z\mathcal{L}) = \exp\left(-\sum_{n=0}^{\infty} \frac{z^n}{n} \text{tr} \mathcal{L}^n\right), \quad (32)$$

where z is an auxiliary variable, and the trace:

$$\text{tr} \mathcal{L}^n = \int_{\mathcal{M}} dx e^{\beta \cdot (\hat{f}^n(x) - x)} \delta(x - f^n(x)). \quad (33)$$

With the δ function inside, eq. (33) picks up a contribution whenever $x = f^n(x)$, e.g. when x is a periodic point of the map f . When n is not a prime number, it is possible that x belongs to a periodic orbit p of period n_p , and satisfies the multiplicity $n_p r = n$, where r is the number of repeats.

We may now restrict the integral only in the vicinities of the prime periodic orbits (i.e., those who are not the repeat of other periodic orbits) of the return map, and write:

$$\text{tr} \mathcal{L}^n = \sum_p \delta_{n, n_p r} \sum_{x \in p} \frac{e^{r\beta \cdot \hat{n}_p(x)}}{|\det(\mathbf{1} - \mathbf{J}_p^r(x))|}, \quad (34)$$

where $\mathbf{J}_p(x) = Df^{n_p}(x)$ is the Jacobian. Using the chain rule of differentiation, it follows that $\mathbf{J}_p(x) = \mathbf{J}_p$, i.e., the Jacobian is independent of the point x on the cycle. We can also show that $\hat{n}_p(x) = \hat{n}_p$, by summing all the free flights along the cycle: because translations are commutative, the order at which individual displacements are added stays irrelevant.

With (35) and (33), we finally obtain:

$$\det(1 - z\mathcal{L}) = \prod_p \exp\left(-\sum_{r=1}^{\infty} \frac{z^{n_p r}}{r} \frac{e^{r\beta \cdot \hat{n}_p}}{|\det(\mathbf{1} - \mathbf{J}_p^r)|}\right), \quad (35)$$

where the product runs over all prime periodic cycles in the elementary cell.

Generalization to continuous time [29, 53] amounts to the replacement $z^{n_p} \rightarrow e^{-sT_p}$, where T_p is now the (not necessarily integer) period of the prime cycle p for the

flow. One has to distinguish the period of the return map, n_p , which is the number of collisions for the cycle, and the period of the flow, T_p , which represents the time traveled after finishing the cycle once. The spectrum determinant for the continuous time is:

$$Z(\beta, s) = \prod_{p \in \mathbf{P}} \exp \left(- \sum_{r=1}^{\infty} \frac{1}{r} \frac{e^{(\beta \cdot \hat{n}_p - s T_p)r}}{|\det(\mathbf{1} - \mathbf{J}_p^r)|} \right), \quad (36)$$

and the associated dynamical zeta function:

$$1/\zeta(\beta, s) = \prod_p \left(1 - \frac{e^{(\beta \cdot \hat{n}_p - s T_p)}}{|\Lambda_p|} \right), \quad (37)$$

when one approximates the $\det(\mathbf{1} - \mathbf{J}_p^r)$ with the product of expanding eigenvalues of the cycle, Λ_p .

The determinant (36) has many resonances (zeros) on the complex s plane, even for the simplest systems. According to previous literatures [52], extracting the leading eigenvalue of the evolution operator amounts to solve the implicit equation $Z(\beta, s(\beta)) = 0$. By taking derivatives with respect to β we arrive at

$$\frac{ds}{d\beta} = - \frac{\partial Z}{\partial \beta} / \frac{\partial Z}{\partial s}. \quad (38)$$

The final piece needed now is to determine the actual value $s(\beta)$ at $\beta = 0$. The Lorentz gas system is infinite and yet *bounded* such that the particle can never exist the lattice. In other words, the flow is *conserved*, and the escape rate $s(\beta = 0) = 0$. The problem at hand is automatically resolved, and also provides us a sanity check $Z(0, 0) \approx 0$, if the cycle expansion formula is correct and all cycles are included.

The dynamical zeta function cycle averaging formula for the diffusion constant, zero mean drift $\langle \hat{x}_i \rangle = 0$ (because the system is symmetric), is given by

$$D = \frac{1}{2d} \frac{\langle \hat{x}^2 \rangle_{\zeta}}{\langle T \rangle_{\zeta}} = \frac{1}{2d} \frac{1}{\langle T \rangle_{\zeta}} \sum' \frac{(-1)^{k+1} (\hat{n}_{p_1} + \dots + \hat{n}_{p_k})^2}{|\Lambda_{p_1} \dots \Lambda_{p_k}|}, \quad (39)$$

where $\langle T \rangle_{\zeta} = \partial Z / \partial s|_{s=0}$, and the sum is over all distinct non-repeating combinations of prime cycles. The derivation is standard, still the formula is strange. Diffusion

is unbounded motion across an infinite lattice; nevertheless, the reduction to the elementary cell enables us to compute relevant quantities in the usual way, in terms of periodic orbits.

4.6 Fundamental domain diffusion tensor

If a quantum system has an underlying symmetry, its Hamiltonian can be block-diagonalized by the irreducible representations of the symmetry group, with each block spanned by a set of degenerate states. In fact, this standard approach is not specific to quantum mechanics. Once we describe the classical dynamics in terms of the evolution operator, the algebra follows in a similar way, and the group factorization applies. The quotiented state space, i.e., the fundamental domain, is more compact, as understood by the one-to-many map of periodic orbits. The convergence of cycle expansion formulae improves and less cycles are required. In previous works [55, 52] fundamental domain cycle expansion for scalar quantities such like Lyapunov constant was obtained. However, for reasons mentioned in sect. 4.4.1, an exact formula for the diffusion constant (an average over displacement, a vector quantity) was not given.

We start from the trace of elementary cell evolution operator (33) and project it into the irreducible representations \mathcal{I}_G . We first derive the map version:

$$\begin{aligned} \text{tr } \mathcal{L}^n &= \sum_{\alpha \in \mathcal{I}_G} \text{tr } \mathcal{L}_\alpha^n \\ \text{tr } \mathcal{L}_\alpha^n &= \frac{d_\alpha}{|G|} \sum_{h \in G} \chi_\alpha(h) \\ &\quad \int_{\tilde{\mathcal{M}}} d\tilde{x} \sum_{\sigma \in G} \delta(h^{-1}\tilde{x} - f^n(\sigma\tilde{x})) e^{\beta \cdot (f^n(\sigma\tilde{x}) - \sigma\tilde{x})}, \end{aligned}$$

where d_α is the dimension of irrep α and $\chi_\alpha(h)$ the group character. Using equivariance relations (11), (12), and noting that the little group is closed, we have:

$$\begin{aligned} \text{tr } \mathcal{L}_\alpha^n &= \frac{d_\alpha}{|G|} \sum_{\sigma \in G} \sum_{h \in G} \chi_\alpha(h) \\ &\int_{\tilde{\mathcal{M}}} d\tilde{x} \delta(h^{-1}\tilde{x} - f^n(\tilde{x})) e^{\beta \cdot \sigma \cdot (\hat{f}^n(\tilde{x}) - \tilde{x})}. \end{aligned} \quad (40)$$

As in the analysis of sect. 4.5, the δ -function part $\delta(h^{-1}\tilde{x} - f^n(\tilde{x}))$ in the integral selects points on fundamental domain relative periodic orbits \tilde{p} . In addition, after completing the cycle r times, the cumulative group action should also satisfy $h_{\tilde{p}}^r(\tilde{x}) = h$. It follows that the integral in (40) can be written as a sum over fundamental domain cycles

$$\int_{\tilde{\mathcal{M}}} = \sum_{\tilde{p}} \delta_{n, n_{\tilde{p}} r} \sum_{\tilde{x} \in \tilde{p}} \delta_{h_{\tilde{p}}^r(\tilde{x}), h} \frac{e^{\beta \cdot \sigma \cdot \hat{L}_{\tilde{p}}(r, \tilde{x})}}{|\det(\mathbf{1} - \mathbf{J}_{\tilde{p}}^r(\tilde{x}))|}, \quad (41)$$

where the r -repeats displacement $\hat{L}_{\tilde{p}}(r, \tilde{x})$ along the orbit takes the form computed in (18), and $\mathbf{J}_{\tilde{p}}^r(\tilde{x})$ absorbs the cycle group element $h_{\tilde{p}}^r(\tilde{x})$. The spectral determinant for the α -irrep is:

$$Z_\alpha(\beta, z) = \exp \left(-\frac{d_\alpha}{|G|} \sum_{\sigma \in G} \sum_{\tilde{p}} \frac{1}{n_{\tilde{p}}} \sum_{\tilde{x} \in \tilde{p}} \sum_{r=1}^{\infty} t_{\tilde{p}}(r, \tilde{x}) \right), \quad (42)$$

where

$$t_{\tilde{p}} = \frac{z^{n_{\tilde{p}} r} \chi_\alpha(h_{\tilde{p}}^r(\tilde{x})) e^{\beta \cdot \sigma \cdot \hat{L}_{\tilde{p}}(r, \tilde{x})}}{r |\det(\mathbf{1} - \mathbf{J}_{\tilde{p}}^r(\tilde{x}))|}, \quad (43)$$

is the weight associated with the orbit. The corresponding zeta function ζ_α is obtained by replacing $\det(\mathbf{1} - \mathbf{J}_{\tilde{p}}^r(\tilde{x}))$ with expanding eigenvalues $\Lambda_{\tilde{p}}$. Eq. (42) takes a more complicated form than its counterpart (36) in the elementary cell. As a sanity check, note that if the little group contains only the identity element e , i.e. there is no additional symmetry, it is reduced to (35). Generalization to continuous flow is also different. Besides replacing $z^{n_p} \rightarrow e^{-sT_{\tilde{p}}}$, the summation is changed to an integral

$$\frac{1}{n_{\tilde{p}}} \sum_{\tilde{x} \in \tilde{p}} \rightarrow \frac{1}{T_{\tilde{p}}} \oint_{\mathcal{P}} d\tau \tilde{x}(\tau), \quad (44)$$

which runs along the tangent (marginal) direction of the orbit. Here comes an interesting discovery (to which we return in sect. 4.7): changing the sum to the integral will produce *different* results for any non-trivial symmetry (the group of which contains more than e). For consistency, we denote $\langle \rangle_{\tilde{p}}$ as the average over the cycle \tilde{p} .

The important long term dynamics is contained in the one-dimensional, symmetric representation: $d_\alpha = 1$ and all $\chi(h) = 1$. The cycle averaged mean drift vanishes,

$$\begin{aligned} \langle \hat{x} \rangle_{\zeta_\alpha} &= - \left. \frac{\partial Z_\alpha}{\partial \beta} \right|_{\beta=0, s=0} \\ &= Z_\alpha(0, 0) \sum_{\tilde{p}} \sum_{r=1}^{\infty} \frac{1}{|G|} \sum_{\sigma \in G} \frac{\langle \sigma \cdot \hat{L}_{\tilde{p}}(r, \tilde{x}) \rangle_{\tilde{p}}}{r |\Lambda_{\tilde{p}}|^r} \equiv 0, \end{aligned} \quad (45)$$

because directions of $\sigma \cdot \hat{L}_{\tilde{p}}(r, \tilde{x})$ cancel each other when we sum the group elements σ . Observing that the length $|\sigma \cdot \hat{L}_{\tilde{p}}(r, \tilde{x})|$ does not change under isometric transformations, the cycle averaged mean squared displacement (MSD) is:

$$\langle \hat{x}^2 \rangle_{\zeta_\alpha} = \prod_{\tilde{p}} \left(1 - \frac{1}{|\Lambda_{\tilde{p}}|} \right) \sum_{\tilde{p}} \sum_{r=1}^{\infty} \frac{\langle |\hat{L}_{\tilde{p}}(r, \tilde{x})|^2 \rangle_{\tilde{p}}}{r |\Lambda_{\tilde{p}}|^r}. \quad (46)$$

The formula contains infinite series with exponential tail. In numerical computations we keep the auxiliary variable z in (42), expand (46) as a polynomial and then truncate it according to the topological length of the longest periodic orbit found [52].

There is one last piece before we apply (46) to numerically compute the diffusion coefficients of the Lorentz gas system. There generally exist the “boundary cycles” which completely lie on the symmetry lines. An example of such cycles in the Lorentz gas is $\overline{06}$ (in elementary cell). Boundary cycles remain unchanged when we apply the group action that reflects about the symmetry line, thus simultaneously contribute to multiple terms in (41) (Remember, we absorbed the group element into the Jacobian). Because under axial reflection the eigen-values does not flip sign (see the Jacobian matrix for in chapter 9 of ref. [52]), in our system the boundary orbits contribute

normally and does not need special treatment (see formulations in chapter 25 of ref. [52]).

4.7 Numerical results

Table 1: Elementary cycle expansion results (39) computed Schreiber 1992 calculation [55] (and this paper) in the elementary cell.

n_p	# cycles	$\zeta(0,0)$	λ	D
1	0	-	-	-
2	24	-0.31697	1.330	0.375
3	64	-0.54152	1.435	0.339
4	168	-0.09764	1.902	0.284
5	516	0.02334	2.324	0.215
6	1589	-0.00481	1.975	0.133
7	5700	-0.01241	1.885	0.184
8	20729	-0.01006	1.785	0.247

Elementary cycles and the corresponding cycle expansion calculation results are listed in Table 1. Although the diffusion coefficient computed using elementary cycles up to $n_p = 8$ is close to the numerical experiment value 0.25, the convergence is not promising, as have pointed out in ref. [55, 155].

Table 2: Results for $w=0.3$. Calculation in the fundamental domain . Gaspard 1992 note: “My numerical estimate for the Lyapunov exponent when $w = 0.3$ is $\lambda = 1.760 \pm 0.002$, which supports the result of this table.” The numerical diffusion coefficient is calculated using Green-Kubol method.

T_p	# cycles	$\zeta(0,0)$	λ	D
1	5	-0.2169759	1.39193	0.37795
2	10	-0.0248233	1.74541	0.23118
3	33	-0.0221962	1.72235	0.25257
4	108	-0.0002192	1.74450	0.24165
5	373	0.0023463	1.76079	0.24468
6	1378	0.0096330	1.75610	0.24068
numerical experiment			1.760	0.25

We list the numerical results computed using the fundamental domain orbits (Equation (46)) in Table 2. Compared with other methods, the symmetry-reduced

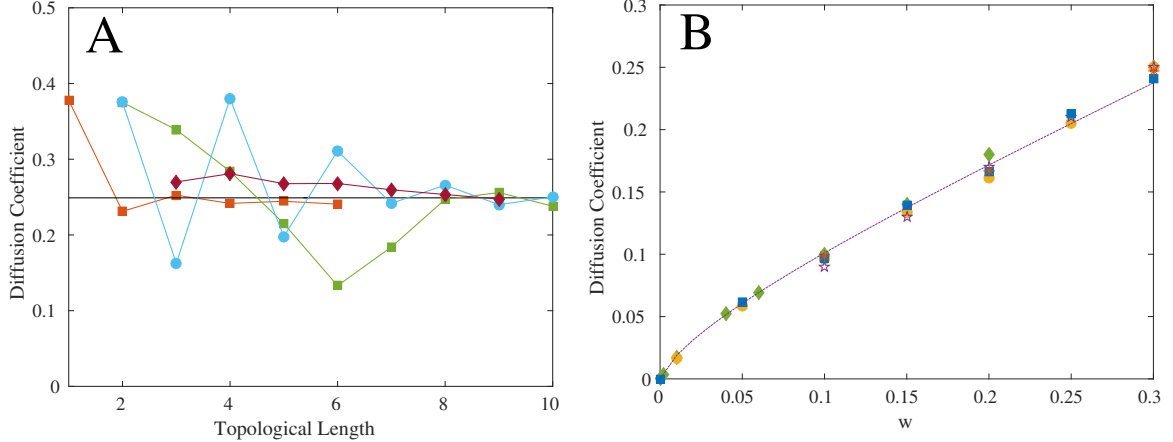


Figure 41: (A) The convergence of diffusion coefficients calculated using cycle expansion in elementary cell (green squares), fundamental domain (orange squares). We also show the convergence of “periodic orbit expansion” method, with and without Shanks transformation (circles and diamonds) discussed in ref. [155]. Here $w = 0.3$. (B) Diffusion coefficients as a function w . Figure generated using data from various resources. Diamonds are results from Green-Kubo numerical experiments [141]; stars [20] and circles [80] are calculated from escape rate; and triangles are given by Hausdorff fractal dimension calculation [80]; dashed line is a statistical approximation from [11].

cycle expansion method converges the fastest, see Table 2 and Figure 41A. Diffusion coefficient computed from ~ 2000 fundamental domain cycles of topological length up to 6 converges to two significant digits, while the elementary cell calculation needs over ~ 10000 cycles in order to converge.

We also compute the diffusion coefficient for $w = 0.05, 0.10, 0.15, 0.20, 0.25, 0.30$. The results are compared with previous numerical experiments and a recent statistical estimation, see Figure 41. In Green-Kubo velocity auto-correlation method the diffusion coefficient can be extrapolated to the accurate reference value 0.250 (at $w/r = 0.30$), using ensembles of $10^6 \sim 10^7$ random trajectories that fly for an extensive period ($T > 20$) [141]. The number of bounces for each trajectory are typically greater than 20 (as compared to 6, the topological length of longest periodic orbit we used). On the other hand, while statistical approach yields a smooth analytical formula [11], the diffusion property in such systems is fundamentally never a smooth

function of parameters [50]. Unfortunately, for the 2D system we do not have enough numerical precision to monitor the fractal behavior of diffusion coefficient observed in ref. [50].

4.8 Conclusion

We have thus obtained a description of global diffusive properties of an infinite periodic dynamical system, such as the Lorentz gas, in terms of periodic orbits restricted to the elementary cell. These formulas have been tested extensively in refs. [55, 20] on the Lorentz gas, and in ref. [14] on 1-dimensional mappings. Related trace formulas have been independently introduced and tested numerically in ref. [214]. The formalism has been generalized to evaluation of power spectra of chaotic time series in ref. [56].

Honesty in advertising requires disclaimer; no such fractal behavior of the conductance has been detected experimentally so far. In practice, the periodic orbit evaluations of the diffusion constant converge poorly compared with averages over scalar quantities such as the Lyapunov exponents. These difficulties are due to several reasons:

1. the diffusion coefficient is not a mean but a variance which is always more difficult to evaluate than mean quantities like Lyapunov exponents;
2. until this work, there was no formula for the diffusion coefficient in terms of the periodic orbits of the fundamental domain;
3. systems like the Lorentz gas do not have simple symbolic dynamics and the analyticity of the associated zeta functions may also be affected by the flow discontinuities associated with the grazing trajectories (trajectories tangent to the disks).

CHAPTER V

SNAKE LOCOMOTION AND CONTROL IN HETEROGENEOUS ENVIRONMENTS

Results and discussions here are based on unpublished work. Snake experiments were conducted by Perrin Schiebel.

5.1 Introduction

Snakes maneuver in nearly all natural terrains. They use versatile locomotion modes such as lateral undulation and sidewinding. During lateral undulation (i.e. slithering), the snake contracts its muscles to create horizontal waves propagating from head to tail. The body bends provide thrust forces through frictional contacts with the ground and/or by pressing against irregularities in the environment. On sand surfaces, some snake species (e.g. the rattlesnake *Crotalus cerastes*) use the peculiar sidewinding gait, in which the body adopts an elliptical-helix shape composed of both horizontal and vertical traveling waves [144]. While principles for lateral undulation [104] and sidewinding [18] were proposed and tested on robotic platforms [86], such templates cannot fully capture the complexity and richness observed in snake locomotion [90, 112, 77, 154]. While snakes were assumed to use various sensing mechanisms during locomotion, to our surprise, there have been no systematic studies on this topic. We posited that, by studying the relation between sensing information and changes in snake behavior during locomotion, we can better understand why snakes are adaptive to various heterogeneous environments.

We chose the shovel-nosed snake (*Chionactis occipitalis*, 18 ± 2 g, 36.6 ± 3.4 cm) as

our model animal. This sand-dwelling snake can perform low-slip subsurface swimming in homogeneous granular media [193]. Recently, Schiebel et al. studied¹ the undulatory locomotion of *C. occipitalis* on granular media both with and without obstacles (pegs), and found that snake individuals used regular traveling waves of fixed parameters through all experimental trials. In this dissertation, we studied the locomotion of *C. occipitalis* on a featureless substrate, a white board. We then incorporated a lattice of pegs into the board and studied how the animal controlled its body to effectively generate thrust.

5.2 Materials and methods

5.2.1 Animal experiment

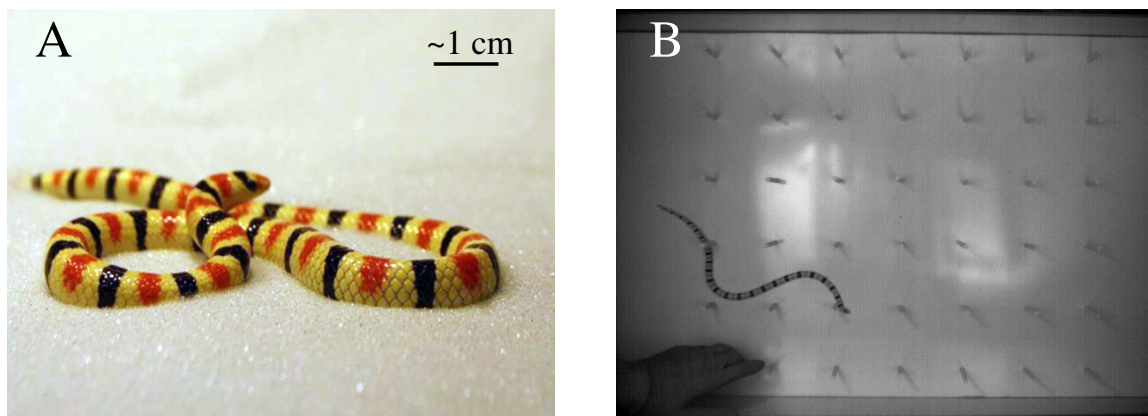


Figure 42: (A) *C. occipitalis* resting on 0.3 mm diameter glass particles. (B) *C. occipitalis* moving in a 9 cm spacing square lattice of pegs on a white board.

C. occipitalis dwell in the Mojave and Sonoran deserts. Individuals were collected in Arizona (by Kevin and April Young) in accordance with a scientific collection permit (no. SP591773) approved by the Arizona Game and Fish Department. All snakes were housed in the Georgia Tech Physiological Research Laboratory (PRL) and experiments were conducted (by Perrin Schiebel) at the Crab Lab under the Georgia Institute of Technology IACUC protocol A11066 and A14067. In both the

¹unpublished work

test and holding areas, the temperature was maintained at $26.7 \pm 1^\circ$, which is the ideal active range for *C. occipitalis* [125].

Rigid, cylindrical pegs of 0.635 cm diameter were 3D-printed using ABS plastic material and arranged into square and hexagonal lattices affixed to white boards. We tested snakes in lattices where the center-to-center distances between nearest pegs varied from 2 to 16 cm. In a 2 cm spacing lattice the gap between pegs was ~ 1.2 cm, comparable to the snake body width at ~ 1 cm; for lattice spacings greater than 16 cm, *C. occipitalis* had a low chance of contacting pegs. All experiments were conducted between 3 PM and 6 PM. Between consecutive runs snakes had 5 minutes to rest, and the total number of trials were limited to 3 per day. Dorsal-view videos were recorded by high-speed cameras (AOS S-Motion) at the frame rate of 250 fps. In order to analyze the kinematics, the videos were digitized in MATLAB, using a custom-written GUI software [193] which tracked the ~ 1 cm spaced black body bands.

5.2.2 Multibody simulation

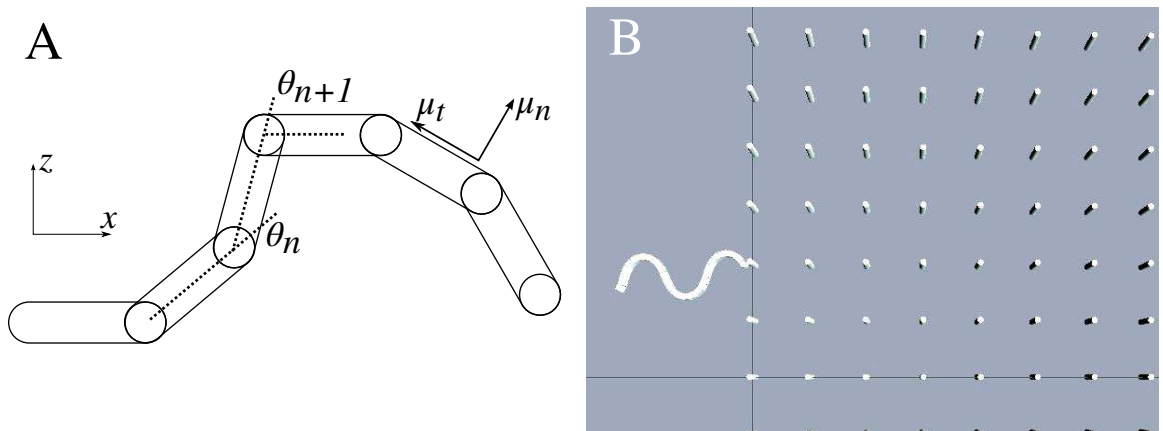


Figure 43: (A) The snake model in simulation. Adjacent rigid bodies (rounded rectangles) are connected by motors (circles). All motions are restricted in the $x - z$ plane. θ_n is the n -th motor actuation angle. μ_n and μ_t are friction coefficients for the normal and tangential directions of each segment. (B) The simulated snake moved in a peg lattice. The distance between two nearest pegs are 0.26 BL, comparable to *C. occipitalis* in a 10 cm spacing lattice.

We used Chrono::Engine [146], a multi-body framework written in C++ to model the actuation and dynamics of a snake in simulation. The simulated snake consisted of $N = 30$ cuboid rigid bodies (Figure 43B), and had a length-to-width ratio $L/w = 24$. Adjacent segments were linked with motors which only allow relative rotation about y -axis. In the basic, template control scheme, motors were commanded to generate sinusoidal rotations with uniform phase delay from head to tail segments, i.e.:

$$\theta_n(t) = A \sin\left(\frac{2\pi}{T}t + \frac{\xi n}{2\pi}\right), \quad (47)$$

where θ_n was the angle of the n -th motor, A the maximal rotation angle, T the undulation period and ξ the number of waves along the body. This template scheme produces a serpentine wave [99]. We also introduced a feedback controller to model the snake behavior when they interacted with pegs (see Section 5.3).

In experiment, *C. occipitalis* moved laterally on a flat surface with no significant lifting (such as climbing over pegs) observed, we constrained the simulated snake to a 2D plane, allowing translations in x and z directions, and rotations about y direction. The ground-belly interaction was modeled using anisotropic Coulomb friction. An anisotropy ratio (defined as the ratio between μ_n , the friction coefficient along the normal direction of the slender body, to μ_t , the friction coefficient in the tangent direction) that was greater than 1 allowed the slender body to propel forward [104]. At $\mu_n/\mu_t = 3$ the simulated snake moved at an undulation efficiency $\eta = 0.25$ (the traveled distance in a cycle divided by the body length), which quantitatively matched snake experiment results on the white board. We added frictionless, rigid, cylindrical pegs, separated at the same relative spacings d/L as in experiment (Figure 43A and B).

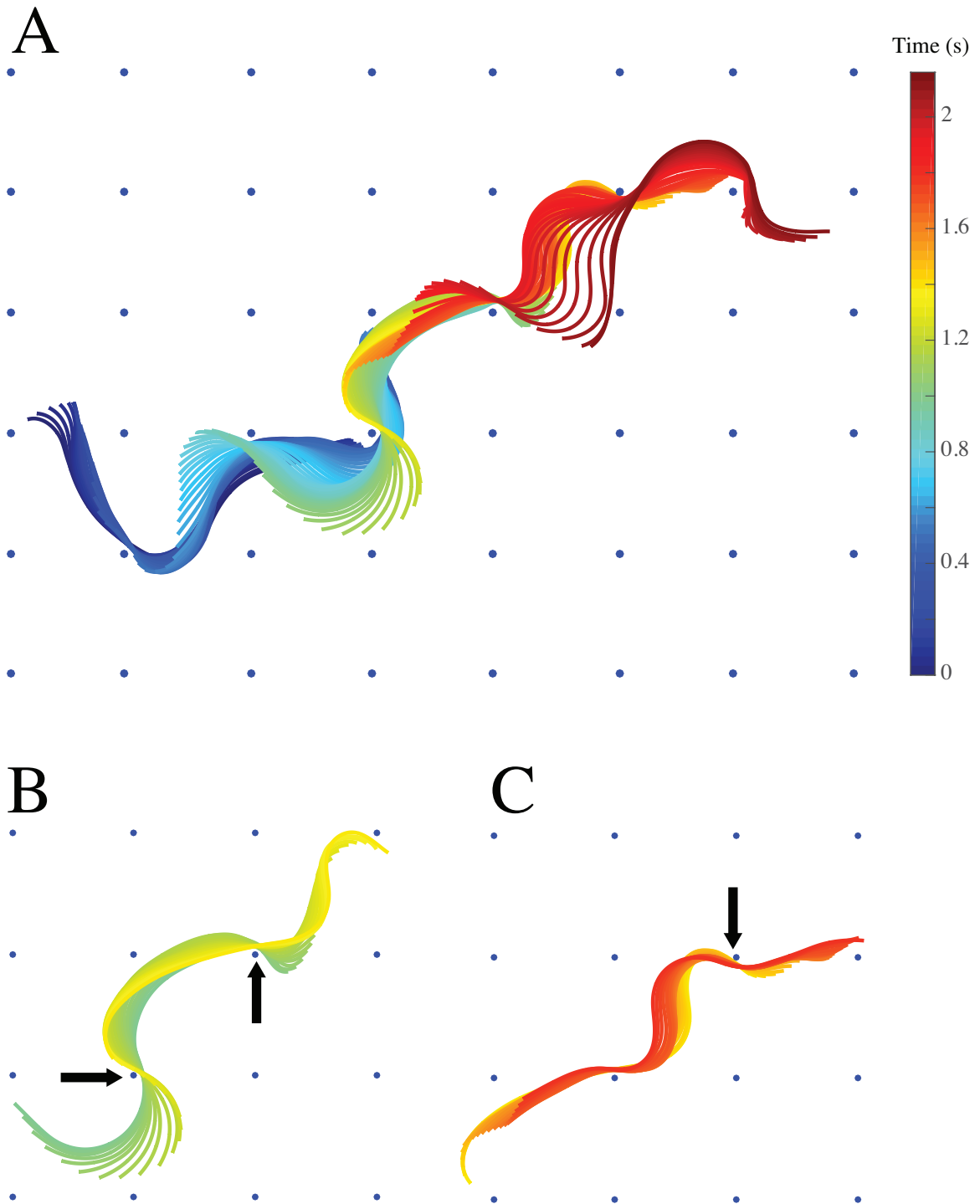


Figure 44: *C. occipitalis* traveled in a square lattice of 8 cm spacing. (A) Sequential positions of the snake. The temporal interval between two frames are 0.02 s. Blue dots indicate peg positions. Color represents time. (B) and (C) are isolated subsequences from (A). Arrows indicate the pegs being contacted. See text for details.

5.3 Results and discussions

5.3.1 Kinematics

Currently, there is no universal way to quantitatively characterize the undulatory wave pattern of snake, partly because it is mathematically challenging to parameterize a continuous curve of unknown class using only a few meaningful variables. Stephans et al. have explored the “eigenworm” decomposition [200], using time-correlated principle component analysis (PCA) to project the high-dimensional spatial configuration of nematodes (*C. elegans*) into a low dimensional behavior hyperplane. The method worked well when the movement pattern was regular and repeatable. As Schiebel et al. demonstrated, *C. occipitalis* undulation shape on sand surface can be reconstructed with 95% accuracy, using the first two eigen shapes.

In contrast, when *C. occipitalis* moved on a white board in peg lattices, a substantially wide range of waveforms were observed (Figure 44 A). A number of factors contributed to the resulting complexity of the snake’s movement patterns: the smooth, featureless substrate (as a rough analogy, compare to humans walking on ice); the limited free space imposed by the presence of obstacles; and the non-trivial interaction between the animal body and pegs. When interacting with pegs located posterior to the body’s traveling wave, the snake can modulate its axial bending at the point of contact to generate thrust and propel the body forward (Figure 44 B). When a peg stood anterior to the body, the wave shape had to deform (i.e. compress), and the body slipped back (Figure 44 C). Worried that the temporal integral in the PCA covariant analysis may erase such subtle behaviors, we decided to analyze the motion of *C. occipitalis* case-by-case in this study. Specifically, we were interested in the detailed kinematics and control strategy when the snake first encountered a peg.

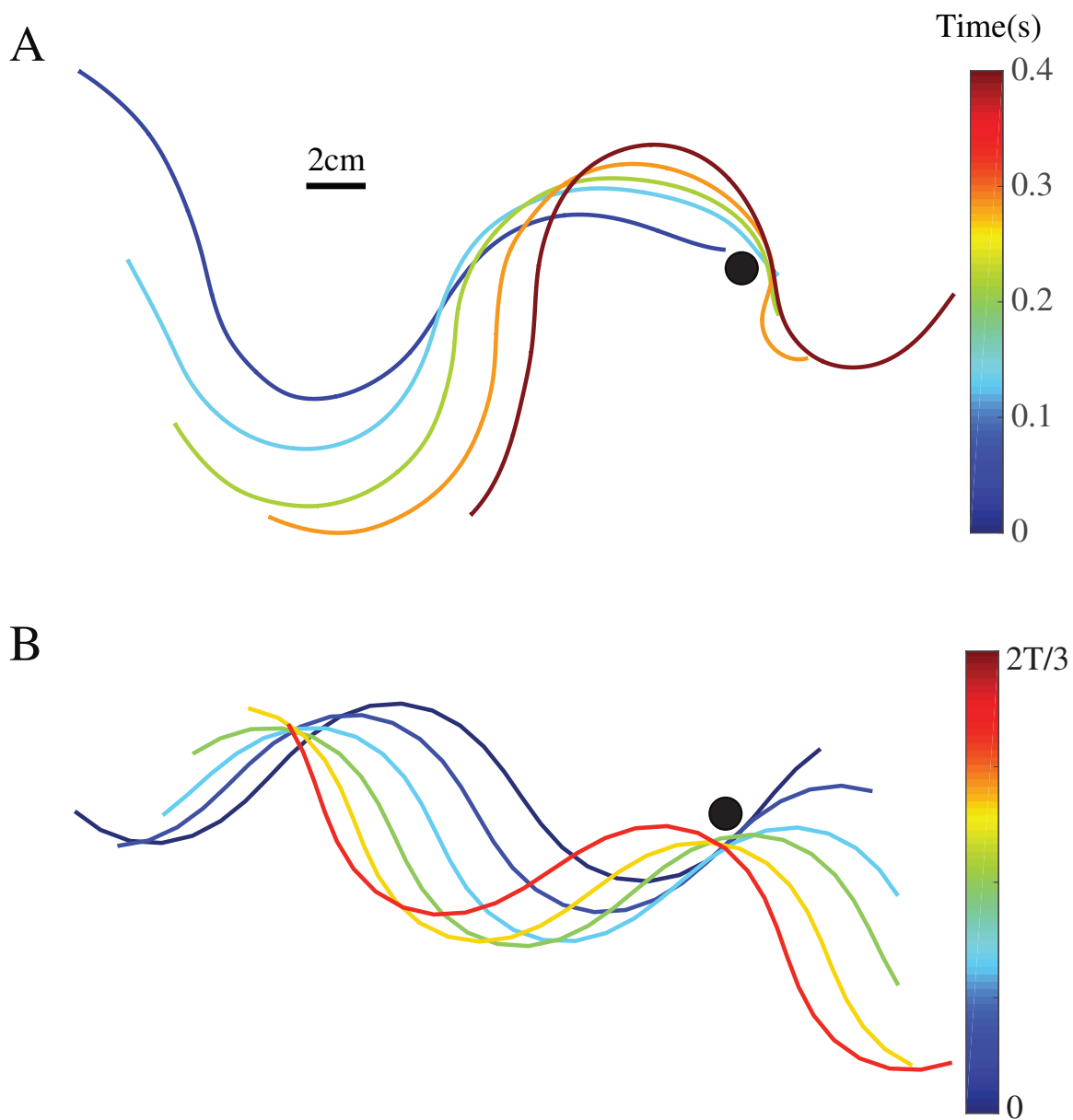


Figure 45: Snapshots of the body shape when (A) *C. occipitalis* touched the peg and (B) when the simulated snake had contacted a peg and was deflected. The time intervals between consecutive plotted frames are ~ 0.1 s in experiment and $\sim T/8$ in simulation, respectively. Color indicates time.

5.3.2 Snake interaction with a single peg

As observed in various literature [90, 77], a snake can propel itself by throwing its body into a “S” shape and pressing on the anterior surface of a single contact site. There have been a few experiment studies on snake movements facilitated by pegs [90, 112, 77, 154]. Qualitatively similar kinematics were documented for different snake species (*Natrix natrix*, *Elaphe obsoleta*, *Python regius*, and *Pituophis melanoleucus affinis*) during the interaction with a single peg. Force measurements were performed [90, 77] and showed that snakes were able to generate forward thrust from the contact that counteracted the frictional drag from the substrate. Although correlations between muscle activity and the kinematics were discussed, no concrete conclusion or testable hypotheses were made. In this study, we connected the propulsion dynamics of *C. occipitalis* with its shape change, and inferred the control mechanism behind the scene.

In our experiment, *C. occipitalis* demonstrated similar maneuverability when it interacted with a single resistance site (Figure 45 A). When the snake touched a peg posterior to its moving direction, the body posture was adjusted to wrap around the peg. The head section of the snake maintained contact while the rest of the body was pulled forward (Figure 45 A, blue to orange lines). After the contact normal was aligned to the desired traveling direction, new bends were generated (Figure 45 A, dark red line) and propagated backward (in the body frame) to continuously press against the peg while the center of mass (CoM) moved forward in the lab frame. Such peg-grabbing behavior may not be explained by a single-mode lateral undulation gait. With only the open-loop serpentine wave template, we found that the simulated snake was deflected to the side immediately and could not effectively use the peg to push its body (Figure 45 B, dark blue to dark red lines). The results were not surprising because the contact force was not initially aligned with the traveling direction. Without a control mechanism, the body was pushed to the perpendicular

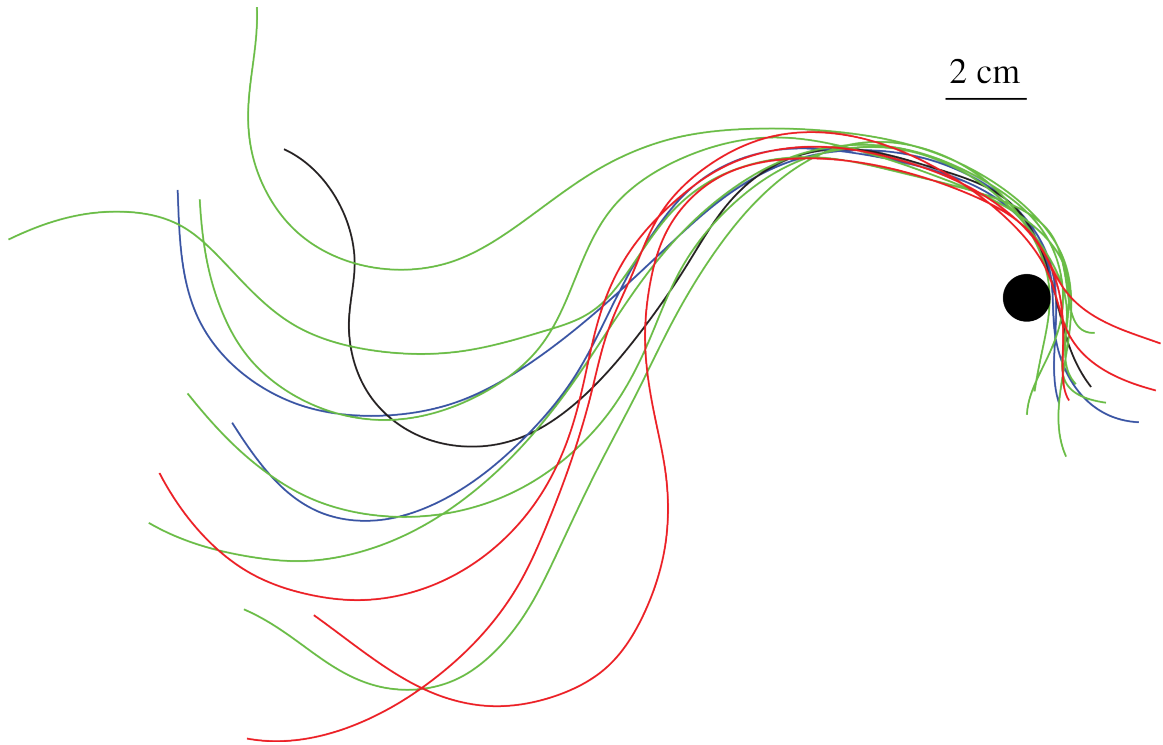


Figure 46: The body shapes adopted by *C. occipitalis* when they began to wrap around the peg. We plotted 14 tracked runs of 3 individuals from 29 instances where grab behavior was observed. Color distinguishes individual snakes. All shapes were aligned to peg positions. Some curves were rotated and reflected. The actual moving direction shall not be inferred from the snapshots.

direction of motion and also rotated away from the peg.

In previous studies, researchers qualitatively characterized the “S” shape being used during the snake-peg interaction. However, little was understood on *how* snakes were able to create such shapes and rotate the initially misaligned contact normal to its movement direction. To answer this question, we examined ~ 150 experiment trials of *C. occipitalis* moving in the peg lattice, and identified 29 instances of single peg interaction. The duration of the grab phase, defined as the elapsed time from when the snake had just touched the peg, to when the snake had aligned the body and was ready to generate a new bend, was 0.24 ± 0.08 s (60 ± 8 frames). For each instance, we extracted the body trajectory at the middle of the grab phase (Figure 46). Although

the body shapes can vary significantly between runs, we observed stereotyped, “C”-shaped conformations near the contact site. Because the shapes were clipped and rotated manually, the exact moving directions are not represented in Figure 46.

The universality in *C. occipitalis* postures suggest that (at least partially) a shape-based control may be used during the grab phase. The C-shape can be achieved by a modulation on top of the normal serpentine wave. To see this, we computed the signed curvature κ_s , which was related to the motor angle in simulation by $\kappa_s \approx \theta_n/l$, where l is the length of a segment. For the representative run (Figure 47), when the snake had just touched the peg (Figure 47A), the curvature at the point right behind the contact site was still increasing (Figure 47D, at $t = 0.04$ s). If the motion followed the serpentine wave template, the signed curvature would increase with a sinusoidal pattern until it reached the positive maximum. However, between $t = 0.05$ s and $t = 0.16$ s, the curvature speed changed sign and κ_s decreased from -0.1 cm^{-1} to -0.7 cm^{-1} . We examined the perturbed wave form at $t = 0.15$ s (Figure 47D, the vertical dashed line in the middle) and observed the C-shape pattern near the head portion (Figure 47B). At $t \approx 0.16$ s, $\dot{\kappa}_s$ changed sign again from negative to positive. κ_s increased for the next ~ 0.1 s until a new bend was generated at $t \approx 0.25$ s (Figure 47C).

We noticed that the sign change of the curvature speed occurred at all tracking points between the contact location and the center of the first bend (indicated by the maximum of the absolute curvature $\max |\kappa_s|$) behind the contact. By modulating the motor angle θ in a similar way to the snake, we may create a similar C-shape in the simulated snake. We hypothesized that using the C-shape was a key ingredient to successfully grip the peg.

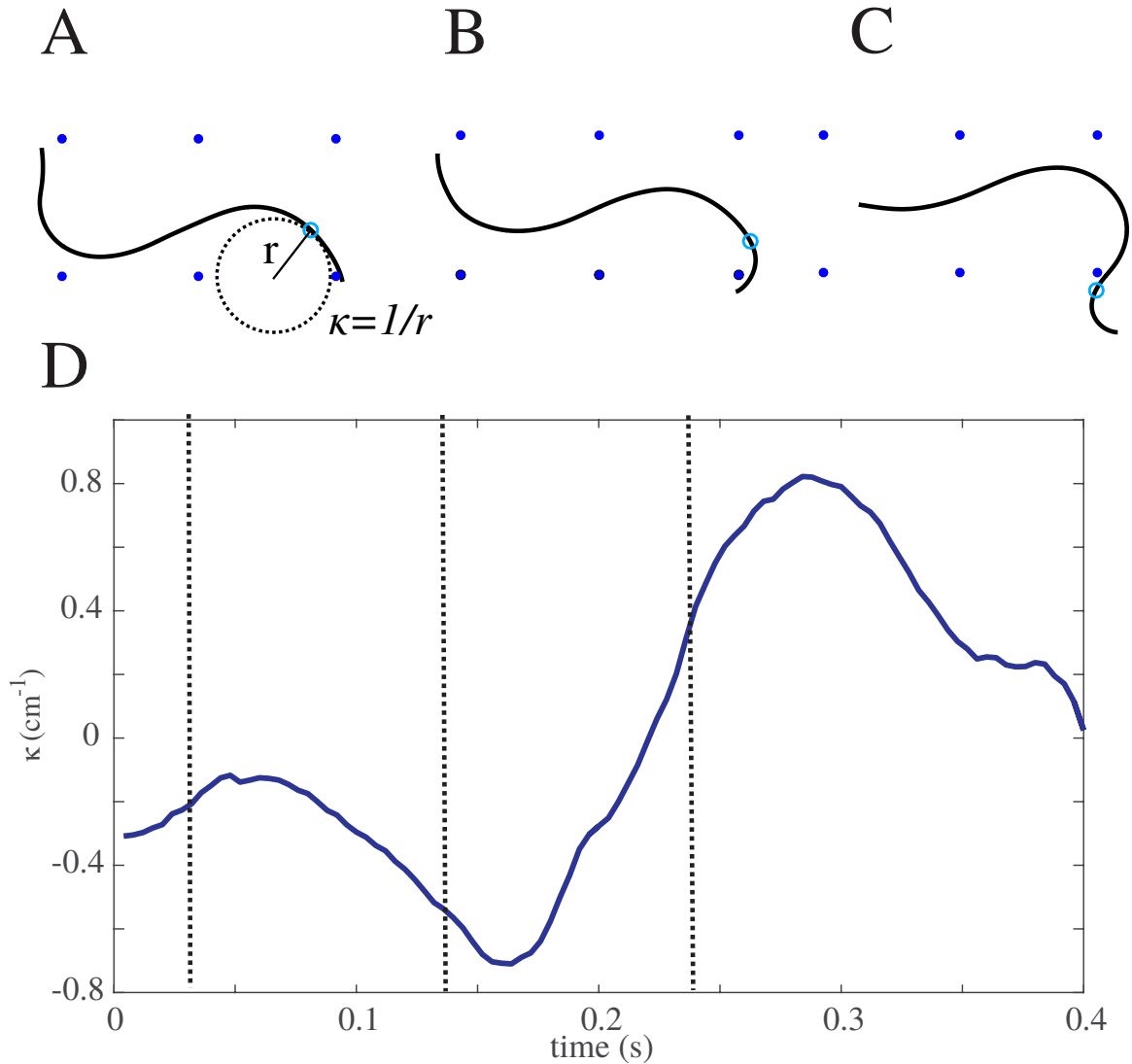


Figure 47: A representative trial showing the shape and curvature changes of *C. occipitalis* during the interaction with a peg. Top row, the snake shape in configuration space when (A) it just contacted a peg, (B) when it actively modulated the wave to grab the peg, and (C) when the grab phase finished and the wave resumed the nominal form (serpentine wave). The spacing between nearest pegs (blue dots) was 9 cm. (D) the curvature κ vs time plot for the representative point (blue empty circle in A, B and C). Dashed vertical black lines indicate the time frame at which the snapshots in the top row were taken. κ was computed by fitting circles at the selected point.

5.3.3 Improved controller

To test our hypothesis, a feedback controller was introduced to monitor contacts in real time and adjust the curvature accordingly. Instead of interpolating the kinematics directly from the snake data, we were inspired by the “lateral inhibition” method, an evasive control mechanism proposed by Hirose et al. [99], which enabled ACM (a snake robot built on wheels [99]) to generate adaptive propulsions in a winding tunnel. In our control scheme, we applied forces to the curvature:

$$\dot{\theta}_n = -\text{sign}(\dot{\theta}_n)\Theta(n, m) - k_p(\theta_n - \theta_n^{(d)}) - k_d(\dot{\theta}_n - \dot{\theta}_n^{(d)}), \quad (48)$$

to modify the motor bending angles near the segment in contact with a peg, and introduced proportional k_p and derivative k_d terms to stabilize the motion pattern near the serpentine wave template which was prescribed by $\theta^{(d)}$ (Equation 47).

The term $\Theta(n, m)$ denoted the contribution of a contact at the segment m near the head portion ($m < N/3$) to the angle of n -th motor. We chose

$$\Theta(n, m) = \begin{cases} K \exp\left(-\frac{1}{2}\left(\frac{n-m}{\sigma}\right)^2\right) & m < N/3, \\ 0 & \text{otherwise,} \end{cases} \quad (49)$$

where K controls the strength of the extra bending, and σ indicates the scale of non-locality. In simulation we set $\sigma = 4$, so the length scale of the Gaussian function matched the quarter wavelength of $\frac{N}{2\xi} = 5$ segments. This allowed simultaneous modification of ~ 5 motors between the contact position and the center of the first bend behind it.

5.3.4 Simulation results

We tested the prototype controller in simulation (Figure 48). With touch sensing enabled, the simulated snake generated the C-shape while interacting with the peg (Figure 48, green line), and was able to drag the rest of the body forward (Figure 48, blue to orange lines). There was less change in the snake orientation after the peg

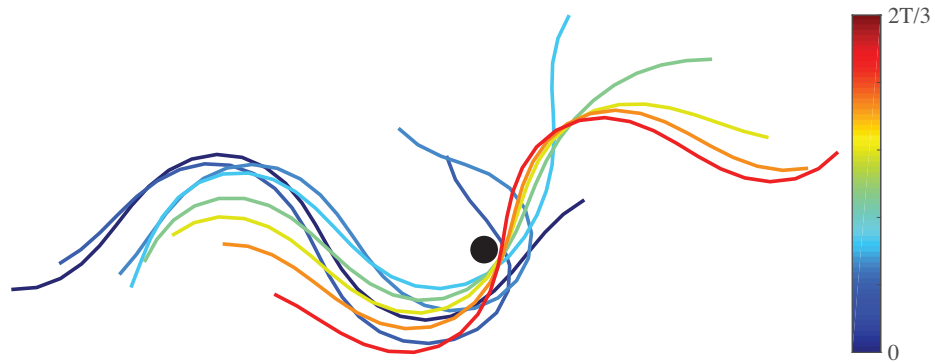


Figure 48: Touch sensitive controller enabled the simulated snake to grab. Filled black markers show the location of the peg.

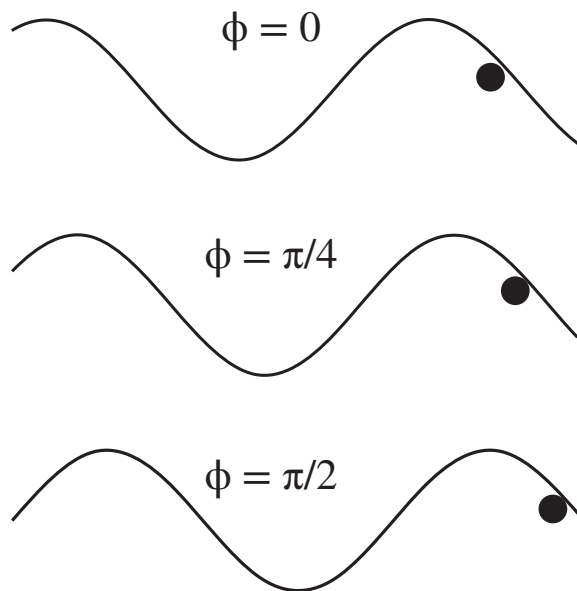


Figure 49: Diagrammatic illustration of the effects of initial positions on the first contact point along the body. Filled black markers show the relative positions of the pegs.

interaction. Instead of being deflected as in the open-loop passive case, the next bend propagated from the head portion and subsequently pushed the snake forward (Figure 48, dark red line).

We then systematically ran simulations to quantify the performance of the new controller. In the setup, a single peg was set at $(0, 0)$. At the beginning of each simulation we placed the snake at $(-L, 0)$, and aligned the body axis towards the peg. By varying L we can control ϕ , the phase of the serpentine wave at the instance the simulated snake encountered a peg (Figure 49). L was chosen such that the snake can touch the peg soon (within $T/6$) after simulation started and there were enough variations in the contact phase ϕ to cover $(0, \pi/2)$ —because of the mirror symmetry about x -axis, only $\phi \in (0, \pi/2)$ were considered. We tested two anisotropy factors $\mu_n/\mu_t = \{3, 1\}$. When $\mu_n/\mu_t = 3$ the simulated snake moved at a mean speed of 0.25 BL/cycle without pegs, close to the observed performance of *C. occipitalis* on white board. At $\mu_n/\mu_t = 1$ (i.e. isotropic friction) the simulated snake could not move forward because the average thrust and drag forces always balanced within a undulation cycle. Thus any extra movements in x -axis were generated from interactions with the peg.

We plotted ~ 400 simulation trajectories in Figure 50. For anisotropic ground friction and an open-loop controller (Figure 50A, dashed trajectories), the simulated snakes did not have any chance to manipulate the peg and were deflected towards $-z$ direction at similar angles, regardless of initial contact positions. The results were thus insensitive to the contact phase, and all trajectories converged to the location $x_e \approx 0.18$ BL at the end of simulation. The situation was worse when friction forces were isotropic (Figure 50B, dashed lines). The simulated snake was not only pushed perpendicular to the target x -direction but also slightly backwards, resulted in $x_e < 0$ (Figure 51, the right red bar).

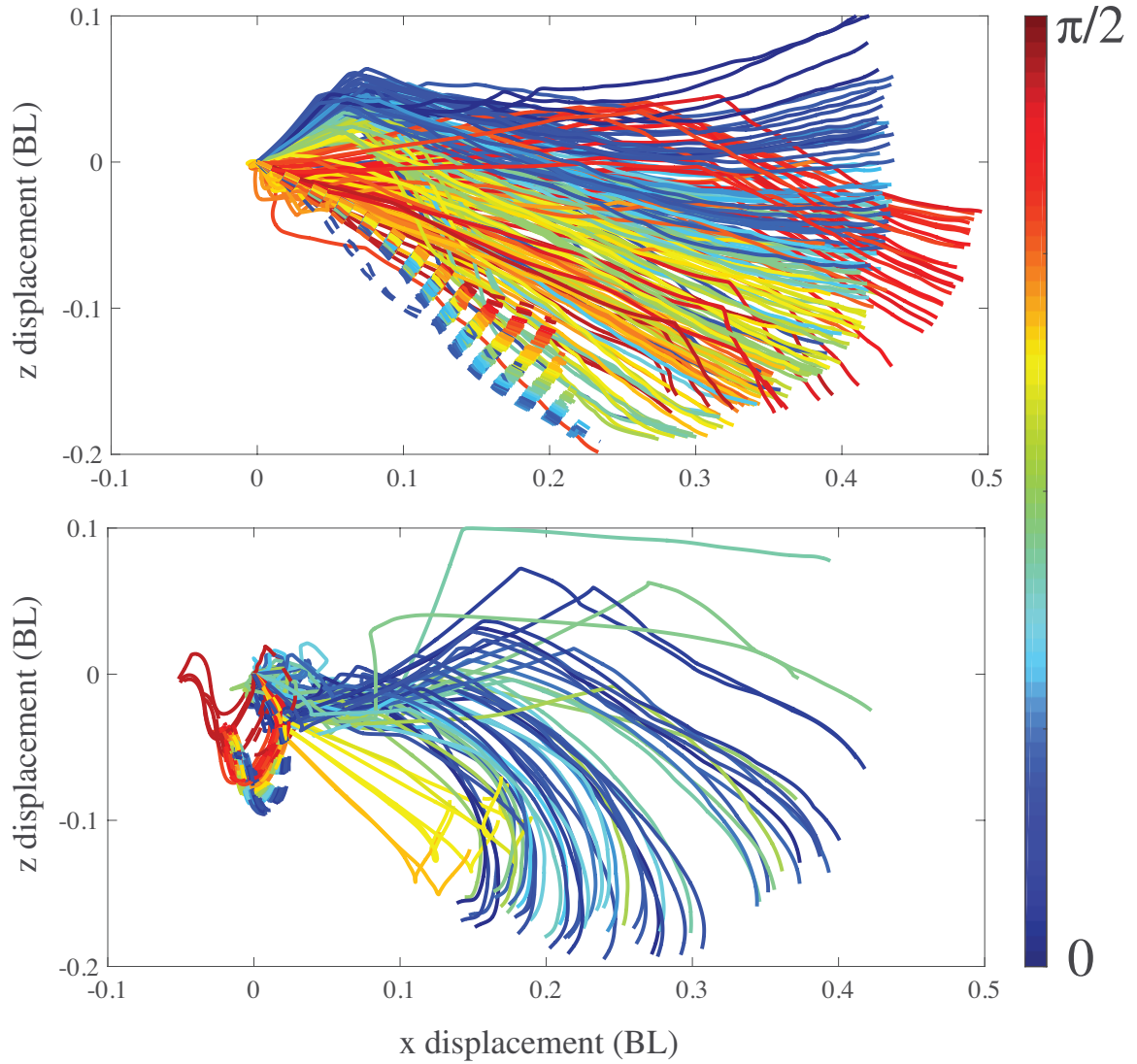


Figure 50: The center of mass (CoM) trajectories in simulation when the feedback controller was enabled (solid lines), and disabled (dashed lines) for (A) $\mu_n/\mu_t = 3$ and (B) $\mu_n/\mu_t = 1$. For each combination of controller condition and anisotropy factor, ~ 100 simulation runs were conducted. We subtracted the initial CoM position from each run to compare the relative displacements. Color represents the phase at the time of contact, see details in Figure 49. The simulation time for the plotted trajectories was 1 undulation cycle (T).

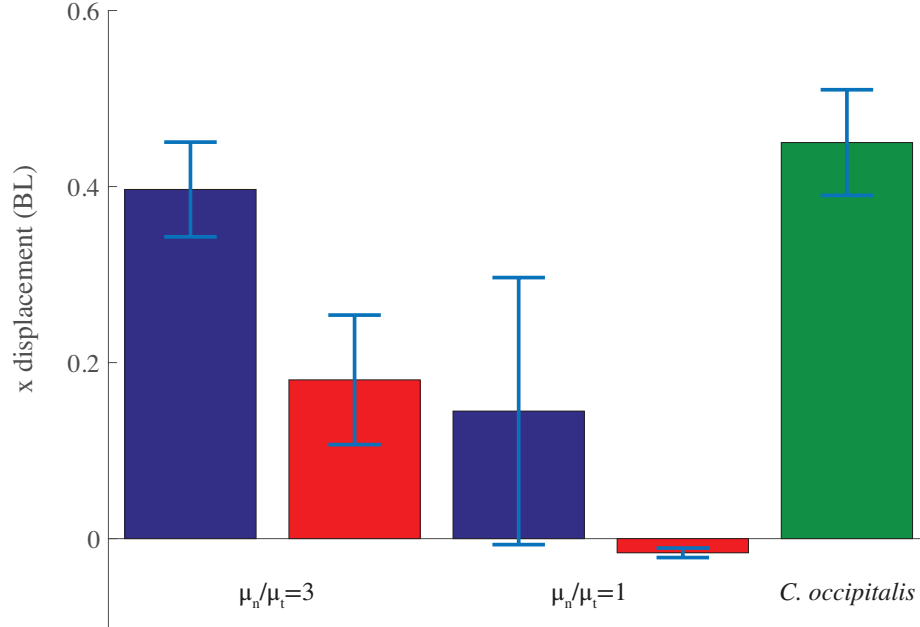


Figure 51: The performance of the simulated snake (measured by the displacement in x direction after a cycle) with (blue bars) and without (red bars) the controller. Error bars show the standard deviation. The green bar shows the performance of *C. occipitalis* in a single cycle using active grab.

In contrast, the performance of the feedback-controlled snake had a sensitive dependence on the contact phase (Figure 50A and B, solid lines). The controller introduced non-trivial interactions between the snake and the peg. The grab phase began when the simulated snake first touched the peg. Due to the nature of LCP solvers used in Chrono::Engine and the stiffness of rigid bodies being used, the contact forces were over-estimated. As a result, the contact broke shortly while the controller was still modulating the body shape. Within a single cycle, multiple collisions can occur (Figure 50A and B, turning points on solid lines), and the controller may issue more grab commands if the contact point is still near the head.

When $\mu_n/\mu_t = 3$, the total x -displacement, x_e , in a undulation cycle (after the initial collision) was 0.40 ± 0.05 BL (Figure 51, the left blue bar). Compared with the passive case where $x_e = 0.18 \pm 0.07$ (Figure 51, the left red bar), the increase in performance was over 100%. Additionally, the simulated snake achieved similarly

x-displacement as the real snake at 0.45 ± 0.05 BL (Figure 51, green bar).

For the isotropic condition $\mu_n/\mu_t = 1$, the feedback controlled snake was able to manipulate the peg and generate thrust for $\phi \lesssim 1.0$ (Figure 50 B, blue and green solid lines). For simulation with $\phi > 1.2$, x_e decreased to ~ 0 BL, and the trajectories (Figure 50B, red solid lines) were similar to the passive case (Figure 50B, dashed lines). The results were not surprising, because at first contact, the portion of the snake body ahead of the peg decreased with increasing ϕ (Figure 49B). When only the first segment (behind the head) touched the peg, a subsequent grip action may force the entire body to slip off the edge (Figure 51, the right blue bar and dashed horizontal line). Detailed sequential snapshots indicate that, with the current controller, the simulated snake failed to rotate the contact normal effectively when there was little thrust from the substrate.

5.4 Conclusion

We studied the locomotion of *C. occipitalis* in a heterogeneous setting. To generate thrust on the featureless substrate (white board), *C. occipitalis* actively manipulated its contact with a single resistance site (i.e. a peg). From a kinematics analysis, we hypothesized that *C. occipitalis* modulated its wave template using a shape-based control method. Based on our experimental findings, a close-loop controller using touch feedback was proposed and tested in simulation. We observed that the feedback controlled snake was able to grab pegs and improved its mobility.

While simulation has provided insight into the use of closed-loop undulatory control around pegs, certain features of simulation, i.e. intermittent contacts between rigid bodies, resulted in unrealistic conditions that a robotic snake would not encounter. Thus, we next intend to test the controller in a robot snake (Figure 52). Also, the observations and results in this chapter are limited to a single contact scenario. It remains to be studied how snakes control their bodies when multiple contacts

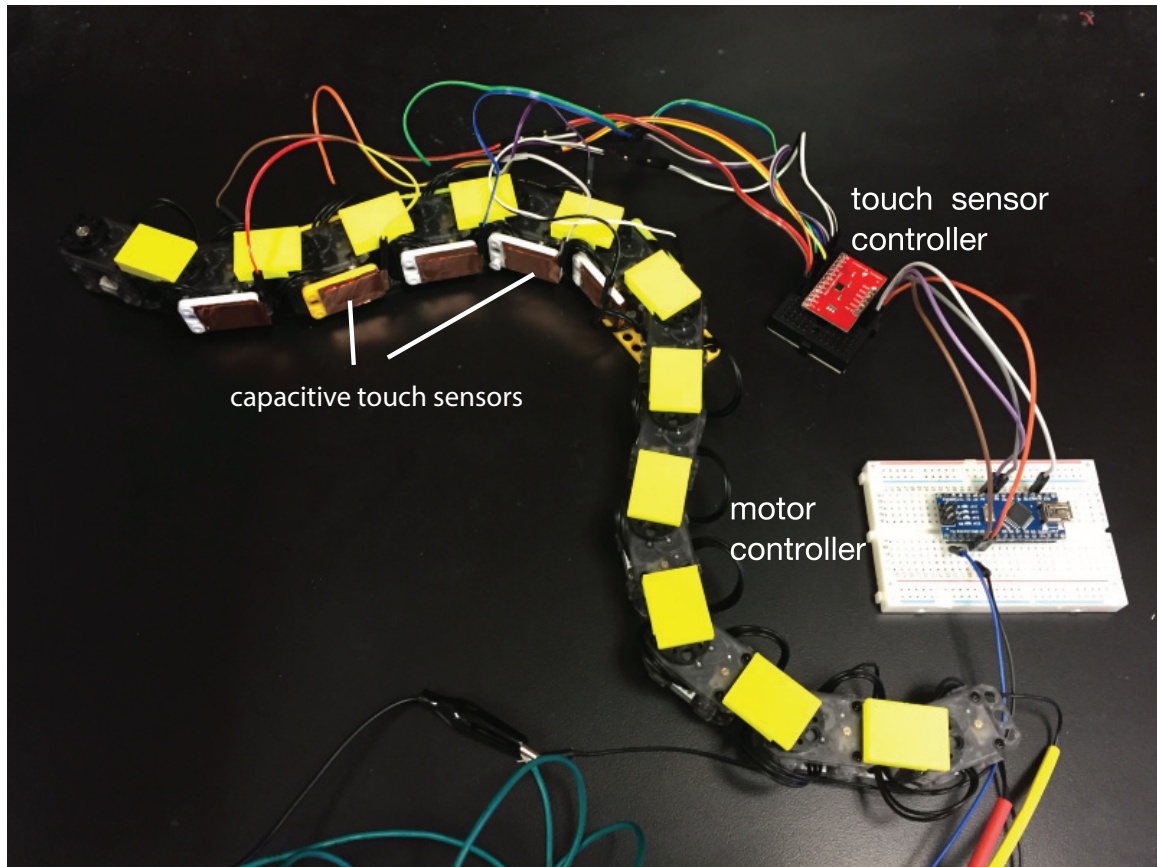


Figure 52: The snake robot with touch sensing capability. The body was built with 12 Dynamixel XL-320 motors. Adjacent motors were linked by 3D printed brackets (yellow square parts). All motors were connected to a serial bus and can be controlled individually using the Arduino Mini board. We taped copper foils to the side of motors to detect the capacitance change upon touching. Sensing information was gathered by a MPR121 breakout board (SparkFun parts) and processed by the Arduino.

are presented.

CHAPTER VI

CONCLUSION AND FUTURE WORK

6.1 Summary

In this dissertation, we developed predictive models for legged and limbless locomotion on dry, homogeneous granular media. The vertical plane Resistive Force Theory (RFT) for frictional granular fluids accurately predicted the reaction forces on intruders (with complex geometries) translating and rotating at low speeds ($\lesssim 0.5$ m/s). Using RFT and multibody simulation, we predicted the forward moving speed of legged robots. During the locomotion of lightweight robots and animals where instantaneous limb penetration speed can reach values greater than ~ 0.5 m/s, a Discrete Element Method (DEM) simulation was developed to capture the limb-ground interaction. We showed that hydrodynamic-like forces generated by accelerated particles can balance the robot weight and inertia, and promote the rapid movement on granular media. Forces from the environment can not only determine locomotion dynamics, but also affect the locomotion strategy. We studied and simulated the limbless locomotion of snakes in a heterogeneous environment and demonstrated how touch sensing was used to adjust the movement pattern. In heterogeneous environments, the long-term locomotion dynamics is also poorly understood. We presented a theory for transport and diffusion in such settings.

Our studies indicated that it is possible to create high-fidelity models for movement on flowable terrains, by understanding the interaction between the locomotor and the environment. In heterogeneous environments where uncertainties (to the locomotor) are present, it is important to actively sense the interactions and integrate the feedback information to the locomotion strategy. Because we used a hybrid

approach including multibody simulations and robots (i.e. robophysics), these results can be immediately applied to legged and limbless devices moving in complex environments.

6.2 Future Directions

6.2.1 From RFT to plasticity theory

While RFT had many successes, there are regimes in which the theory showed discrepancy/did not apply. The current formulation of granular RFT assumes that the forces acting on elements are described by steady state drag forces. This approximation is valid at low Reynolds numbers, since, upon a sudden movement of a body to a constant speed, the accompanying flow fields are developed rapidly (the so-called instantaneity assumption [91]) and are thus time independent for such an interaction. However, in granular media, even for low constant intrusion speed, the material can change state over timescales relevant to the intrusion event. The $\sim 30\%$ over-prediction of sand-swimming speeds in RFT compared to the DEM in Ref. [65] was attributed to such a transient effect.

Several aspects of interaction with surfaces were not incorporated into the granular RFT. For example, unlike fluids, soft materials like sand can display memory effects: for example, GM can form sand craters upon impact [221, 213], which will not be removed (as in a fluid) by the spontaneous fluctuations of particles or by further flow (since the material solidifies post-impact). We have discovered that such effects in which surface properties change due to disturbances can play significant roles in locomotor performance. In studies of the locomotion of a flipper-based robot, drag and penetration forces were found to decrease substantially if an intrusion occurred close to previously disturbed ground [148]. Such memory effects of disturbed ground were posited to be the cause of locomotor failure [148, 135] during surface movement.

Recently, the group led by Kamrin has made progress in developing a plasticity

theory for intrusion forces in granular media [17]; Aguilar and Goldman have explained, for the first time, the “added-mass effect” during rapid impact on granular media [2]. The promising new theories may help us understand both the transient phenomena and hysteresis. In future studies, we could integrate the new models to our multibody simulation. We expect that this approach can predict locomotion dynamics more accurately for a broader terrain conditions, and also explain the failure modes observed in experiments.

6.2.2 Locomotion on wet granular media

In this dissertation we did not discuss locomotion on and/or within wet granular media. Although there have been scattered efforts to understand the mechanisms that nematodes [117] and polychaetes [66] used to burrow in mud, this topic remains largely unexplored due to the complexity of the media. In wet granular media, water can form bridges between adjacent particles [152] and introduce long-ranged, attractive inter-particle forces. Depending on the water content, the rheology and resistive properties of the material can significantly vary [163]. Recently in our lab, a novel experiment method was developed to control and prepare wet granular media into a repeatable state [194]. With this new technique, principles of lizard burrowing in moisturized granular media (when water volume is below $\sim 15\%$) were revealed. However, theories and simulations are still lacking. In future studies, we may modify the force model in DEM simulation to include long-ranged, attractive force from the water bridge. Once validated, we can simulate locomotion on moisturized granular media. For high water content substrates such as sea sediments and muds, a particle-fluid co-simulation can be considered to understand the complicated physics of such interactions.

6.2.3 Control of limbless locomotion using multiple contacts

In this dissertation we have studied the locomotion of *Chionactis occipitalis* on smooth substrates, and revealed how the snake generated propulsions from a single contact site. However, the mechanism by which *C. occipitalis* interacts with *multiple* contacts is still unclear. When moving in a (relatively) dense lattice of pegs, depending on contact locations and their normal directions, the snake may compress part of its body to avoid collisions with certain pegs, while pushing against other sites to gain thrust. Understanding the control scheme behind such behavior may not only advance our knowledge in snake locomotion, but also help design robotic arms that manipulate in cluttered environments. In future studies, we will investigate snake control in peg lattices in simulation, and build touch-sensitive snake robots to test the controller's performance.

APPENDIX A

DETAILS IN RESISTIVE FORCE THEORY

This chapter was published in [136].

A.1 Depth-only force models and their limitations

Previous studies of intrusion forces in granular media focused on simple intruders (e.g. plates, rods, and spheres) moving with simple kinematics (e.g. vertical penetration and horizontal drag). For example, the vertical force F_z on a horizontal plate element ($\beta = 0$) moving vertically ($\gamma = \pm\pi/2$) in granular media was observed to be proportional to the plate's depth $|z|$ and area A [135, 98]:

$$F_z = \alpha_z(0, \text{sgn}(\dot{z})\pi/2)|z|A. \quad (50)$$

Similarly, the horizontal force F_x on a vertical plate element ($\beta = \pm\pi/2$) moving horizontally ($\gamma = 0$) in granular media was proportional to plate depth $|z|$ and plate area A [7, 147, 87]:

$$F_x = \alpha_x(\pi/2, 0)|z|A. \quad (51)$$

where \dot{z} is the velocity of the plate in the vertical direction, and $\alpha_z(0, \text{sgn}(\dot{z})\pi/2)$ and $\alpha_x(\pi/2, 0)$ are vertical and horizontal stresses per unit depth for $(\beta, \gamma) = (0, \pm\pi/2)$ and $(\pi/2, 0)$ (determined from measurements in Figure 21, B and C).

Both the vertical penetration and horizontal drag force models only account for the dependence of stresses on the intruder's depth ($|z|$), but not the dependence on its orientation (attack angle β) or movement direction (intrusion angle γ). Hereafter we refer to these force models as the “depth-only force models”.

In previous studies of legged locomotion on granular media [134, 135, 147], due to the lack of the resistive force model, the forces on a complex intruder were estimated

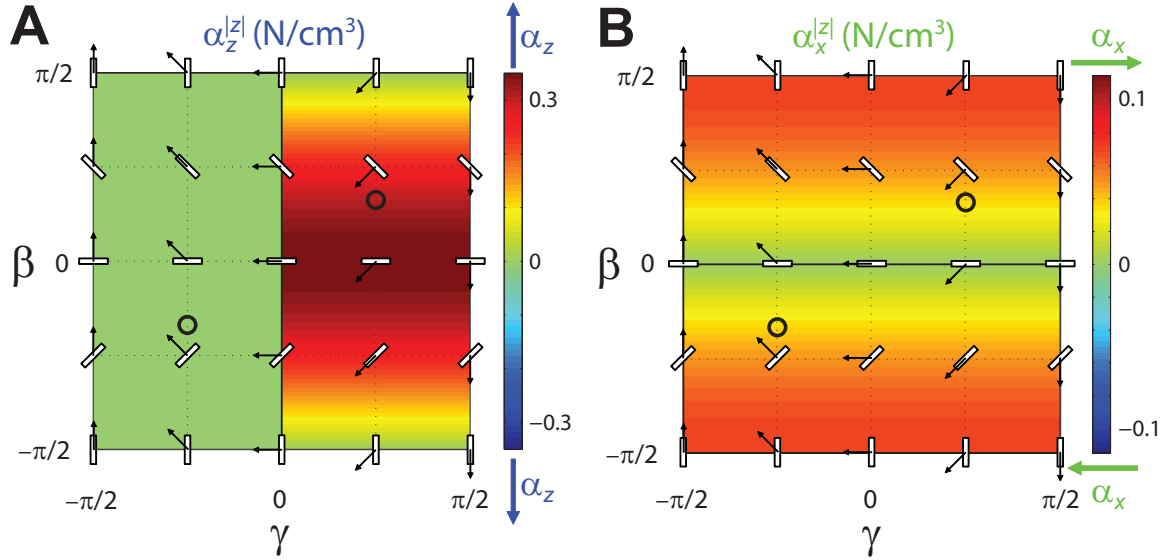


Figure 53: Effective vertical ($\alpha_z^{|z|}(\beta, \gamma)$, left) and horizontal ($\alpha_x^{|z|}(\beta, \gamma)$, right) stresses per unit depth as a function of attack angle β and intrusion angle γ for loosely packed poppy seeds, calculated from Equation 54 using $\alpha_z(0, \text{sgn}(\dot{z})\pi/2)$ and $\alpha_x(\pi/2, 0)$ measured in experiment (Figure 21, B and C). See Figure 20 schematic of the experiment and definition of variables.

from the depth-only force models, using the flat-plate approximation: The vertical force on a leg element of area dA_s and arbitrary β and γ was approximated by that on a horizontal leg element whose area was the element area projected into the horizontal plane [134, 135]:

$$dA_{zs} = |\cos\beta|dA_s. \quad (52)$$

Similarly, the horizontal force on the leg element was approximated by that on a vertical leg element whose area was the element area projected into the vertical plane [147]:

$$dA_{xs} = |\sin\beta|dA_s. \quad (53)$$

The effective stresses per unit depth calculated from these depth-only force models using flat plate approximation were then:

$$\begin{cases} \alpha_z^{|z|}(\beta, \gamma) = \alpha_z(0, \text{sgn}(\dot{z})\pi/2)|\cos\beta| \\ \alpha_x^{|z|}(\beta, \gamma) = \alpha_x(\pi/2, 0)|\sin\beta| \end{cases} \quad (54)$$

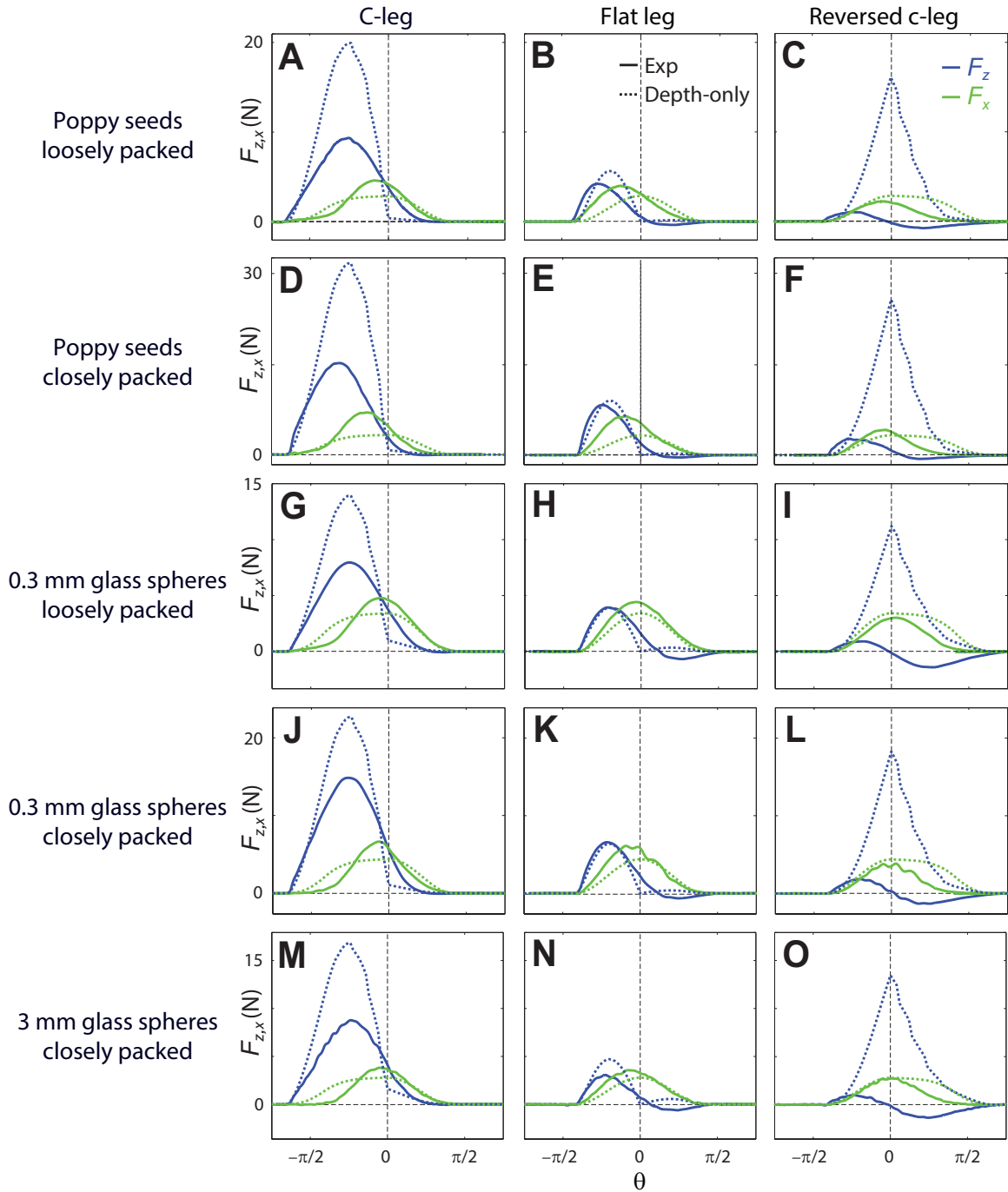


Figure 54: Net lift F_z (blue) and thrust F_x (green) versus leg angle θ on the three model legs for all media tested. Solid curves: experimental measurements. Dotted curves: predictions from the depth-only force models. See Figure 3 A to C for schematic of the experiment and definition of variables.

Comparing the $\alpha_{z,x}^{|\beta|}(\beta, \gamma)$ calculated using Equation 54 (Figure 53) to our resistive force measurements $\alpha_{z,x}(\beta, \gamma)$ (Figure 2, C and D) for loosely packed poppy seeds, we found that these depth-only force models did not capture most of the measured stress profiles. In particular, the depth-only vertical penetration force model over-predicted $\alpha_z(\beta, \gamma)$ for all β and γ except when the plate was horizontal ($\beta = 0$) and moving vertically ($\gamma = \pm\pi/2$). Contrary to experimental measurements, the $\alpha_{z,x}^{|\beta|}$ calculated from the depth-only models were symmetric to $\beta = 0$ (horizontal orientation), and $\alpha_z^{|\beta|}$ (or $\alpha_x^{|\beta|}$) was always opposing the plate’s vertical (or horizontal) velocity (the shaded regions shrank to a line).

We used these depth-only force models to calculate the net lift F_z and thrust F_x versus leg angle θ for the three model legs rotated through all media tested, by the integration of stresses over the legs (Equation 7) using $\alpha_{z,x}^{|\beta|}(\beta, \gamma)$. We found that they not only significantly over-predicted peak F_z (by up to 1400%) but also erroneously predicted similar peak $F_{z,x}$ for the c-leg and reversed c-leg (Figure 54).

A.2 Generality of resistive force model for a variety of granular media

Table 3: Physical properties of the three granular media (in different compactions) for which resistive forces were measured. *Angle of repose for 3 mm glass spheres courtesy of Sarah Sharpe.

Granular medium	Particle diameter (mm)	Particle material density (g/cm ³)	Compaction	Volume fraction	Angle of repose (°)
poppy seeds	0.7 ± 0.2	1.1	LP	0.58	36
			CP	0.62	47
0.3 mm glass spheres	0.27 ± 0.04	2.5	LP	0.58	25
			CP	0.62	35
3 mm glass spheres	3.2 ± 0.2	2.6	CP	0.63	21*

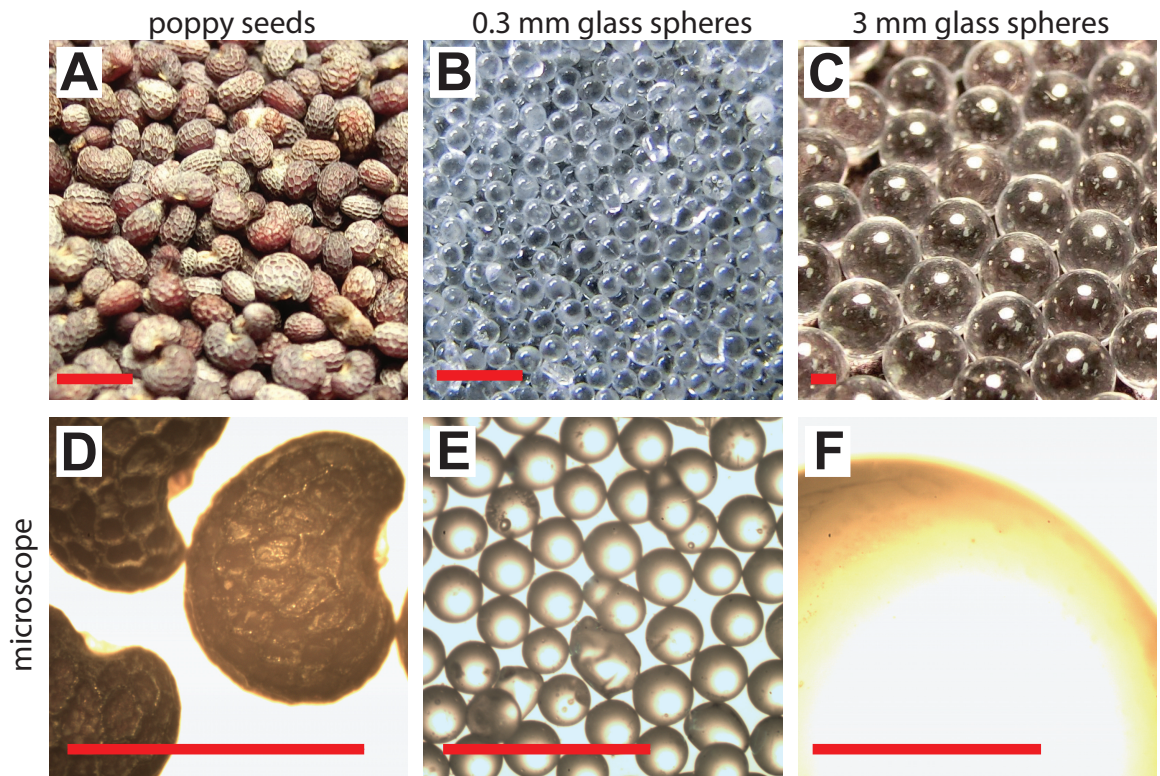


Figure 55: The three granular media tested in our study. Top: regular images. Bottom: microscope images. The length of each scale bar is 1 mm. Photo credit of (A) and (C): Sarah Sharpe.

To test the generality of our resistive force model and provide a database for future studies, we performed resistive force measurements for three granular media—poppy seeds, 0.3 mm glass spheres, and 3 m glass spheres (Figure 55), which have different particle size, shape, density, and friction (measured by angle of repose) (Table 3). We prepared these granular media into well-defined compactions which affected stresses [135, 87]. We prepared poppy seeds and 0.3 mm glass spheres into both a loosely packed (LP) and a closely packed (CP) states, and prepared 3 m glass spheres into a closely packed (CP) state (Table 3).

Despite differences in magnitudes and fine features, we observed similar profiles of the vertical and horizontal stresses per unit depth $\alpha_{z,x}(\beta, \gamma)$ for all media tested (Figure 56). Our resistive force model predicted the net lift F_z and thrust F_x versus leg angle θ on the three model legs rotated through granular media (Figure 57). Compared with predictions from the depth-only force models (Figure 53), our resistive force model had a significant improvement in accuracy.

A.3 Scaling routine for easy use of the resistive force model

To provide a means for practical use of our resistive force model and comparison with new theories of dense granular flow [119], we performed a fitting approximation to the stress per unit depth data $\alpha_{z,x}$ for all media tested, and developed a scaling routine based on the data fits.

We first performed a discrete Fourier transform of the $\alpha_{z,x}(\beta, \gamma)$ data (Figure 56) over $-\pi/2 \leq \beta \leq \pi/2$ and $-\pi \leq \gamma \leq \pi$ to obtain a fitting function. We examined the Fourier coefficients and found that the $\alpha_{z,x}(\beta, \gamma)$ data of all media tested could be well approximated by the following fits:

$$\begin{cases} \alpha_z^{\text{fit}}(\beta, \gamma) = \sum_{m=-1}^1 \sum_{n=0}^1 [A_{m,n} \cos 2\pi(\frac{m\beta}{\pi} + \frac{n\gamma}{2\pi}) + B_{m,n} \sin 2\pi(\frac{m\beta}{\pi} + \frac{n\gamma}{2\pi})] \\ \alpha_x^{\text{fit}}(\beta, \gamma) = \sum_{m=-1}^1 \sum_{n=0}^1 [C_{m,n} \cos 2\pi(\frac{m\beta}{\pi} + \frac{n\gamma}{2\pi}) + D_{m,n} \sin 2\pi(\frac{m\beta}{\pi} + \frac{n\gamma}{2\pi})] \end{cases} \quad (55)$$

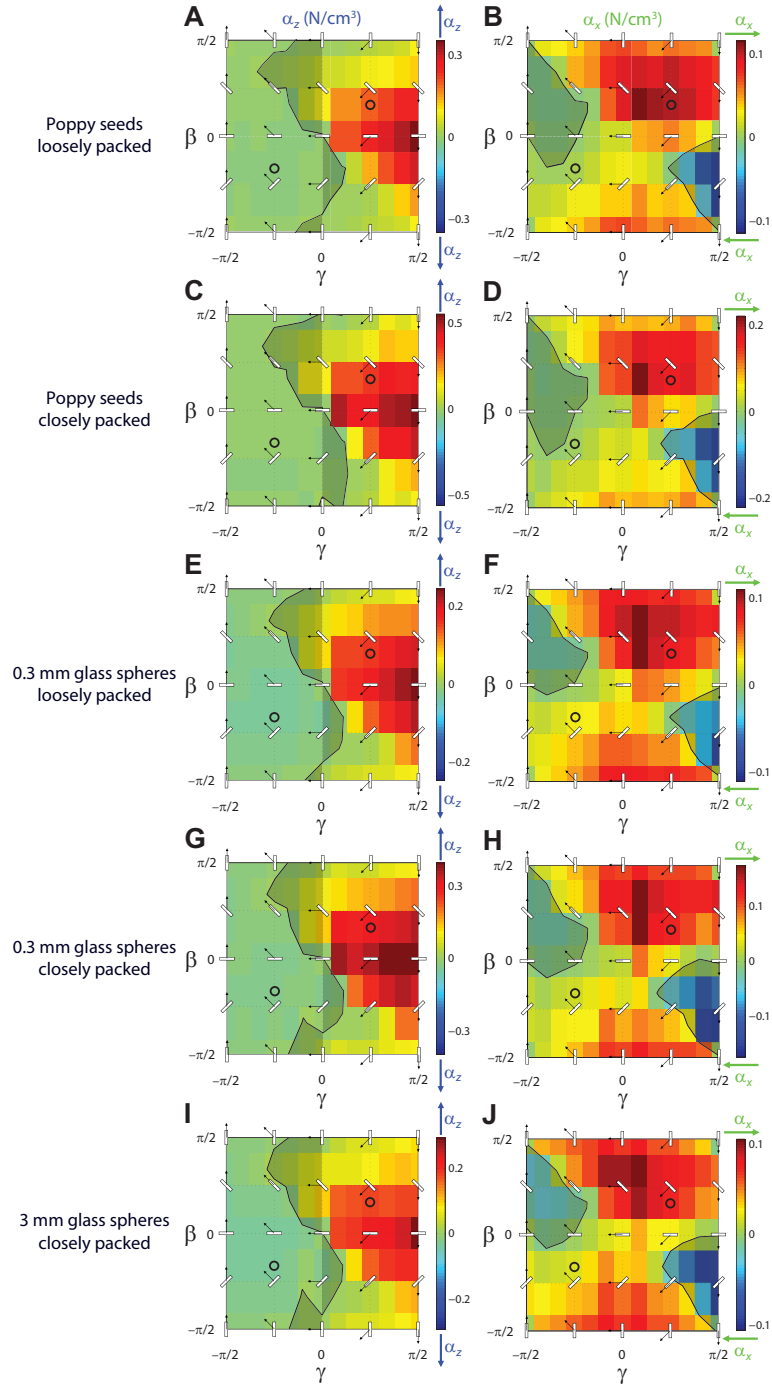


Figure 56: Vertical ($\alpha_z^{|z|}(\beta, \gamma)$, left) and horizontal ($\alpha_{z,x}^{|z|}(\beta, \gamma)$, right) stresses per unit depth as a function of attack angle β and intrusion angle γ for all media tested. (A) and (B) are reproduced from Figure 22, B and C. See Figure 21 for schematic of the experiment and definition of variables.

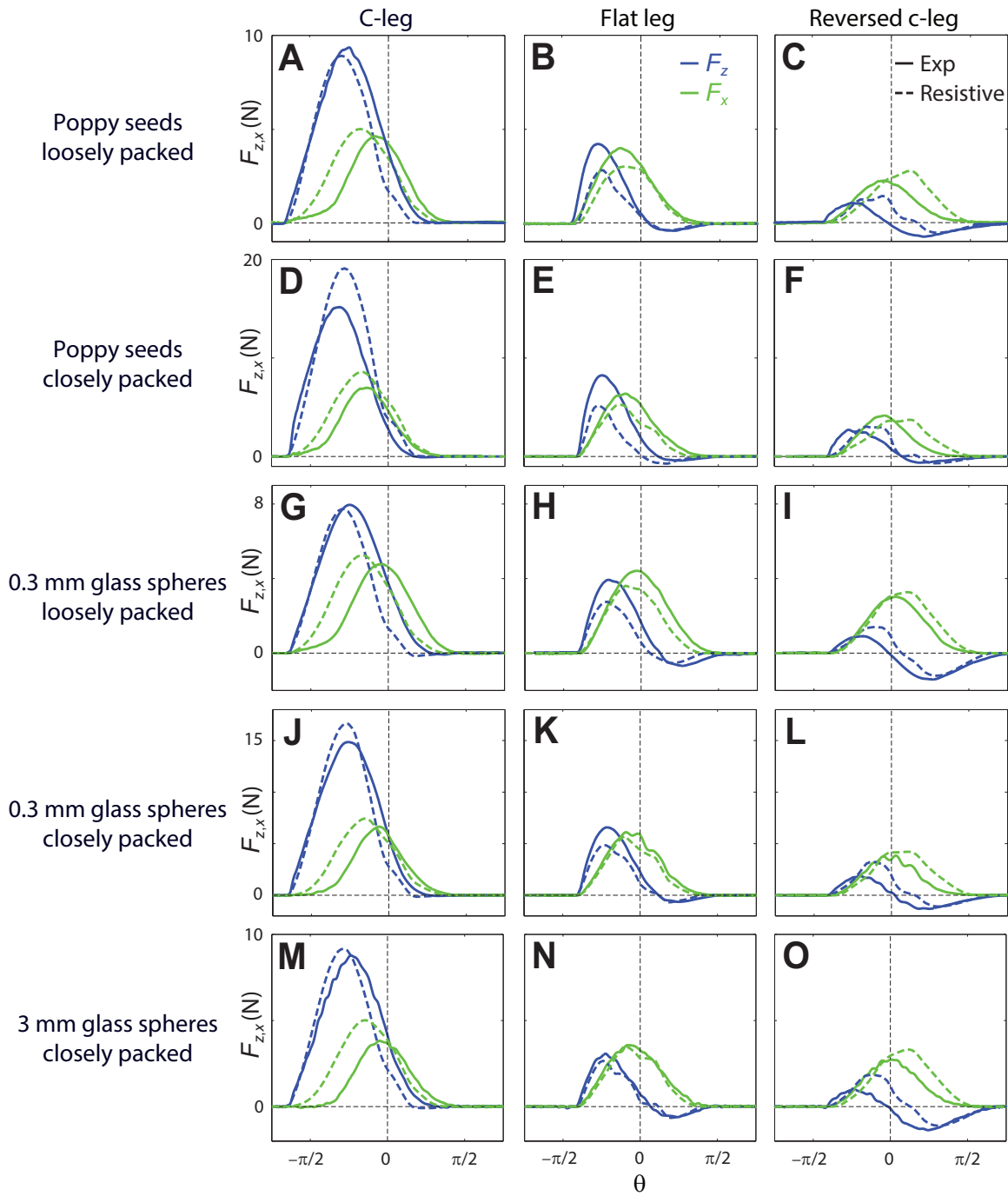


Figure 57: Net lift F_z (blue) and thrust F_x (green) versus leg angle θ on the three model legs for all media tested. Solid curves: experimental measurements. Dashed curves: resistive force model predictions. (A) to (C) are reproduced from Figure 3, D to F. See Figure 21 for schematic of the experiment and definition of variables.

using nine zeroth- and first-order terms (whose magnitudes are larger than $0.05 A_{0,0}$) (Table 4):

$$M = \left(A_{0,0} \quad A_{1,0} \quad B_{1,1} \quad B_{0,1} \quad B_{-1,1} \quad C_{1,1} \quad C_{0,1} \quad C_{-1,1} \quad D_{1,0} \right)^T \quad (56)$$

Table 4: Zeroth- and first-order Fourier coefficients M (in N/cm^3) for all media tested. These coefficients are $0.05 A_{0,0}$. M_0 is a generic coefficient curve to which the M for each granular medium can be collapsed onto by division of a scaling factor ζ ($\zeta = 1$ for M_0). We choose the magnitudes of M_0 such that for all media tested the values of ζ are nearly the same as the values of $\alpha_z^{\text{fit}}(0, \pi/2)$ (this becomes useful later in the scaling routine). CP and LP indicates closely packed and loosely packed states.

granular medium	poppy seeds		0.3 mm glass spheres		3 mm glass spheres	generic coefficients
compaction	LP	CP	LP	CP	CP	n/a
matrix notation	M_{poppyLP}	M_{poppyCP}	$M_{0.3\text{mmLP}}$	$M_{0.3\text{mmCP}}$	$M_{3\text{mmCP}}$	M_0
$A_{0,0}$	0.051	0.094	0.040	0.081	0.045	0.206
$A_{1,0}$	0.047	0.092	0.030	0.063	0.031	0.169
$B_{1,1}$	0.053	0.092	0.045	0.078	0.046	0.212
$B_{0,1}$	0.083	0.151	0.077	0.133	0.084	0.358
$B_{-1,1}$	0.020	0.035	0	0.024	0.012	0.055
$C_{1,1}$	-0.026	-0.039	-0.031	-0.050	-0.031	-0.124
$C_{0,1}$	0.057	0.086	0.066	0.087	0.060	0.253
$C_{-1,1}$	0	0.018	0	0	0	0.007
$D_{1,0}$	0.025	0.046	0.017	0.033	0.015	0.088
scaling factor ζ	0.248	0.488	0.194	0.371	0.214	1

By symmetry, $\alpha_z(\beta \leq 0, \pi/2) = \alpha_z(\beta \geq 0, \pi/2)$, and $\alpha_x(\beta \leq 0, \pi/2) = -\alpha_x(\beta \geq 0, \pi/2)$. However, the data slightly deviated from this equality because the initial positions of the plate were close to one of the boundaries of the container. Therefore, before the Fourier transform, we averaged the raw data for $\gamma = \pm\pi/2$ to restore symmetry by $\alpha_z(\beta \leq 0, \pi/2) = \alpha_z(\beta \geq 0, \pi/2) = \frac{1}{2}[\alpha_z(\beta \leq 0, \pi/2) + \alpha_z(\beta \geq 0, \pi/2)]$. The raw data were also not uniformly sampled in the γ direction; we found that this only resulted in small errors in data fitting.

We found that for all media tested (denoted by $i = \text{poppyLP}, \text{poppyCP}, 0.3\text{mmLP}, 0.3\text{mmCP}, \text{and } 3\text{mmCP}$), the Fourier coefficients M_i could be collapsed onto a generic coefficient curve, M_0 , by dividing M_i by a scaling factor ζ_i (Table 4, Figure 58):

$$M_i/\zeta_i \approx M_0 \quad (57)$$

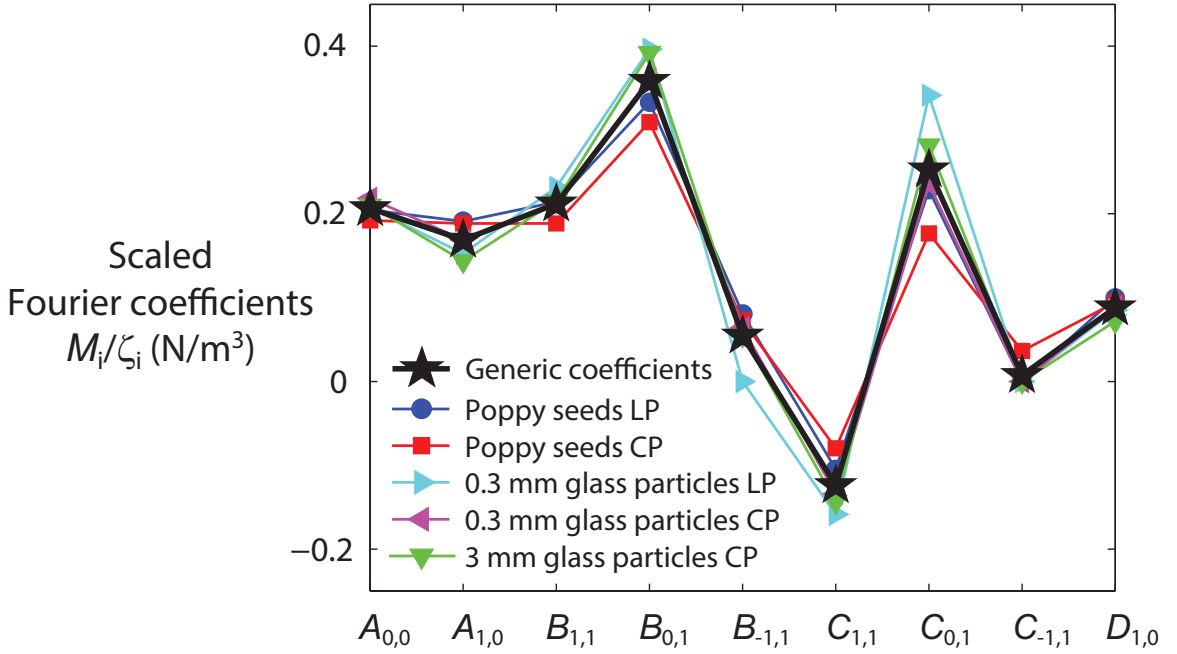


Figure 58: Scaled Fourier coefficients M_i/ζ_i of all media tested (thin colored curves) can be approximated by a generic coefficient curve M_0 (thick black curve).

This enabled us to scale stresses per unit depth ($\alpha_{z,x}$) and thus forces ($f_{z,x}$ and $F_{z,x}$) for all media tested. By Equation 55, using the generic coefficient curve M_0 ($\zeta = 1$) from Table 4, we calculated generic stress (per unit depth) profiles $\alpha_{z,x}^{\text{generic}}(\beta, \gamma)$ (Figure 59). We found that, by multiplication by the scaling factor ζ , these generic stress profiles well approximated the measured $\alpha_{z,x}(\beta, \gamma)$ (Figure 56) for all media tested:

$$\alpha_{z,x}(\beta, \gamma) \approx \zeta \alpha_{z,x}^{\text{generic}}(\beta, \gamma). \quad (58)$$

Using Equation 7 and $\alpha_{z,x}^{\text{generic}}(\beta, \gamma)$, we calculated the generic force profiles $F_{z,x}^{\text{generic}}(\theta)$ on the three model legs rotated through granular media (Figure 60). We found that

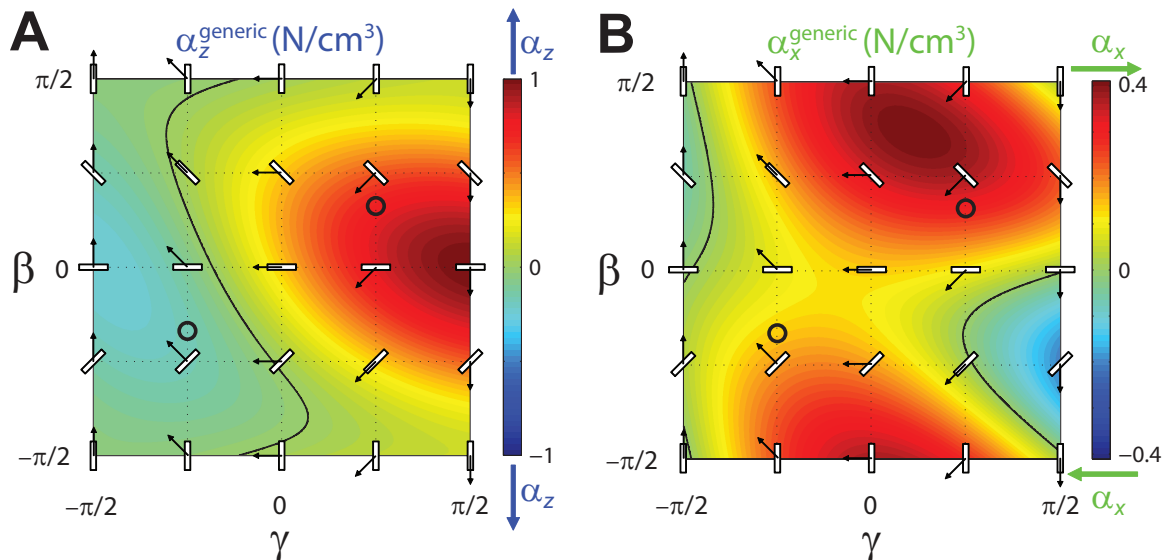


Figure 59: Generic stress (per unit depth) profiles $\alpha_{z,x}^{\text{generic}}(\beta, \gamma)$ for all media tested. See Figure 2, A and B for schematic of the experiment and definition of variables.

in all media tested and for both the c-leg and the flat leg, these generic force profiles captured the measured $F_{z,x}$ scaled by the scaling factors ζ :

$$F_{z,x}^{\text{generic}}(\theta) \approx F_{z,x}(\theta)/\zeta. \quad (59)$$

However, the agreement was worse for the reversed c-leg. Our resistive force model revealed that this was because by using $F_{z,x}^{\text{generic}}(\theta)$, stresses were significantly overestimated for the reversed c-leg's elements that reached large depths.

We further observed that the ratio of the maximal vertical stress (which occurred on a horizontal plate moving downward) between the measurements ($\alpha_z(0, \pi/2)$) and fits ($\alpha_z^{\text{fit}}(0, \pi/2)$) was similar for all media tested (Table 5):

$$\chi = \alpha_z(0, \pi/2)/\alpha_z^{\text{fit}}(0, \pi/2) = 1.26 \pm 0.14, \quad (60)$$

where χ is in mean \pm s.d.

Therefore, we propose that for a sufficiently level and uniform dry granular medium composed of near-monodispersed, near-spherical, rounded particles of ~ 0.1 to ~ 1 mm in diameter, one can simply measure its maximal vertical stress $\alpha_z(0, \pi/2)$ by

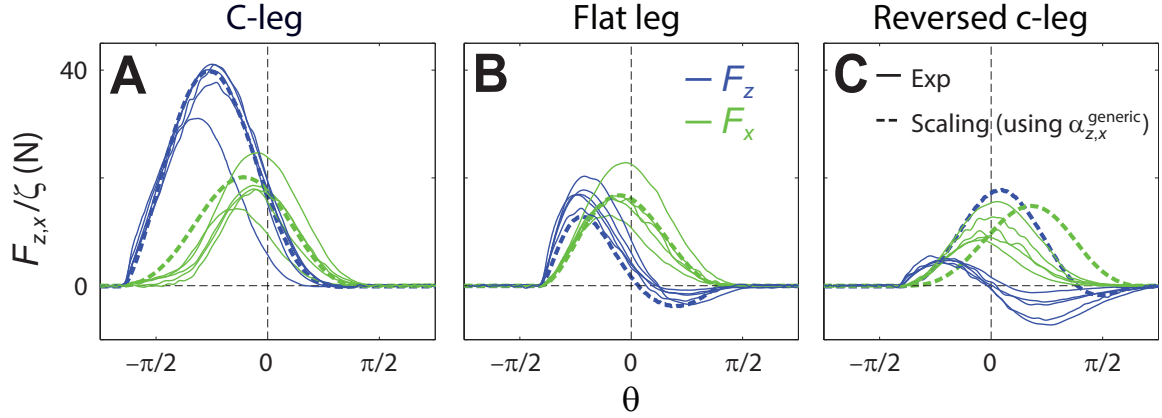


Figure 60: The measured net forces scaled by the measured scaling factors $F_{z,x}(\theta)/\zeta$ for all media tested (thin curves), in comparison with the generic profiles of net forces $F_{z,x}^{\text{generic}}(\theta)$ (thick curves) calculated from the generic stress profiles $\alpha_{z,x}^{\text{generic}}$ (Figure 59). See Figure 3 A to C for schematic of the experiment and definition of variables.

Table 5: Comparison of the measurements and fits of maximal vertical stress per unit depth (in N/cm^3) for all media tested. CP and LP indicates closely packed and loosely packed states. $\chi = \alpha_z(0, \pi/2)/\alpha_z^{\text{fit}}(0, \pi/2)$.

Granular medium	poppy seeds		0.3 mm glass spheres		3 mm glass spheres
	LP	CP	LP	CP	CP
$\alpha_z(0, \pi/2)$	0.35	0.56	0.24	0.40	0.29
$\alpha_z^{\text{fit}}(0, \pi/2)$	0.26	0.47	0.19	0.38	0.22
χ	1.37	1.19	1.27	1.05	1.33

pushing a horizontal plate downward to infer the maximal value of the fit vertical stress $\alpha_z^{\text{fit}}(0, \pi/2)$:

$$\alpha_z^{\text{fit}}(0, \pi/2) = \alpha_z(0, \pi/2)/\chi \approx 0.8\alpha_z(0, \pi/2). \quad (61)$$

The value of $\alpha_z^{\text{fit}}(0, \pi/2)$ in N/m^3 then gives the scaling factor ζ for this granular medium, because we choose the magnitudes of the generic curve M_0 so that the values of ζ and $\alpha_z^{\text{fit}}(0, \pi/2)$ are nearly the same for all media tested:

$$\zeta \approx \alpha_{z,x}^{\text{fit}}(\beta, \gamma). \quad (62)$$

Note that this equation only equates the numeric values on both sides, because ζ is dimensionless. Then, from Equation 58, by scaling the generic stress profiles $\alpha_{z,x}^{\text{generic}}$ (Figure 59) by the determined scaling factor ζ , we can obtain an approximation of stress profiles for this granular medium:

$$\alpha_{z,x}(\beta, \gamma) \approx \alpha_{z,x}^{\text{scaled}}(\beta, \gamma) = \zeta \alpha_{z,x}^{\text{generic}}(\beta, \gamma). \quad (63)$$

This scaling routine provides an alternative to measuring $\alpha_{z,x}$ for all β and γ (at the cost of model accuracy). As demonstrated by the model leg rotation experiments (Figure 60) and robot locomotion experiments (see Figure 65 in the next section), our scaling routine only suffers a small loss in accuracy for much of the leg morphology and stride frequencies tested. This technique can be particularly useful in a field setting, because only a single force measurement is needed. We summarize these practical steps to use our resistive force model in Figure 61.

A.4 Applicability of resistive force model to natural sands

To test the predictive power of our resistive force model for natural sands, we chose two natural sands of higher polydispersity and angularity than those of the granular media tested, and examined whether the scaling routine (Figure 61) could predict the net forces $F_{z,x}(\theta)$ on the three model legs during rotation through the natural sands.

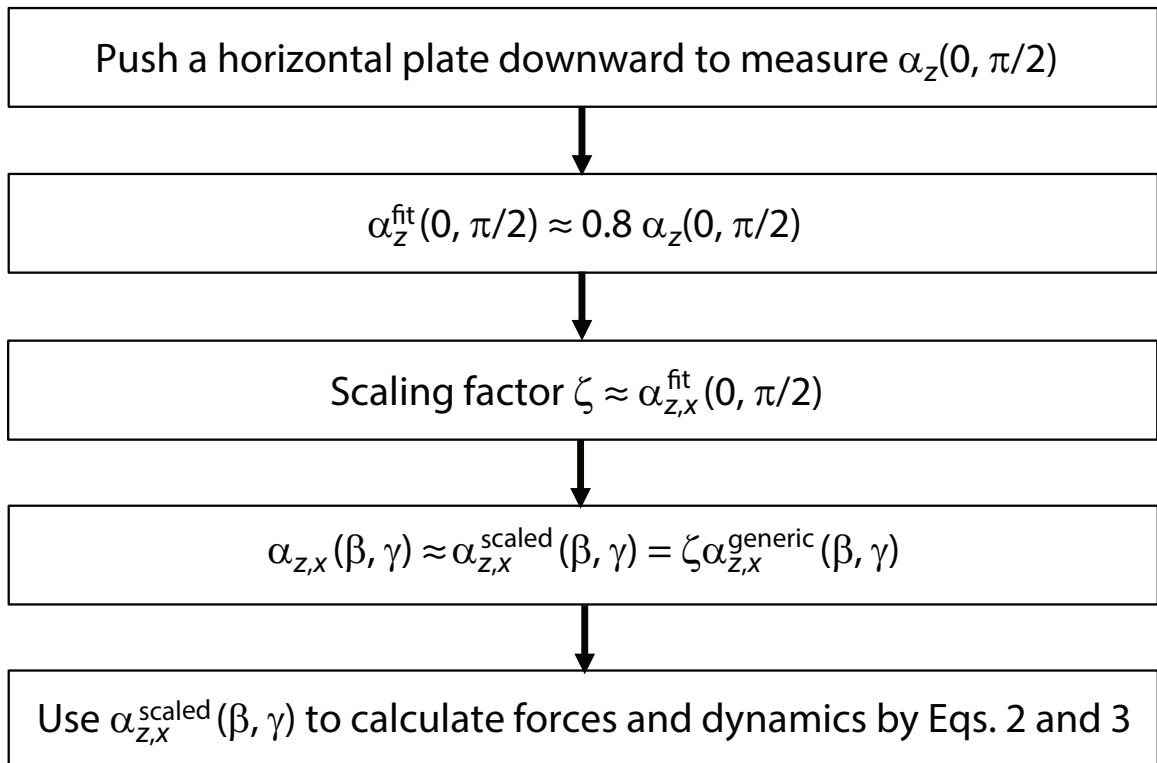


Figure 61: A scaling routine to easily apply our resistive force model.

The two natural sands, referred to as “Yuma sand” and “29 Palms sand” (Table 6, Figure 62), were collected from the Mojave Desert in the southwest United States, one from Yuma, Arizona and the other from 29 Palms, California. The Yuma sand had most particles (70% by mass) in the 0.06–0.3 mm particle size range, and the 29 Palms sand had most particles (91% by mass) in the 0.3–3 mm particle size range. Both natural sands were fluidized by the fluidized bed before each force measurement was performed. We further tested modified 29 Palms sand with reduced polydispersity to examine the effect of polydispersity on model accuracy.

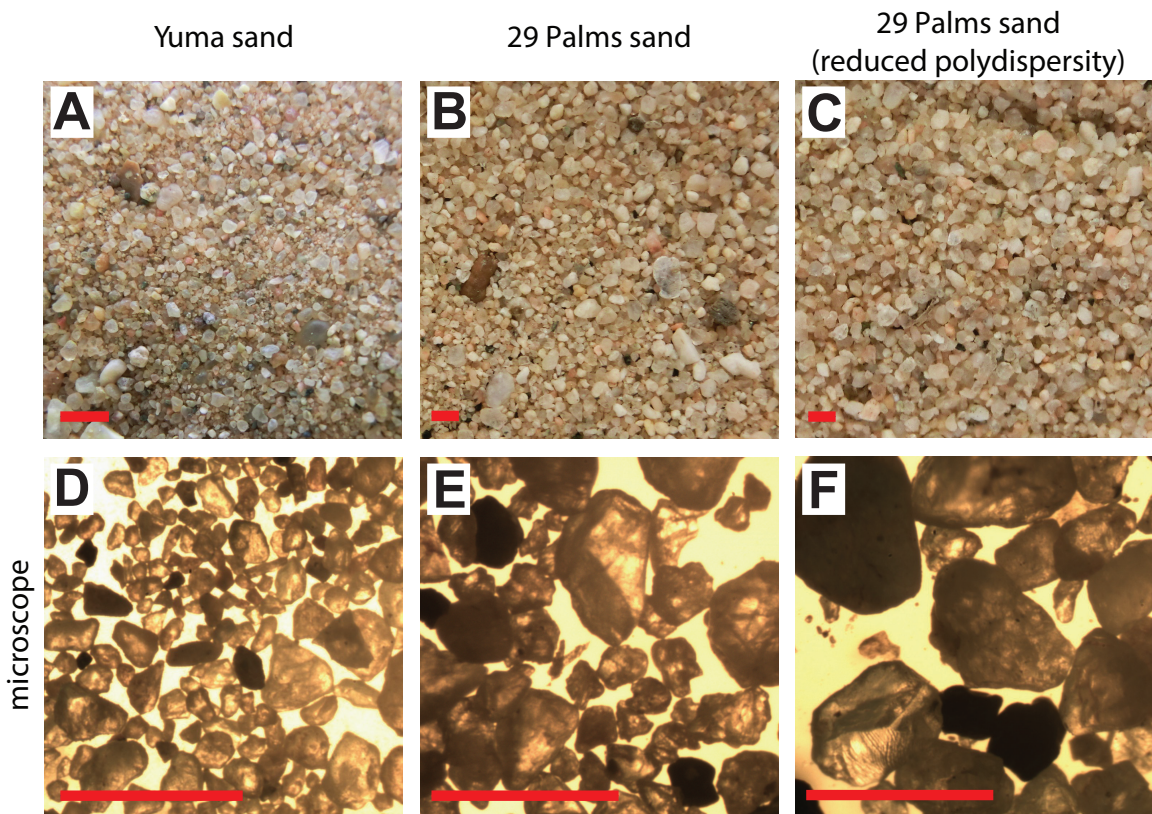


Figure 62: The natural sands used to test the predictive power of our scaling routine. Top: regular images. Bottom: microscope images. The length of each scale bar is 1 mm.

During downward penetration ($\gamma = \pi/2$) into both the Yuma and 29 Palms sands, the vertical stress σ_z on a horizontal plate ($\beta = 0$) increased nearly proportionally to

Table 6: Particle size distribution of the natural sands tested.

natural sand	particle diameter (mm)	mass percentage (%)
Yuma sand	< 0.06	2
	0.06–0.3	68
	0.3–3.0	17
	>3.0	13
29 Palms sand	< 0.3	5
	0.3–0.6	36
	0.6–0.7	55
	0.7–3.0	3
	>3.0	1
29 Palms sand with reduced polydispersity	0.6–0.7	100

depth $|z|$ at low enough depths (Figure 63, solid curves), similar to observations in the granular media tested. However, for both the natural sands, σ_z versus $|z|$ displayed nonlinearity as depth further increased sooner than observed for the granular media tested. This was because both natural sands had larger internal stresses (larger $\alpha_{z,x}$ magnitudes) and likely suffered boundary effects at much shallower depths as compared to the granular media tested. In addition, for the Yuma sand which had more particles in the 0.06–0.3 mm particle size range, this nonlinearity due to boundary effects was more pronounced. Therefore, to minimize possible errors from boundary effects, we perform linear fits with zero intercept to the σ_z versus $|z|$ data (Figure 63, dashed curves) over the linear regime (0–2 cm for the Yuma sand; 0–3 cm for the 29 Palms sand) to obtain $\alpha_z(0, \pi/2)$ (slopes of dashed lines) for both the natural sands. This gave us their scaling factors ζ and estimates of their stress profiles from $\alpha_{z,x}^{\text{scaled}}(\beta, \gamma) = \zeta \alpha_{z,x}^{\text{generic}}(\beta, \gamma)$ (Equation 63).

For the three model legs rotated through both the Yuma and 29 Palms sands, both the net lift F_z and thrust F_x versus leg angle θ displayed asymmetric profiles similar to those observed for the granular media tested (Figure 64, solid curves). Using the $\alpha_z(0, \pi/2)$ obtained from the vertical penetration experiment (Figure 63),

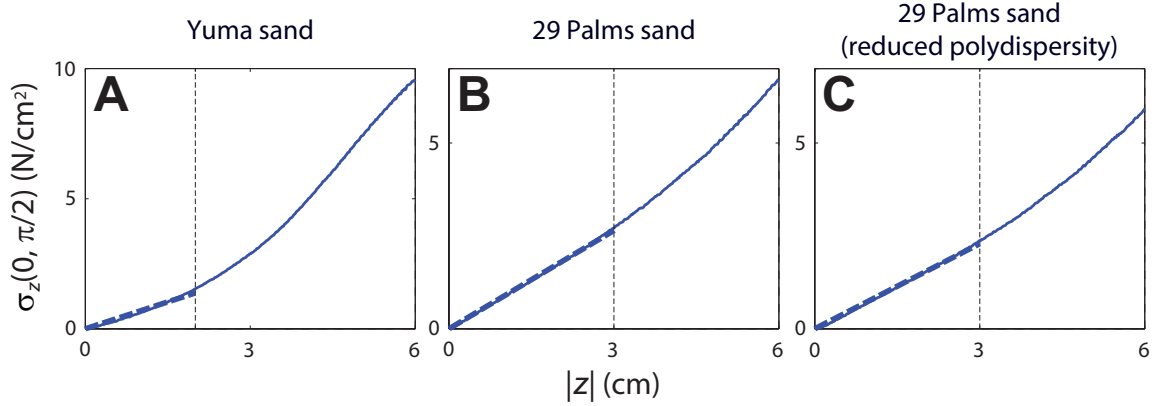


Figure 63: Maximal vertical stress $\sigma_z(0, \pi/2)$ versus depth $|z|$ measured in the natural sands using a plate element horizontally oriented and penetrating vertically downward ($\beta = 0, \gamma = \pi/2$). Dashed lines are linear fits with zero intercept to the data in the linear regime at shallow depths. See Figure 21 for schematic of the experiment and definition of variables.

our scaling routine significantly overpredicted $F_{z,x}(\theta)$ on the c-leg for both the Yuma and 29 Palms sands (both by 35%). Nevertheless, the shape of model predictions were similar to experimental observations (Figure 64, dashed curves). The model accuracy was best for the flat leg, and worst for the reversed c-leg.

There are two major differences between the natural sands and the granular media tested: The natural sands have higher polydispersity, and are also less spherical and more angular. To probe where the overprediction (of forces on the c-leg) stemmed from, we further tested the 29 Palms sand with reduced polydispersity (obtained by sieving the sand to obtain only the 0.6–0.7 mm particles). We found that while both $\alpha_z(0, \pi/2)$ and $F_{z,x}(\theta)$ dropped by 14% (figs. 63 and 64), the model overprediction of forces on the c-leg remained the same (35%). This suggested that the non-spherical and angular shape of the natural sand particles, rather than their higher polydispersity, was likely the cause of the model overprediction.

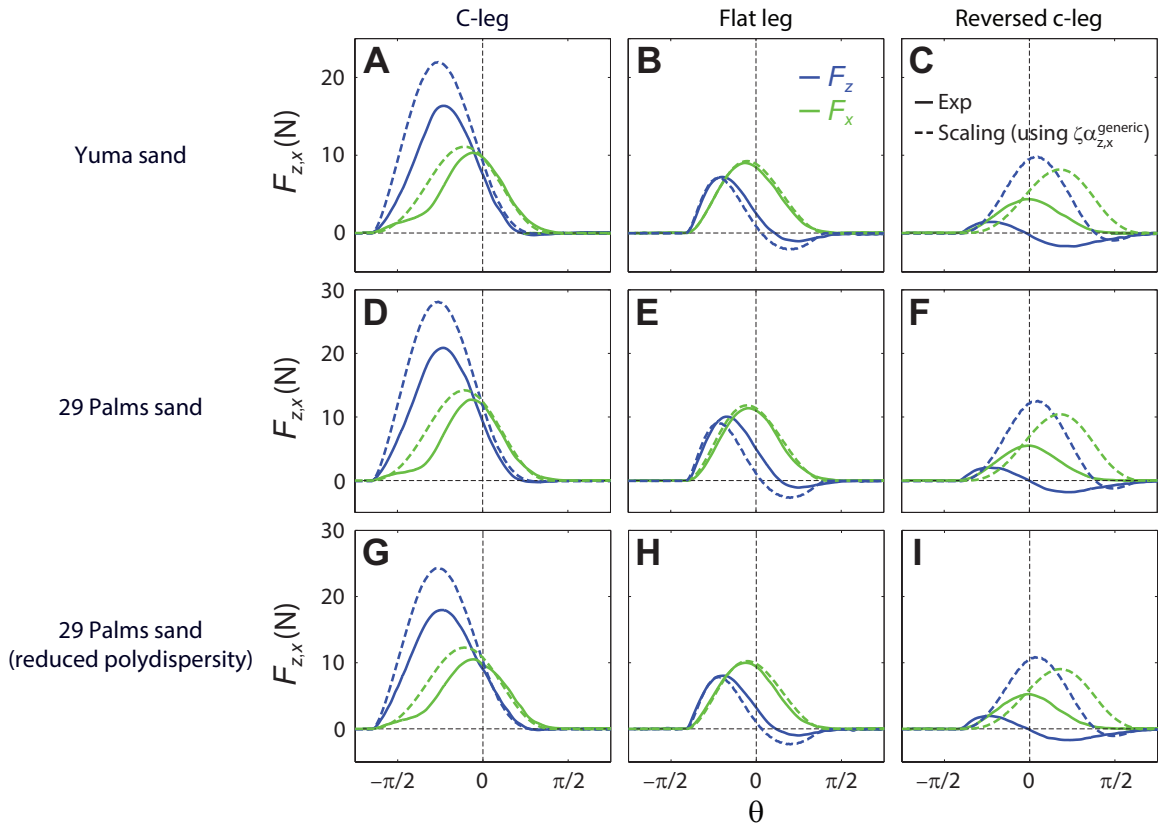


Figure 64: Net lift F_z (blue) and thrust F_x (green) versus leg angle θ on the three model legs for the natural sands tested. Solid curves: experimental measurements. Dashed curves: resistive force model predictions using the scaling routine (Figure 61). See Figure 21 for schematic of the experiment and definition of variables.

A.5 Comparison of model accuracy in predicting legged locomotion

To evaluate the accuracy of our scaling routine in predicting legged locomotion, we used our multibody dynamic simulation to simulate the robot’s movement on loosely packed poppy seeds using the scaled generic stress profiles ($\alpha_{z,x}^{\text{scaled}} = \zeta\alpha_{z,x}^{\text{generic}}$). We calculated the robot’s average forward speed \bar{v}_x versus stride frequency f and leg curvature $1/r$ (Figure 65), and compare it with experimental measurements and resistive force model predictions (without using the scaling routine). As a comparison, we also calculated $\bar{v}_x(f, 1/r)$ using $\alpha_{z,x}^{|z|}$ obtained from the depth-only force models (Figure 53).

We found that the simulation using scaled generic stress profiles ($\zeta\alpha_{z,x}^{\text{generic}}$) only suffered a small loss in accuracy as compared to that using the measured $\alpha_{z,x}$. By contrast, the simulation using stresses $\alpha_{z,x}^{|z|}$ from the depth-only force models suffered a larger loss in accuracy (by up to 150% error), and in particular, erroneously predicted that the robot moved at similar speeds using both c-legs and reversed c-legs.

In addition to the predictions locomotor kinematics, our resistive force model and multibody dynamic simulation also allowed us to calculate ground reaction forces (Figure 66) during locomotion on granular media (which would be otherwise difficult to measure), in a similar fashion as calculations of lift, drag, thrust, traction, and resistance in studies of vehicle mobility in fluids and terramechanics studies. Notice the larger vertical ground reaction forces produced by the C-legs relative to those by the reversed c-legs. This allowed the robot to maintain higher lift above the granular medium, reducing drag on the belly.

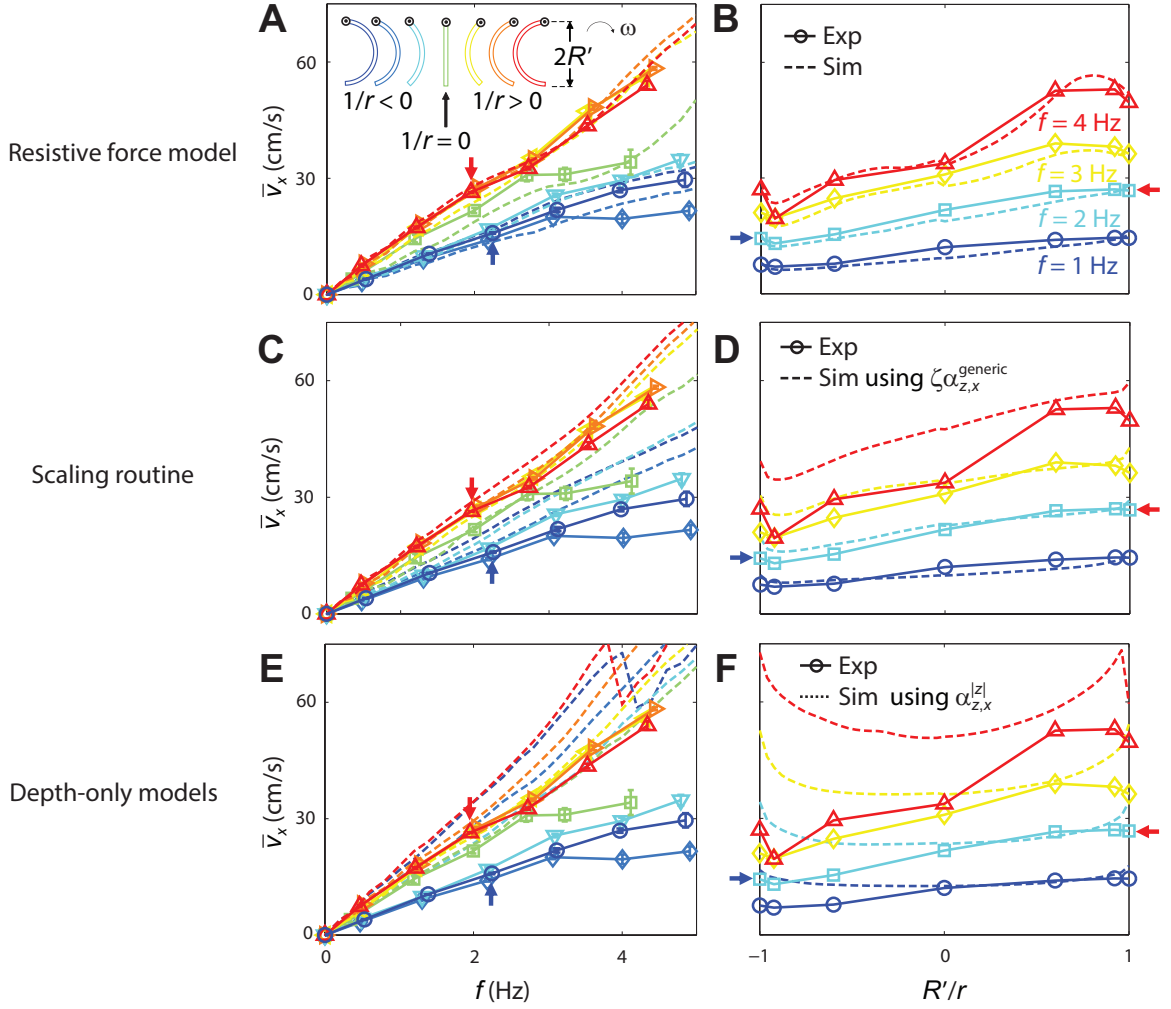


Figure 65: Average forward speed \bar{v}_x of the robot as a function of stride frequency f (left) and leg curvature $1/r$ (right) on loosely packed poppy seeds. Solid curves: experimental measurements. Dashed curves: simulation predictions. Top: using the measured stresses ($\alpha_{z,x}$). Middle: using the scaled generic stress profiles ($\alpha_{z,x}^{\text{scaled}} = \zeta_5 \alpha_{z,x}^{\text{generic}}$). Bottom: using stresses from the depth-only force models ($\alpha_{z,x}^{|z|}$). The drop of \bar{v}_x vs. f at near $R'/r = 1$ using $\alpha_{z,x}^{|z|}$ was due to pitch instability of the robot in simulation (the robot became upside down). (A) and (B) are reproduced from Figure 23, C and D.

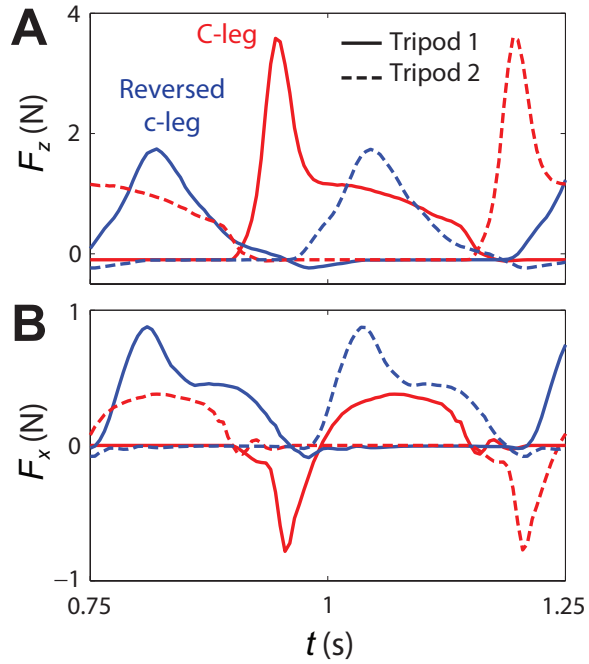


Figure 66: Vertical (F_z , top) and horizontal (F_x , bottom) ground reaction forces versus time t on both tripods of the robot during locomotion on loosely packed poppy seeds, calculated from the simulation using the resistive force model. Solid and dashed curves correspond to forces on the two tripods of legs, respectively. Results are for the two representative runs shown in Figure 23B. Note that these ground reaction forces do not include those on the robot body (which were also calculated but not plotted here).

REFERENCES

- [1] AGUILAR, J. and GOLDMAN, D. I., “Robophysical study of jumping dynamics on granular media,” *Nature Physics*, 2015.
- [2] AGUILAR, J. and GOLDMAN, D. I., “Robophysical study of jumping dynamics on granular media,” *Nature Physics*, 2015.
- [3] AGUILAR, J., ZHANG, T., QIAN, F., KINGSBURY, M., MCINROE, B., MAZOUCHOVA, N., LI, C., MALADEN, R., GONG, C., TRAVERS, M., and OTHERS, “A review on locomotion robophysics: the study of movement at the intersection of robotics, soft matter and dynamical systems,” *arXiv preprint arXiv:1602.04712*, 2016.
- [4] AHN, A. N., MEIJER, K., and FULL, R. J., “In situ muscle power differs without varying in vitro mechanical properties in two insect leg muscles innervated by the same motor neuron,” *Journal of Experimental Biology*, vol. 209, no. 17, pp. 3370–3382, 2006.
- [5] AHN, A. N., MONTI, R., and BIEWENER, A. A., “In vivo and in vitro heterogeneity of segment length changes in the semimembranosus muscle of the toad,” *The Journal of physiology*, vol. 549, no. 3, pp. 877–888, 2003.
- [6] ALBERT, I., TEGZES, P., ALBERT, R., SAMPLE, J., BARABÁSI, A.-L., VICSEK, T., KAHNG, B., and SCHIFFER, P., “Stick-slip fluctuations in granular drag,” *Physical Review E*, vol. 64, no. 3, p. 031307, 2001.
- [7] ALBERT, R., PFEIFER, M., BARABÁSI, A.-L., and SCHIFFER, P., “Slow drag in a granular medium,” *Physical review letters*, vol. 82, no. 1, p. 205, 1999.
- [8] ALEXANDER, R. M., *Principles of animal locomotion*. Princeton University Press, 2003.
- [9] ANAND, A., CURTIS, J. S., WASSGREN, C. R., HANCOCK, B. C., and KETTERHAGEN, W. R., “Predicting discharge dynamics from a rectangular hopper using the discrete element method (DEM),” *Chemical Engineering Science*, vol. 63, no. 24, pp. 5821–5830, 2008.
- [10] ANDREOTTI, B., FORTERRE, Y., and POULIQUEN, O., *Granular media: between fluid and solid*. Cambridge University Press, 2013.
- [11] ANGSTMANN, C. and MORRISS, G. P., “An approximate formula for the diffusion coefficient for the periodic Lorentz gas,” *Phys. Lett. A*, vol. 376, pp. 1819–1822, 2012.

- [12] ANITESCU, M. and POTRA, F. A., “A time-stepping method for stiff multi-body dynamics with contact and friction,” *International journal for numerical methods in engineering*, vol. 55, no. 7, pp. 753–784, 2002.
- [13] ANITESCU, M. and TASORA, A., “An iterative approach for cone complementarity problems for nonsmooth dynamics,” *Computational Optimization and Applications*, vol. 47, no. 2, pp. 207–235, 2010.
- [14] ARTUSO, R., “Diffusive dynamics and periodic orbits of dynamic systems,” *Phys. Lett. A*, vol. 160, pp. 528–530, 1991.
- [15] ARTUSO, R., “Recycling deterministic diffusion,” *Physica D*, vol. 76, pp. 1–7, 1994.
- [16] ARTUSO, R. and CVITANOVIĆ, P. in *Chaos: Classical and Quantum*, ch. Deterministic diffusion, Copenhagen: Niels Bohr Inst., 2016.
- [17] ASKARI, H. and KAMRIN, K., “Intrusion in heterogeneous materials: Simple global rules from complex micro-mechanics,” *arXiv preprint arXiv:1510.02966*, 2015.
- [18] ASTLEY, H. C., GONG, C., DAI, J., TRAVERS, M., SERRANO, M. M., VELA, P. A., CHOSET, H., MENDELSON, J. R., HU, D. L., and GOLDMAN, D. I., “Modulation of orthogonal body waves enables high maneuverability in sidewinding locomotion,” *Proceedings of the National Academy of Sciences*, vol. 112, no. 19, pp. 6200–6205, 2015.
- [19] BAGNOLD, R. A., *The physics of blown sand and desert dunes*. Courier Corporation, 2012.
- [20] BARANYAI, A., EVANS, D. J., and COHEN, E. G. D., “Field-dependent conductivity and diffusion in a two-dimensional Lorentz gas,” *J. Stat. Phys.*, vol. 70, pp. 1085–1098, 1993.
- [21] BAUCHAU, O. A., BOTTASSO, C. L., and NIKISHKOV, Y. G., “Modeling rotorcraft dynamics with finite element multibody procedures,” *Mathematical and Computer Modelling*, vol. 33, no. 10, pp. 1113–1137, 2001.
- [22] BAYLY, P., LEWIS, B., RANZ, E., OKAMOTO, R., PLESS, R., and DUTCHER, S., “Propulsive forces on the flagellum during locomotion of *Chlamydomonas reinhardtii*,” *Biophysical journal*, vol. 100, no. 11, pp. 2716–2725, 2011.
- [23] BEKKER, M. G., *Off-the-road locomotion: research and development in terramechanics*. University of Michigan Press Ann Arbor, 1960.
- [24] BENEDICT, M., MATTABONI, M., CHOPRA, I., and MASARATI, P., “Aeroelastic analysis of a micro-air-vehicle-scale cycloidal rotor in hover,” *AIAA journal*, vol. 49, no. 11, pp. 2430–2443, 2011.

- [25] BIEWENER, A. A. and ROBERTS, T. J., “Muscle and tendon contributions to force, work, and elastic energy savings: a comparative perspective,” *Exercise and sport sciences reviews*, vol. 28, no. 3, pp. 99–107, 2000.
- [26] BIRKMEYER, P., PETERSON, K., and FEARING, R. S., “DASH: A dynamic 16g hexapedal robot,” in *Intelligent Robots and Systems, 2009. IROS 2009. IEEE/RSJ International Conference on*, pp. 2683–2689, IEEE, 2009.
- [27] BLEHER, P. M., “Statistical properties of two-dimensional periodic Lorentz gas with infinite horizon,” *J. Stat. Phys.*, vol. 66, pp. 479–497, 1992.
- [28] BLICKHAN, R., “The spring-mass model for running and hopping,” *Journal of biomechanics*, vol. 22, no. 11-12, pp. 1217–1227, 1989.
- [29] BOWEN, R., *Equilibrium States and the Ergodic Theory of Anosov Diffeomorphisms*. New York: Springer, 1975.
- [30] BRAND, L. R., “Variations in salamander trackways resulting from substrate differences,” *Journal of Paleontology*, vol. 70, no. 06, pp. 1004–1010, 1996.
- [31] BRILLIANTOV, N. V. and PÖSCHEL, T., *Kinetic theory of granular gases*. Oxford University Press, 2010.
- [32] BRZINSKI III, T., MAYOR, P., and DURIAN, D., “Depth-dependent resistance of granular media to vertical penetration,” *Physical review letters*, vol. 111, no. 16, p. 168002, 2013.
- [33] BUCHLI, J., KALAKRISHNAN, M., MISTRY, M., PASTOR, P., and SCHAAL, S., “Compliant quadruped locomotion over rough terrain,” in *Intelligent Robots and Systems, 2009. IROS 2009. IEEE/RSJ International Conference on*, pp. 814–820, IEEE, 2009.
- [34] BUNIMOVICH, L. A., “Decay of correlations in dynamical systems with chaotic behavior,” *Sov. Phys. JETP*, vol. 62, pp. 842–852, 1985.
- [35] BUNIMOVICH, L. A. and SINAI, Y. G., “Markov partitions for dispersed billiards,” *Commun. Math. Phys.*, vol. 78, pp. 247–280, 1980. Erratum, *ibid.* **107**, 357 (1986).
- [36] BUNIMOVICH, L. A. and SINAI, Y. G., “Statistical properties of Lorentz gas with periodic configuration of scatterers,” *Commun. Math. Phys.*, vol. 78, pp. 479–497, 1981.
- [37] BUNIMOVICH, L. A., SINAI, Y. G., and CHERNOV, N. I., “Markov partitions for two-dimensional hyperbolic billiards,” *Russ. Math. Surv.*, vol. 45, pp. 105–152, 1990.
- [38] BUXTON, P. A., *Animal life in deserts*. Edward Arnold; London, 1923.

- [39] CAVAGNA, G. A., THYS, H., and ZAMBONI, A., “The sources of external work in level walking and running,” *The Journal of physiology*, vol. 262, no. 3, p. 639, 1976.
- [40] CHAUDHURI, B., MEHROTRA, A., MUZZIO, F. J., and TOMASSONE, M. S., “Cohesive effects in powder mixing in a tumbling blender,” *Powder Technology*, vol. 165, no. 2, pp. 105–114, 2006.
- [41] CHEN, G. and UETA, T., “Yet another chaotic attractor,” *International Journal of Bifurcation and Chaos*, vol. 9, no. 07, pp. 1465–1466, 1999.
- [42] CHENG, J., DAVISON, I., and DEMONT, M., “Dynamics and energetics of scallop locomotion,” *Journal of Experimental Biology*, vol. 199, no. 9, pp. 1931–1946, 1996.
- [43] CHO, G.-C., DODDS, J., and SANTAMARINA, J. C., “Particle shape effects on packing density, stiffness, and strength: natural and crushed sands,” *Journal of Geotechnical and Geoenvironmental Engineering*, vol. 132, no. 5, pp. 591–602, 2006.
- [44] CLARK, A. H., KONDIC, L., and BEHRINGER, R. P., “Particle scale dynamics in granular impact,” *Physical review letters*, vol. 109, no. 23, p. 238302, 2012.
- [45] CLEARY, P. W. and SAWLEY, M. L., “DEM modelling of industrial granular flows: 3D case studies and the effect of particle shape on hopper discharge,” *Applied Mathematical Modelling*, vol. 26, no. 2, pp. 89–111, 2002.
- [46] COTTON, F. A., *Chemical Applications of Group Theory*. New York: Wiley, 3 ed., 2008.
- [47] COWAN, N. J., LEE, J., and FULL, R., “Task-level control of rapid wall following in the American cockroach,” *Journal of Experimental Biology*, vol. 209, no. 9, pp. 1617–1629, 2006.
- [48] CRAGO, P. E., HOUK, J. C., and RYMER, W. Z., “Sampling of total muscle force by tendon organs,” *Journal of neurophysiology*, vol. 47, no. 6, pp. 1069–1083, 1982.
- [49] CRAWFORD, C. S., *Biology of desert invertebrates*. Springer Science & Business Media, 2012.
- [50] CRISTADORO, G., “Fractal diffusion coefficient from dynamical zeta functions,” *Journal of Physics A: Mathematical and General*, vol. 39, no. 10, p. L151, 2006.
- [51] CUNDALL, P. A. and STRACK, O. D., “A discrete numerical model for granular assemblies,” *Geotechnique*, vol. 29, no. 1, pp. 47–65, 1979.
- [52] CVITANOVIĆ, P., ARTUSO, R., MAINIERI, R., TANNER, G., and VATTAY, G., *Chaos: Classical and Quantum*. Copenhagen: Niels Bohr Inst., 2016.

- [53] CVITANOVIĆ, P. and ECKHARDT, B., “Periodic orbit expansions for classical smooth flows,” *J. Phys. A*, vol. 24, p. L237, 1991.
- [54] CVITANOVIĆ, P., ECKMANN, J.-P., and GASPARD, P., “Transport properties of the Lorentz gas in terms of periodic orbits,” *Chaos Solit. Fract.*, vol. 6, pp. 113–120, 1995.
- [55] CVITANOVIĆ, P., GASPARD, P., and SCHREIBER, T., “Investigation of the Lorentz gas in terms of periodic orbits,” *Chaos*, vol. 2, pp. 85–90, 1992.
- [56] CVITANOVIC, P. and PIKOVSKY, A., “Cycle expansion for power spectrum,” *Proc. SPIE*, vol. 2038, pp. 290–298, 1993.
- [57] DALEY, M., FELIX, G., and BIEWENER, A., “Running stability is enhanced by a proximo-distal gradient in joint neuromechanical control,” *Journal of Experimental Biology*, vol. 210, no. 3, pp. 383–394, 2007.
- [58] DARWIN, C., *The formation of vegetable mould, through the action of worms, with observations on their habits*. J. Murray, 1892.
- [59] DETTMANN, C. P., “Diffusion in the Lorentz gas,” *Commun. Theor. Phys*, vol. 62, pp. 521–540, 2014.
- [60] DI RENZO, A. and DI MAIO, F. P., “Comparison of contact-force models for the simulation of collisions in dem-based granular flow codes,” *Chemical engineering science*, vol. 59, no. 3, pp. 525–541, 2004.
- [61] DICKINSON, M. H., FARLEY, C. T., FULL, R. J., KOEHL, M., KRAM, R., and LEHMAN, S., “How animals move: an integrative view,” *Science*, vol. 288, no. 5463, pp. 100–106, 2000.
- [62] DICKINSON, W. W. and WARD, J. D., “Low depositional porosity in eolian sands and sandstones, Namib Desert,” *Journal of Sedimentary Research*, vol. 64, no. 2a, pp. 226–232, 1994.
- [63] DING, Y., GRAVISH, N., and GOLDMAN, D. I., “Drag induced lift in granular media,” *Physical Review Letters*, vol. 106, no. 2, p. 028001, 2011.
- [64] DING, Y., SHARPE, S. S., MASSE, A., and GOLDMAN, D. I., “Mechanics of undulatory swimming in a frictional fluid,” *PLoS Comput Biol*, vol. 8, no. 12, p. e1002810, 2012.
- [65] DING, Y., SHARPE, S. S., WIESENFELD, K., and GOLDMAN, D. I., “Emergence of the advancing neuromechanical phase in a resistive force dominated medium,” *Proceedings of the National Academy of Sciences*, vol. 110, no. 25, pp. 10123–10128, 2013.
- [66] DORGAN, K. M., ARWADE, S. R., and JUMARS, P. A., “Burrowing in marine muds by crack propagation: kinematics and forces,” *Journal of Experimental Biology*, vol. 210, no. 23, pp. 4198–4212, 2007.

- [67] DUDLEY, R., *The biomechanics of insect flight: form, function, evolution*. Princeton University Press, 2002.
- [68] DUNATUNGA, S. and KAMRIN, K., “Continuum modelling and simulation of granular flows through their many phases,” *Journal of Fluid Mechanics*, vol. 779, pp. 483–513, 2015.
- [69] EICH, M., GRIMMINGER, F., and KIRCHNER, F., “A versatile stair-climbing robot for search and rescue applications,” in *Safety, Security and Rescue Robotics, 2008. SSRR 2008. IEEE International Workshop on*, pp. 35–40, IEEE, 2008.
- [70] ERICKSON, J. K., “Living the dream—an overview of the Mars exploration project,” *Robotics & Automation Magazine, IEEE*, vol. 13, no. 2, pp. 12–18, 2006.
- [71] ETKIN, B., *Dynamics of atmospheric flight*. Courier Corporation, 2012.
- [72] EZCURRA, E., *Global deserts outlook*. UNEP/Earthprint, 2006.
- [73] FANCY, S. G. and WHITE, R. G., “Energy expenditures by caribou while cratering in snow,” *The Journal of wildlife management*, pp. 987–993, 1985.
- [74] FULL, R. J., KUBOW, T., SCHMITT, J., HOLMES, P., and KODITSCHKEK, D., “Quantifying dynamic stability and maneuverability in legged locomotion,” *Integrative and comparative biology*, vol. 42, no. 1, pp. 149–157, 2002.
- [75] FUNG, Y.-C., *Biomechanics: mechanical properties of living tissues*. Springer Science & Business Media, 2013.
- [76] GALLAVOTTI, G., “Lectures on the billiard,” in *Dynamical Systems, Theory and Applications* (MOSER, J., ed.), vol. 38 of *Lecture Notes in Physics*, pp. 236–295, Berlin: Springer, 1975.
- [77] GASC, J.-P., CATTART, D., CHASSERAT, C., and CLARAC, F., “Propulsive action of a snake pushing against a single site: its combined analysis,” *Journal of morphology*, vol. 201, no. 3, pp. 315–329, 1989.
- [78] GASC, J.-P. and GANS, C., “Tests on locomotion of the elongate and limbless lizard *Anguis fragilis* (Squamata: Anguinae),” *Copeia*, pp. 1055–1067, 1990.
- [79] GASPARD, P., “Diffusion, effusion, and chaotic scattering: An exactly solvable Liouvillian dynamics,” *J. Stat. Phys.*, vol. 68, pp. 673–747, 1992.
- [80] GASPARD, P. and BARAS, F., “Chaotic scattering and diffusion in the Lorentz gas,” *Phys. Rev. E*, vol. 51, pp. 5332–5352, 1995.
- [81] GASPARD, P. and NICOLIS, G., “Transport properties, Lyapunov exponents, and entropy per unit time,” *Phys. Rev. Lett.*, vol. 65, pp. 1693–1696, 1990.

- [82] GENG, J. and BEHRINGER, R. P., “Slow drag in two-dimensional granular media,” *Physical review E*, vol. 71, no. 1, p. 011302, 2005.
- [83] GHIRINGHELLI, G. L., MASARATI, P., MANTEGAZZA, P., and NIXON, M. W., “Multi-body analysis of a tiltrotor configuration,” *Nonlinear Dynamics*, vol. 19, no. 4, pp. 333–357, 1999.
- [84] GLASHEEN, J., MCMAHON, T., and OTHERS, “A hydrodynamic model of locomotion in the basilisk lizard,” *Nature*, vol. 380, no. 6572, pp. 340–341, 1996.
- [85] GOLDMAN, D. I. and UMBANHOWAR, P., “Scaling and dynamics of sphere and disk impact into granular media,” *Physical Review E*, vol. 77, no. 2, p. 021308, 2008.
- [86] GONG, C., TRAVERS, M. J., ASTLEY, H. C., LI, L., MENDELSON, J. R., GOLDMAN, D. I., and CHOSET, H., “Kinematic gait synthesis for snake robots,” *The International Journal of Robotics Research*, vol. 35, no. 1-3, pp. 100–113, 2016.
- [87] GRAVISH, N., UMBANHOWAR, P. B., and GOLDMAN, D. I., “Force and flow transition in plowed granular media,” *Physical review letters*, vol. 105, no. 12, p. 128301, 2010.
- [88] GRAY, J., “The mechanism of locomotion in snakes,” *Journal of Experimental Biology*, vol. 23, no. 2, pp. 101–120, 1946.
- [89] GRAY, J. and HANCOCK, G., “The propulsion of sea-urchin spermatozoa,” *Journal of Experimental Biology*, vol. 32, no. 4, pp. 802–814, 1955.
- [90] GRAY, J. and LISSMANN, H., “The kinetics of locomotion of the grass-snake,” *Journal of Experimental Biology*, vol. 26, no. 4, pp. 354–367, 1950.
- [91] GUAZZELLI, E. and MORRIS, J. F., *A physical introduction to suspension dynamics*, vol. 45. Cambridge University Press, 2011.
- [92] GUCKENHEIMER, J., “Sensitive dependence to initial conditions for one dimensional maps,” *Communications in Mathematical Physics*, vol. 70, no. 2, pp. 133–160, 1979.
- [93] GUILLARD, F., FORTERRE, Y., and POULIQUEN, O., “Lift forces in granular media,” *Physics of Fluids (1994-present)*, vol. 26, no. 4, p. 043301, 2014.
- [94] HATTON, R. L., DING, Y., CHOSET, H., and GOLDMAN, D. I., “Geometric visualization of self-propulsion in a complex medium,” *Physical review letters*, vol. 110, no. 7, p. 078101, 2013.
- [95] HEDRICK, T. and DANIEL, T., “Flight control in the hawkmoth *Manduca sexta*: the inverse problem of hovering,” *The journal of experimental Biology*, vol. 209, no. 16, pp. 3114–3130, 2006.

- [96] HENANN, D. L. and KAMRIN, K., “A predictive, size-dependent continuum model for dense granular flows,” *Proceedings of the National Academy of Sciences*, vol. 110, no. 17, pp. 6730–6735, 2013.
- [97] HERRMANN, H. J., HOVI, J.-P., and LUDING, S., *Physics of dry granular media*, vol. 350. Springer Science & Business Media, 2013.
- [98] HILL, G., YEUNG, S., and KOEHLER, S., “Scaling vertical drag forces in granular media,” *EPL (Europhysics Letters)*, vol. 72, no. 1, p. 137, 2005.
- [99] HIROSE, S. and MORI, M., “Biologically inspired snake-like robots,” in *Robotics and Biomimetics, 2004. ROBIO 2004. IEEE International Conference on*, pp. 1–7, IEEE, 2004.
- [100] HOGAN, N., “Impedance control: An approach to manipulation: Part III Implementation,” *Journal of dynamic systems, measurement, and control*, vol. 107, no. 1, pp. 8–16, 1985.
- [101] HOGAN, N., “Stable execution of contact tasks using impedance control,” in *Robotics and Automation. Proceedings. 1987 IEEE International Conference on*, vol. 4, pp. 1047–1054, IEEE, 1987.
- [102] HOLMES, P., FULL, R. J., KODITSCHKEK, D., and GUCKENHEIMER, J., “The dynamics of legged locomotion: Models, analyses, and challenges,” *Siam Review*, vol. 48, no. 2, pp. 207–304, 2006.
- [103] HOOVER, A. M., BURDEN, S., FU, X.-Y., SASTRY, S. S., and FEARING, R. S., “Bio-inspired design and dynamic maneuverability of a minimally actuated six-legged robot,” in *Biomedical Robotics and Biomechanics (BioRob), 2010 3rd IEEE RAS and EMBS International Conference on*, pp. 869–876, IEEE, 2010.
- [104] HU, D. L., NIRODY, J., SCOTT, T., and SHELLY, M. J., “The mechanics of slithering locomotion,” *Proceedings of the National Academy of Sciences*, vol. 106, no. 25, pp. 10081–10085, 2009.
- [105] HUMPHRIES, N. E., QUEIROZ, N., DYER, J. R., PADE, N. G., MUSYL, M. K., SCHAEFER, K. M., FULLER, D. W., BRUNNSCHWEILER, J. M., DOYLE, T. K., HOUGHTON, J. D., and OTHERS, “Environmental context explains Lévy and Brownian movement patterns of marine predators,” *Nature*, vol. 465, no. 7301, pp. 1066–1069, 2010.
- [106] IJSPEERT, A. J., “Central pattern generators for locomotion control in animals and robots: a review,” *Neural Networks*, vol. 21, no. 4, pp. 642–653, 2008.
- [107] ISHIGAMI, G., MIWA, A., NAGATANI, K., and YOSHIDA, K., “Terramechanics-based model for steering maneuver of planetary exploration rovers on loose soil,” *Journal of Field robotics*, vol. 24, no. 3, pp. 233–250, 2007.

- [108] IWASHITA, K. and ODA, M., “Rolling resistance at contacts in simulation of shear band development by DEM,” *Journal of engineering mechanics*, vol. 124, no. 3, pp. 285–292, 1998.
- [109] JAEGER, H. M., NAGEL, S. R., and BEHRINGER, R. P., “Granular solids, liquids, and gases,” *Reviews of modern physics*, vol. 68, no. 4, p. 1259, 1996.
- [110] JANOSI, Z. and HANAMOTO, B., “The analytical determination of drawbar pull as a function of slip for tracked vehicles in deformable soils,” in *Proc. of the First Int. Conf. On Terrain-Vehicle Systems*, Turin, Italy, 1961.
- [111] JAYNE, B. C., “Kinematics of terrestrial snake locomotion,” *Copeia*, pp. 915–927, 1986.
- [112] JAYNE, B. C., “Muscular mechanisms of snake locomotion: an electromyographic study of lateral undulation of the florida banded water snake (*Nerodia fasciata*) and the yellow rat snake (*Elaphe obsoleta*),” *Journal of Morphology*, vol. 197, no. 2, pp. 159–181, 1988.
- [113] JERKINS, M., SCHRÖTER, M., SWINNEY, H. L., SENDEN, T. J., SAADATFAR, M., and ASTE, T., “Onset of mechanical stability in random packings of frictional spheres,” *Physical review letters*, vol. 101, no. 1, p. 018301, 2008.
- [114] JINDRICH, D. L. and FULL, R. J., “Dynamic stabilization of rapid hexapedal locomotion,” *Journal of Experimental Biology*, vol. 205, no. 18, pp. 2803–2823, 2002.
- [115] JOHNSON, A. M., HALE, M. T., HAYNES, G., and KODITSCHKEK, D. E., “Autonomous legged hill and stairwell ascent,” in *Safety, Security, and Rescue Robotics (SSRR), 2011 IEEE International Symposium on*, pp. 134–142, IEEE, 2011.
- [116] JOHNSON, K. L., KENDALL, K., and ROBERTS, A. D., “Surface energy and the contact of elastic solids,” *Proceedings of the Royal Society of London A: Mathematical, Physical and Engineering Sciences*, vol. 324, no. 1558, pp. 301–313, 1971.
- [117] JUAREZ, G., LU, K., SZNITMAN, J., and ARRATIA, P. E., “Motility of small nematodes in wet granular media,” *EPL (Europhysics Letters)*, vol. 92, no. 4, p. 44002, 2010.
- [118] JUNG, S., “*Caenorhabditis elegans* swimming in a saturated particulate system,” *Physics of Fluids (1994-present)*, vol. 22, no. 3, p. 031903, 2010.
- [119] KAMRIN, K. and KOVAL, G., “Nonlocal constitutive relation for steady granular flow,” *Physical Review Letters*, vol. 108, no. 17, p. 178301, 2012.
- [120] KATSURAGI, H. and DURIAN, D. J., “Unified force law for granular impact cratering,” *Nature Physics*, vol. 3, no. 6, pp. 420–423, 2007.

- [121] KAUFMAN, D. M., SUEDA, S., JAMES, D. L., and PAI, D. K., “Staggered projections for frictional contact in multibody systems,” *ACM Trans. Graph.*, vol. 27, pp. 164:1–164:11, Dec. 2008.
- [122] KAVANAU, J. L. and NORRIS, K. S., “Behavior studies by capacitance sensing,” *Science*, vol. 134, no. 3481, pp. 730–732, 1961.
- [123] KERN, M., TIEFENBACHER, F., and MCELWAIN, J., “The rheology of snow in large chute flows,” *Cold Regions Science and Technology*, vol. 39, no. 2, pp. 181–192, 2004.
- [124] KIM, S., CLARK, J. E., and CUTKOSKY, M. R., “iSprawl: Design and tuning for high-speed autonomous open-loop running,” *The International Journal of Robotics Research*, vol. 25, no. 9, pp. 903–912, 2006.
- [125] KLAUBER, L. M., *Studies of reptile life in the arid southwest*. Zoological Society of San Diego, 1939.
- [126] KODITSCHKEK, D. E., “Exact robot navigation by means of potential functions: Some topological considerations,” in *Robotics and Automation. Proceedings. 1987 IEEE International Conference on*, vol. 4, pp. 1–6, IEEE, 1987.
- [127] LANDAU, L. and LIFSHITZ, E., “Classical mechanics,” 1960.
- [128] LAUDER, G. V., ANDERSON, E. J., TANGORRA, J., and MADDEN, P. G., “Fish biorobotics: kinematics and hydrodynamics of self-propulsion,” *Journal of Experimental Biology*, vol. 210, no. 16, pp. 2767–2780, 2007.
- [129] LAUDER, G. V., NAUEN, J. C., and DRUCKER, E. G., “Experimental hydrodynamics and evolution: function of median fins in ray-finned fishes,” *Integrative and Comparative Biology*, vol. 42, no. 5, pp. 1009–1017, 2002.
- [130] LAUGA, E., DILUZIO, W. R., WHITESIDES, G. M., and STONE, H. A., “Swimming in circles: motion of bacteria near solid boundaries,” *Biophysical journal*, vol. 90, no. 2, pp. 400–412, 2006.
- [131] LAUGA, E. and POWERS, T. R., “The hydrodynamics of swimming microorganisms,” *Reports on Progress in Physics*, vol. 72, no. 9, p. 096601, 2009.
- [132] LEHMANN, F.-O. and PICK, S., “The aerodynamic benefit of wing–wing interaction depends on stroke trajectory in flapping insect wings,” *Journal of experimental biology*, vol. 210, no. 8, pp. 1362–1377, 2007.
- [133] LI, C., HOOVER, A. M., BIRKMEYER, P., UMBANHOWAR, P. B., FEARING, R. S., and GOLDMAN, D. I., “Systematic study of the performance of small robots on controlled laboratory substrates,” in *SPIE Defense, Security, and Sensing*, pp. 76790Z–76790Z, International Society for Optics and Photonics, 2010.

- [134] LI, C., HSIEH, S. T., and GOLDMAN, D. I., “Multi-functional foot use during running in the zebra-tailed lizard (*Callisaurus draconoides*),” *Journal of Experimental Biology*, vol. 215, no. 18, pp. 3293–3308, 2012.
- [135] LI, C., UMBANHOWAR, P. B., KOMSUOGLU, H., KODITSCHKEK, D. E., and GOLDMAN, D. I., “Sensitive dependence of the motion of a legged robot on granular media,” *Proceedings of the National Academy of Sciences*, vol. 106, no. 9, pp. 3029–3034, 2009.
- [136] LI, C., ZHANG, T., and GOLDMAN, D. I., “A terradynamics of legged locomotion on granular media,” *Science*, vol. 339, no. 6126, pp. 1408–1412, 2013.
- [137] LIU, B., POWERS, T. R., and BREUER, K. S., “Force-free swimming of a model helical flagellum in viscoelastic fluids,” *Proceedings of the National Academy of Sciences*, vol. 108, no. 49, pp. 19516–19520, 2011.
- [138] LIU, C. and JAIN, S., “A quick tutorial on multibody dynamics,” *Online tutorial*, June, p. 7, 2012.
- [139] LIU, C., LIU, T., LIU, L., and LIU, K., “A new chaotic attractor,” *Chaos, Solitons & Fractals*, vol. 22, no. 5, pp. 1031–1038, 2004.
- [140] LORENTZ, H. A., “The motion of electrons in metallic bodies,” *K. Ned. Akad. van Wet. B*, vol. 7, pp. 438–453, 1905.
- [141] MACHTA, J. and ZWANZIG, R., “Diffusion in a periodic Lorentz gas,” *Phys. Rev. Lett.*, vol. 50, pp. 1959–1962, 1983.
- [142] MALADEN, R. D., DING, Y., LI, C., and GOLDMAN, D. I., “Undulatory swimming in sand: subsurface locomotion of the sandfish lizard,” *science*, vol. 325, no. 5938, pp. 314–318, 2009.
- [143] MALADEN, R. D., DING, Y., UMBANHOWAR, P. B., KAMOR, A., and GOLDMAN, D. I., “Mechanical models of sandfish locomotion reveal principles of high performance subsurface sand-swimming,” *Journal of The Royal Society Interface*, vol. 8, no. 62, pp. 1332–1345, 2011.
- [144] MARVI, H., GONG, C., GRAVISH, N., ASTLEY, H., TRAVERS, M., HATTON, R. L., MENDELSON, J. R., CHOSET, H., HU, D. L., and GOLDMAN, D. I., “Sidewinding with minimal slip: Snake and robot ascent of sandy slopes,” *Science*, vol. 346, no. 6206, pp. 224–229, 2014.
- [145] MATSON, J., “Unfree Spirit: NASA’s Mars rover appears stuck for good,” *Scientific American*, vol. 302, no. 4, pp. 16–16, 2010.
- [146] MAZHAR, H., HEYN, T., PAZOUKI, A., MELANZ, D., SEIDL, A., BARTHOLOMEW, A., TASORA, A., and NEGRUT, D., “Chrono: a parallel multi-physics library for rigid-body, flexible-body, and fluid dynamics,” *Mech. Sci.*, vol. 4, no. 1, pp. 49–64, 2013.

- [147] MAZOUCHOVA, N., GRAVISH, N., SAVU, A., and GOLDMAN, D. I., “Utilization of granular solidification during terrestrial locomotion of hatchling sea turtles,” *Biology letters*, p. rsbl20091041, 2010.
- [148] MAZOUCHOVA, N., UMBANHOWAR, P. B., and GOLDMAN, D. I., “Flipper-driven terrestrial locomotion of a sea turtle-inspired robot,” *Bioinspiration & biomimetics*, vol. 8, no. 2, p. 026007, 2013.
- [149] McMILLEN, T., WILLIAMS, T., and HOLMES, P., “Nonlinear muscles, passive viscoelasticity and body taper conspire to create neuromechanical phase lags in anguilliform swimmers,” *PLoS Comput Biol*, vol. 4, no. 8, p. e1000157, 2008.
- [150] MEIRION-GRIFFITH, G. and SPENKO, M., “An empirical study of the teramechanics of small unmanned ground vehicles,” in *Aerospace Conference, 2010 IEEE*, pp. 1–6, IEEE, 2010.
- [151] MILLER, A. H. and STEBBINS, R. C., *The lives of desert animals in Joshua Tree National Monument*. Univ of California Press, 1964.
- [152] MITARAI, N. and NORI, F., “Wet granular materials,” *Advances in Physics*, vol. 55, no. 1-2, pp. 1–45, 2006.
- [153] MITTAL, R., DONG, H., BOZKURTTAS, M., LAUDER, G., and MADDEN, P., “Locomotion with flexible propulsors: II. Computational modeling of pectoral fin swimming in sunfish,” *Bioinspiration & biomimetics*, vol. 1, no. 4, p. S35, 2006.
- [154] MOON, B. R. and GANS, C., “Kinematics, muscular activity and propulsion in gopher snakes,” *Journal of Experimental Biology*, vol. 201, no. 19, pp. 2669–2684, 1998.
- [155] MORRIS, G. P. and RONDONI, L., “Periodic orbit expansions for the Lorentz gas,” *J. Stat. Phys.*, vol. 75, pp. 553–584, 1994.
- [156] MOSAUER, W., “Adaptive convergence in the sand reptiles of the Sahara and of California: a study in structure and behavior,” *Copeia*, vol. 1932, no. 2, pp. 72–78, 1932.
- [157] MUSCARELLO, V., MASARATI, P., and QUARANTA, G., “Multibody analysis of rotorcraft-pilot coupling,” in *Proceedings of the 2nd Joint International Conference on Multibody System Dynamics*, P. Eberhard and P. Ziegler, eds, 2012.
- [158] NAKAMURA, Y. and SEKIGUCHI, A., “The chaotic mobile robot,” *Robotics and Automation, IEEE Transactions on*, vol. 17, no. 6, pp. 898–904, 2001.
- [159] NAWROTH, J., FEITL, K., COLIN, S., COSTELLO, J. H., and DABIRI, J., “Phenotypic plasticity in juvenile jellyfish medusae facilitates effective animal–fluid interaction,” *Biology letters*, vol. 6, no. 3, pp. 389–393, 2010.

- [160] NEDDERMAN, R., “Statics and kinematics of granular materials,” *Cambridge University Press*, 1992.
- [161] NEWMAN, J. N., *Marine hydrodynamics*. MIT press, 1977.
- [162] NISHIKAWA, K., BIEWENER, A. A., AERTS, P., AHN, A. N., CHIEL, H. J., DALEY, M. A., DANIEL, T. L., FULL, R. J., HALE, M. E., HEDRICK, T. L., and OTHERS, “Neuromechanics: an integrative approach for understanding motor control,” *Integrative and Comparative Biology*, vol. 47, no. 1, pp. 16–54, 2007.
- [163] NOWAK, S., SAMADANI, A., and KUDROLLI, A., “Maximum angle of stability of a wet granular pile,” *Nature Physics*, vol. 1, no. 1, pp. 50–52, 2005.
- [164] ODA, M. and IWASHITA, K., “Study on couple stress and shear band development in granular media based on numerical simulation analyses,” *International journal of engineering science*, vol. 38, no. 15, pp. 1713–1740, 2000.
- [165] PATLA, A. E., “Understanding the roles of vision in the control of human locomotion,” *Gait & Posture*, vol. 5, no. 1, pp. 54–69, 1997.
- [166] PENNYCUICK, C., “Mechanics of flight,” *Avian biology*, vol. 5, pp. 1–75, 1975.
- [167] PETROV, M. P. and OTHERS, *Deserts of the world*. John Wiley and Sons, 1976.
- [168] PFEIFFER, F. and GLOCKER, C., *Multibody dynamics with unilateral contacts*, vol. 9. John Wiley & Sons, 1996.
- [169] PHARR, G., OLIVER, W., and BROTZEN, F., “On the generality of the relationship among contact stiffness, contact area, and elastic modulus during indentation,” *Journal of materials research*, vol. 7, no. 03, pp. 613–617, 1992.
- [170] PLAYTER, R., BUEHLER, M., and RAIBERT, M., “BigDog,” in *Defense and Security Symposium*, pp. 62302O–62302O, International Society for Optics and Photonics, 2006.
- [171] POMEROY, J. and BRUN, E., “Physical properties of snow,” *Snow ecology*, pp. 45–126, 2001.
- [172] PROCTOR, J., KUKILLAYA, R., and HOLMES, P., “A phase-reduced neuro-mechanical model for insect locomotion: feed-forward stability and proprioceptive feedback,” *Philosophical Transactions of the Royal Society of London A: Mathematical, Physical and Engineering Sciences*, vol. 368, no. 1930, pp. 5087–5104, 2010.
- [173] QIAN, F. and GOLDMAN, D., “Anticipatory control using substrate manipulation enables trajectory control of legged locomotion on heterogeneous granular media,” in *SPIE Defense+ Security*, pp. 94671U–94671U, International Society for Optics and Photonics, 2015.

- [174] QIAN, F. and GOLDMAN, D. I., “The dynamics of legged locomotion in heterogeneous terrain: universality in scattering and sensitivity to initial conditions,” in *Proceedings of Robotics: Science and Systems*, RSS, 2015.
- [175] QIAN, F., ZHANG, T., KORFF, W., UMBANHOWAR, P. B., FULL, R. J., and GOLDMAN, D. I., “Principles of appendage design in robots and animals determining terradynamic performance on flowable ground,” *Bioinspiration & biomimetics*, vol. 10, no. 5, p. 056014, 2015.
- [176] QUILLIN, K. J., “Kinematic scaling of locomotion by hydrostatic animals: ontogeny of peristaltic crawling by the earthworm *Lumbricus terrestris*,” *Journal of Experimental Biology*, vol. 202, no. 6, pp. 661–674, 1999.
- [177] RAIBERT, M., BLANKESPOOR, K., NELSON, G., PLAYTER, R., and TEAM, T., “BigDog, the rough-terrain quadruped robot,” in *Proceedings of the 17th World Congress*, vol. 17, pp. 10822–10825, 2008.
- [178] RAIBERT, M. H., *Legged robots that balance*. MIT press, 1986.
- [179] RAYNER, J., “A new approach to animal flight mechanics,” *Journal of Experimental Biology*, vol. 80, no. 1, pp. 17–54, 1979.
- [180] RIMON, E. and KODITSCHKEK, D. E., “Exact robot navigation using artificial potential functions,” *Robotics and Automation, IEEE Transactions on*, vol. 8, no. 5, pp. 501–518, 1992.
- [181] RODENBORN, B., CHEN, C.-H., SWINNEY, H. L., LIU, B., and ZHANG, H., “Propulsion of microorganisms by a helical flagellum,” *Proceedings of the National Academy of Sciences*, vol. 110, no. 5, pp. E338–E347, 2013.
- [182] ROLLINSON, D. and CHOSET, H., “Gait-based compliant control for snake robots,” in *Robotics and Automation (ICRA), 2013 IEEE International Conference on*, pp. 5138–5143, IEEE, 2013.
- [183] RUELLE, D., “A measure associated with Axiom-A attractors,” *Amer. J. Math.*, vol. 98, pp. 619–654, 1976.
- [184] RUELLE, D., “Sensitive dependence on initial condition and turbulent behavior of dynamical systems,” *Annals of the New York Academy of Sciences*, vol. 316, no. 1, pp. 408–416, 1979.
- [185] SANE, S. P., “The aerodynamics of insect flight,” *The journal of experimental Biology*, vol. 206, no. 23, pp. 4191–4208, 2003.
- [186] SANE, S. P., SRYGLEY, R. B., and DUDLEY, R., “Antennal regulation of migratory flight in the neotropical moth *Urania fulgens*,” *Biology letters*, p. rsbl20091073, 2010.

- [187] SARANLI, U., BUEHLER, M., and KODITSCHKEK, D. E., “RHex: A simple and highly mobile hexapod robot,” *The International Journal of Robotics Research*, vol. 20, no. 7, pp. 616–631, 2001.
- [188] SCHMITT, J., GARCIA, M., RAZO, R., HOLMES, P., and FULL, R. J., “Dynamics and stability of legged locomotion in the horizontal plane: a test case using insects,” *Biological cybernetics*, vol. 86, no. 5, pp. 343–353, 2002.
- [189] SCHMITT, J. and HOLMES, P., “Mechanical models for insect locomotion: dynamics and stability in the horizontal plane I. Theory,” *Biological cybernetics*, vol. 83, no. 6, pp. 501–515, 2000.
- [190] SCHRÖTER, M., GOLDMAN, D. I., and SWINNEY, H. L., “Stationary state volume fluctuations in a granular medium,” *Physical Review E*, vol. 71, no. 3, p. 030301, 2005.
- [191] SEGUIN, A., BERTHO, Y., MARTINEZ, F., CRASSOUS, J., and GONDRET, P., “Experimental velocity fields and forces for a cylinder penetrating into a granular medium,” *Physical Review E*, vol. 87, no. 1, p. 012201, 2013.
- [192] SENATORE, C. and IAGNEMMA, K., “Analysis of stress distributions under lightweight wheeled vehicles,” *Journal of Terramechanics*, vol. 51, pp. 1–17, 2014.
- [193] SHARPE, S. S., KOEHLER, S. A., KUCKUK, R. M., SERRANO, M., VELA, P. A., MENDELSON, J., and GOLDMAN, D. I., “Locomotor benefits of being a slender and slick sand swimmer,” *The Journal of experimental biology*, vol. 218, no. 3, pp. 440–450, 2015.
- [194] SHARPE, S. S., KUCKUK, R., and GOLDMAN, D. I., “Controlled preparation of wet granular media reveals limits to lizard burial ability,” *Physical biology*, vol. 12, no. 4, p. 046009, 2015.
- [195] SICILIANO, B. and KHATIB, O., *Springer handbook of robotics*. Springer Science & Business Media, 2008.
- [196] SIMS, D. W., SOUTHALL, E. J., HUMPHRIES, N. E., HAYS, G. C., BRADSHAW, C. J., PITCHFORD, J. W., JAMES, A., AHMED, M. Z., BRIERLEY, A. S., HINDELL, M. A., and OTHERS, “Scaling laws of marine predator search behaviour,” *Nature*, vol. 451, no. 7182, pp. 1098–1102, 2008.
- [197] SINAI, Y. G., “Dynamical systems with elastic reflections: Ergodic properties of dispersing billiards,” *Usp. Mat. Nauk*, vol. 25, pp. 141–192, 1970.
- [198] SINAI, Y. G., “Gibbs measures in ergodic theory,” *Russ. Math. Surv.*, vol. 27, p. 21, 1972.
- [199] SPARROW, C., *The Lorenz equations: bifurcations, chaos, and strange attractors*, vol. 41. Springer Science & Business Media, 2012.

- [200] STEPHENS, G. J., JOHNSON-KERNER, B., BIALEK, W., and RYU, W. S., “Dimensionality and dynamics in the behavior of *C. elegans*,” *PLoS Comput Biol*, vol. 4, no. 4, p. e1000028, 2008.
- [201] STEWART, D. E. and TRINKLE, J. C., “An implicit time-stepping scheme for rigid body dynamics with inelastic collisions and coulomb friction,” *International Journal for Numerical Methods in Engineering*, vol. 39, no. 15, pp. 2673–2691, 1996.
- [202] TAGA, G., “A model of the neuro-musculo-skeletal system for human locomotion,” *Biological cybernetics*, vol. 73, no. 2, pp. 97–111, 1995.
- [203] TAN, J., *Locomotion Synthesis in Complex Physically Simulated Environments*. PhD thesis, Georgia Institute of Technology, 2015.
- [204] TASORA, A., SILVESTRI, M., and RIGHETTINI, P., “Architecture of the Chrono::Engine physics simulation middleware,” in *Proceedings of Multibody Dynamics 2007, ECCOMAS thematic conference*, Citeseer, 2007.
- [205] TERZOPOULOS, D., PLATT, J., BARR, A., and FLEISCHER, K., “Elastically deformable models,” *SIGGRAPH Comput. Graph.*, vol. 21, pp. 205–214, Aug. 1987.
- [206] THEOBALD, J. C., RINGACH, D. L., and FRYE, M. A., “Visual stabilization dynamics are enhanced by standing flight velocity,” *Biology letters*, p. rsbl20090845, 2009.
- [207] THORNTON, C., “Numerical simulations of deviatoric shear deformation of granular media,” *Géotechnique*, vol. 50, no. 1, pp. 43–53, 2000.
- [208] TRANSETH, A. A., LEINE, R. I., GLOCKER, C., PETTERSEN, K. Y., and LILJEBACK, P., “Snake robot obstacle-aided locomotion: Modeling, simulations, and experiments,” *Robotics, IEEE Transactions on*, vol. 24, no. 1, pp. 88–104, 2008.
- [209] TRUEMAN, E., “The dynamics of burrowing in *Ensis* (Bivalvia),” *Proceedings of the Royal Society of London B: Biological Sciences*, vol. 166, no. 1005, pp. 459–476, 1967.
- [210] TRUEMAN, E., “The mechanism of burrowing of the mole crab, *Emerita*,” *J Exp Biol*, vol. 53, pp. 701–710, 1970.
- [211] UGURLU, B., KOTAKA, K., and NARIKIYO, T., “Actively-compliant locomotion control on rough terrain: Cyclic jumping and trotting experiments on a stiff-by-nature quadruped,” in *Robotics and Automation (ICRA), 2013 IEEE International Conference on*, pp. 3313–3320, IEEE, 2013.
- [212] UI, T., HUSSEY, R., and ROGER, R., “Stokes drag on a cylinder in axial motion,” *Physics of Fluids (1958-1988)*, vol. 27, no. 4, pp. 787–795, 1984.

- [213] UMBANHOWAR, P. and GOLDMAN, D. I., “Granular impact and the critical packing state,” *Physical Review E*, vol. 82, no. 1, p. 010301, 2010.
- [214] VANCE, W. N., “Unstable periodic-orbits and transport-properties of nonequilibrium steady-states,” *Phys. Rev. Lett.*, vol. 69, pp. 1356–1359, 1992.
- [215] VIDELER, J., MULLER, U., and STAMHUIS, E., “Aquatic vertebrate locomotion: wakes from body waves,” *Journal of Experimental Biology*, vol. 202, no. 23, pp. 3423–3430, 1999.
- [216] VISWANATHAN, G. M., DA LUZ, M. G., RAPOSO, E. P., and STANLEY, H. E., *The physics of foraging: an introduction to random searches and biological encounters*. Cambridge University Press, 2011.
- [217] VISWANATHAN, G., RAPOSO, E., and DA LUZ, M., “Lévy flights and superdiffusion in the context of biological encounters and random searches,” *Physics of Life Reviews*, vol. 5, no. 3, pp. 133–150, 2008.
- [218] VITT, L. J., SARTORIUS, S. S., AVILA-PIRES, T. C. S., ESPÓSITO, M. C., and MONTGOMERY, W., “Life on the leaf litter: the ecology of *Anolis nitens tandai* in the Brazilian Amazon,” *Copeia*, vol. 2001, no. 2, pp. 401–412, 2001.
- [219] VOGEL, S., *Life in moving fluids: the physical biology of flow*. Princeton University Press, 1994.
- [220] VOLOS, C. K., KYPRIANIDIS, I. M., and STOUBOULOS, I. N., “A chaotic path planning generator for autonomous mobile robots,” *Robotics and Autonomous Systems*, vol. 60, no. 4, pp. 651–656, 2012.
- [221] WALSH, A. M., HOLLOWAY, K. E., HABDAS, P., and DE BRUYN, J. R., “Morphology and scaling of impact craters in granular media,” *Physical review letters*, vol. 91, no. 10, p. 104301, 2003.
- [222] WANG, Z. J., “Dissecting insect flight,” *Annu. Rev. Fluid Mech.*, vol. 37, pp. 183–210, 2005.
- [223] WARREN JR, W. H., YOUNG, D. S., and LEE, D. N., “Visual control of step length during running over irregular terrain,” *Journal of Experimental Psychology: Human Perception and Performance*, vol. 12, no. 3, p. 259, 1986.
- [224] WINTER, A., DEITS, R., DORSCH, D., SLOCUM, A., HOSOI, A., and OTHERS, “Razor clam to RoboClam: burrowing drag reduction mechanisms and their robotic adaptation,” *Bioinspiration & biomimetics*, vol. 9, no. 3, p. 036009, 2014.
- [225] WINTERS, J. M. and CRAGO, P. E., *Biomechanics and neural control of posture and movement*. Springer Science & Business Media, 2012.
- [226] WONG, J. Y., *Theory of ground vehicles*. John Wiley & Sons, 2001.

- [227] WONG, J.-Y. and REECE, A., “Prediction of rigid wheel performance based on the analysis of soil-wheel stresses part I. Performance of driven rigid wheels,” *Journal of Terramechanics*, vol. 4, no. 1, pp. 81–98, 1967.
- [228] WOOD, R., AVADHANULA, S., SAHAI, R., STELTZ, E., and FEARING, R., “Microrobot design using fiber reinforced composites,” *Journal of Mechanical Design*, vol. 130, no. 5, p. 052304, 2008.
- [229] YAN, J., AVADHANULA, S., BIRCH, J., DICKINSON, M., SITTI, M., SU, T., and FEARING, R., “Wing transmission for a micromechanical flying insect,” *Journal of Micromechatronics*, vol. 1, no. 3, pp. 221–237, 2001.
- [230] ZHANG, T. and GOLDMAN, D. I., “The effectiveness of resistive force theory in granular locomotiona),” *Physics of Fluids (1994-present)*, vol. 26, no. 10, p. 101308, 2014.
- [231] ZHANG, T., QIAN, F., LI, C., MASARATI, P., HOOVER, A. M., BIRKMEYER, P., PULLIN, A., FEARING, R. S., and GOLDMAN, D. I., “Ground fluidization promotes rapid running of a lightweight robot,” *The International Journal of Robotics Research*, vol. 32, no. 7, pp. 859–869, 2013.